Diploma thesis

Manufacturing and characterization of Al-Cu and Al-Cu-Mg alloys and analysis of the precipitation kinetics with DSC measurements

Executed with the purpose of attaining the academical degree of a graduate engineer under the direction of
Univ.Prof. Dipl.-Ing. Dr.techn. Ernst Kozeschnik

at the
Institute for Materials Science and Material Technology

Submitted to the Technical University Vienna
Department for Mechanical Engineering and Science of Management

by
Lorant Pinter

Vienna, February 2010

Acknowledgement

Univ.Prof. Dipl.-Ing. Dr.techn. Ernst Kozeschnik I want to thank for the motivating and excellent supply during my diploma thesis.

For the competent and very extensive supervision I want to thank Univ.Ass. Dipl.-Ing. Dr.techn. Ahmad Falahati.

The laboratory team enabled with the excellent support the implementation of my diploma thesis. Sincere thanks for the explanation of devices and help in the microstructural characterization methods to Heidemarie Knoblich and Christian Zaruba. For the sustained encouragement special thanks at Heinz Kaminski.

For enabling extrusion I want to cordially thank Ass.Prof. Dipl.-Ing. Dr.techn. Christian Edtmaier.

Abstract

These days, the number of existing casting methods for aluminum alloys is high and investigating new technologies is a daily occurrence. Beside the investigation of casting methods, the development of new aluminum alloys is trend-setting. Before the mass-production of a new alloy gets started, many laboratory tests have to be done to ensure, that the material has a chance of survival on the market. The electromagnetic casting (EMC) process has a distinct advantage due to the presence of stirring motions in the melt. Therefore it is a forward-looking method. These stirring motions improve the homogeneity of the alloying elements in the aluminum matrix.

In laboratories, only little amounts of alloys are produced because for microstructural characterization methods like microscopic analyses, DSC, hardness measurements, etc. small specimens are needed. More often than not, the material is molten in crucibles. In this diploma thesis, experiments with three different crucibles were conducted in order to investigate the effect on the alloy´s microstructure.

An induction furnace was used to manufacture Al-Cu and Al-Cu-Mg alloys. The power consumption of the induction coil could be pilot-controlled, if the temperature of the melt was measured with a thermocouple. To keep in mind, temperature measurement with a thermocouple is not practicable for every crucible used in induction furnace. Therefore, different manufacturing possibilities with different crucibles are illustrated.

Furnace atmosphere is very important for the manufacturing procedure. Gas entrapment within the aluminum melt would lead to inclusion of porosities in the alloy. To decrease the number of pores, the material is heated in vacuum for the reason that vacuum has a reduction effect on cavities in the melt. In the experiment, alloys are heated in vacuum and argon to investigate their influence on the microstructure.

The manufactured Al-Cu and Al-Cu-Mg alloys are investigated with light and electron microscopy and the results are illustrated and compared with each other. After homogenization and extrusion, produced alloys are solution heat treated and quenched to room temperature. Moreover, hardness values and DSC curves of these heat treated and quenched alloys are compared with results from literature. With these methods the produced alloys are characterized and compared with each other and given values in literature. The structure of an industrial 2024 aluminum alloy, which is widely applied in aircraft lattices, is also characterized with light and electron microscopy. Aging behavior at room temperature is investigated with hardness measurement. Furthermore, precipitation kinetics of a 2024 alloy is compared with the lab-produced Al-Cu-Mg alloy with the same amount of major alloying elements.

Zusammenfassung

Die Anzahl existierender Gießverfahren für Aluminium ist groß und die Erforschung neuer Methoden ist eine tägliche Herausforderung. Nicht nur die Entwicklung neuer Gießverfahren, sondern auch die Erforschung neuer Aluminiumlegierungen ist zukunftsweisend. Bevor die Massenproduktion einer neuen Legierung gestartet wird, müssen viele Laborversuche durchgeführt werden um das Überleben des neuen Materials am Markt zu gewährleisten. Das elektromagnetische Gießverfahren hat ausgeprägte Vorteile aufgrund des Rühreffektes auf die Schmelze und ist ein zukunftsweisendes Verfahren. Die Rühreffekte verbessern die Homogenität der Legierungselemente im Grundmaterial.

In Labors werden nur geringe Mengen einer Legierung hergestellt weil für die analytischen Methoden wie Mikroskopie, DSC, Härtemessung, usw. nur sehr kleine Proben notwendig sind. In den meisten Fällen werden die Materialien in Tiegeln geschmolzen. Um die Auswirkung auf die Mikrostruktur einer Legierung zu untersuchen, wurden in dieser Diplomarbeit Experimente mit drei verschiedenen Tiegelmaterialien durchgeführt.

Mit einem Induktionsofen wurden Al-Cu und Al-Cu-Mg Legierungen hergestellt. Die Leistung der Induktionsspule konnte durch eine Temperaturmessung mit einem Thermoelement im Tiegel geregelt werden. Jedoch ist die Temperaturmessung nicht für alle Tiegelmaterialien ausführbar. Aus dem Grund wurden verschiedene Herstellungsmöglichkeiten durchgeführt.

Für den Herstellungsprozess ist die Umgebungsatmosphäre der Schmelze von großer Bedeutung. Die Reaktion zwischen Luft und der Aluminiumschmelze kann zu einem Einschluss von Poren führen. Um die Anzahl von Poren zu reduzieren, wird das Material unter Vakuum erhitzt. Im Experiment wurden Aluminiumlegierungen unter Vakuum und Argon hergestellt um deren Einfluss auf die Mikrostruktur zu untersuchen.

Die hergestellten Al-Cu und Al-Cu-Mg Legierungen wurden mit Licht- und Elektronenmikroskopie untersucht und miteinander verglichen. Nach Homogenisieren und Strangpressen wurden die hergestellten Proben lösungsgeglüht und auf Raumtemperatur abgeschreckt. Die Ergebnisse der Härtemessung und DSC wurden mit Werten aus der Literatur verglichen. Durch diese Methoden wurden die Legierungen charakterisiert und sowohl miteinander, als auch mit Ergebnissen aus der Literatur verglichen. Das Gefüge einer industriellen 2024 Aluminiumlegierung, die weit verbreitet für Tragwerke von Flugzeugen eingesetzt wird, wurde ebenfalls mit Licht- und Elektronenmikroskopie untersucht. Der Alterungsprozess während Kaltauslagerung wurde mit Härtemessungen untersucht. Die Ausscheidungskinetik der 2024 Aluminiumlegierung wurde mit den Ergebnissen der im Labor hergestellten Al-Cu-Mg Legierung, die dieselbe Menge an Hauptlegierungselementen aufweist, verglichen.

Table of contents

1 Introduction 8

2 Objectives 9

3 State of the art 10

3.1 Background 10

3.1.1 Classification 10

3.1.2 Phase diagrams 11

3.1.2.1 Al-Cu, Al-Mg and Al-Mn binary phase diagrams 11

3.1.2.2 Al-Cu-Mg ternary phase diagram 13

3.1.3 Alloying elements and heat treatment 14

3.2 Properties of Al-Cu alloys 16

3.2.1 Precipitation sequence 16

3.2.2 Study of DSC curves and hardness 18

3.3 Properties of Al-Cu-Mg alloys 20

3.3.1 Precipitation sequence 20

3.3.2 Study of DSC curves and hardness 22

3.3.3 Properties of 2024 and 2324 aluminum alloys 23

3.4 Direct chill and electromagnetic casting 27

3.5 Homogenization 29

4 Experimental 31

4.1 Materials 31

4.2 Equipment and general test conditions 31

4.2.1 Induction furnace 31

4.2.2 Crucibles 32

4.2.3 Extruder 33

4.2.4 Light microscopy 33

4.2.5 Scanning electron microscopy 33

4.2.6 Hardness measurement 35

4.2.7 Differential Scanning calorimetry 35

4.3 Manufacturing procedure 37

4.3.1 Manufacturing of Al-Cu alloys 37

4.3.1.1 Al-3,85Cu manufactured in a silicon oxide crucible under vacuum 37

4.3.1.2 Al-3,85Cu manufactured in a graphite crucible under vacuum 38

4.3.1.3 Al-4,3Cu manufactured in a graphite crucible under argon 39

4.3.1.4 Al-4,3Cu manufactured in a graphite crucible under vacuum 39

4.3.1.5 Al-4,3Cu manufactured in a boron nitride crucible under vacuum 40

4.3.2 Manufacturing of Al-Cu-Mg alloys 41

4.3.2.1 Al-4,3Cu-1,49Mg manufactured in a graphite crucible under vacuum 41

4.3.2.2 Al-4,3Cu-1,49Mg manufactured in a boron nitride crucible under argon 41

4.4 Homogenization and extrusion of the manufactured Al-Cu and Al-Cu-Mg alloys 42
  4.4.1 Homogenization 42
  4.4.2 Extrusion 42
4.5 Material characterization 43
  4.5.1 Analysis method of the manufactured alloys in the as-cast condition 43
  4.5.2 Analysis method of the manufactured alloys after homogenization and extrusion 43
  4.5.3 Analysis method of an industrial 2024 aluminum alloy 44

5 Results 46
5.1 Characteristics of Al-Cu alloys in the as-cast condition 46
  5.1.1 Al-3,85Cu manufactured in a silicon oxide crucible under vacuum 46
    5.1.1.1 Light microscope analysis 46
  5.1.2 Al-3,85Cu manufactured in a graphite crucible under vacuum 46
    5.1.2.1 Light microscope analysis 47
    5.1.2.2 Scanning electron microscope analysis 50
  5.1.3 Al-4,3Cu manufactured in a graphite crucible under argon 53
    5.1.3.1 Light microscope analysis 53
    5.1.3.2 Scanning electron microscope analysis 54
  5.1.4 Al-4,3Cu manufactured in a graphite crucible under vacuum 54
    5.1.4.1 Light microscope analysis 55
    5.1.4.2 Scanning electron microscope analysis 56
  5.1.5 Al-4,3Cu manufactured in a boron nitride crucible under vacuum 58
    5.1.5.1 Light microscope analysis 58
    5.1.5.2 Scanning electron microscope analysis 59
  5.1.6 Hardness measurement 59
5.2 Characteristics of Al-Cu alloys after homogenization and extrusion 60
  5.2.1 Light microscope analysis 60
  5.2.2 Scanning electron microscope analysis 61
  5.2.3 Hardness measurement 63
  5.2.4 Differential Scanning Calorimetry 63
5.3 Characteristics of Al-Cu-Mg alloys in the as-cast condition 66
  5.3.1 Al-4,3Cu-1,49Mg manufactured in a graphite crucible under vacuum 66
    5.3.1.1 Scanning electron microscope analysis 66
  5.3.2 Al-4,3Cu-1,49Mg manufactured in a boron nitride crucible under argon 67
    5.3.2.1 Light microscope analysis 67
    5.3.2.2 Scanning electron microscope analysis 68
5.4 Characteristics of Al-Cu-Mg alloys after homogenization and extrusion 69
  5.4.1 Light microscope analysis 69
  5.4.2 Scanning electron microscope analysis 70
  5.4.3 Hardness measurement 72
  5.4.4 Differential Scanning Calorimetry 73
5.5 Characteristics of an industrial 2024 aluminum alloy 74
  5.5.1 Light microscope analysis 74

5.5.2 Scanning electron microscope analysis ... 75
5.5.3 Hardness measurement ... 78
5.5.4 Differential Scanning Calorimetry ... 78
6 Discussion ... 83
6.1 Al-Cu alloys ... 83
6.1.1 General manufacturing characteristics ... 83
6.1.2 Characteristics in the as-cast condition ... 84
6.1.3 Characteristics in the homogenized and extruded condition ... 84
6.2 Al-Cu-Mg alloys ... 85
6.2.1 General manufacturing characteristics ... 85
6.2.2 Characteristics in the as-cast condition ... 85
6.2.3 Characteristics in the homogenized and extruded condition ... 85
6.2.4 Comparison of the industrial 2024 alloy and the manufactured Al-Cu-Mg alloy ... 86
7 Summary and conclusions ... 89
8 References ... 90
9 Appendix ... 91
9.1 Hardness measurement ... 91
9.1.1 Results of the Al-4,3Cu alloys in the as-cast condition ... 91
9.1.2 Results of the Al-4,3Cu alloys after homogenization and extrusion ... 91
9.1.3 Results of the Al-4,3Cu-1,49Mg alloy after homogenization and extrusion ... 92
9.1.4 Results for the industrial 2024 aluminum alloy ... 92

1 Introduction

For the last 100 years, lightweight design has become a very important role. Further aluminum alloys are indispensable for these engineering applications. Aluminum alloys are used for aircraft, cars, motorbikes, sports goods, food industry, etc. As a consequence, the demand for these alloys is very high and it is increasing from year to year. Lightweight design means high strength and at the same time low weight of load-bearing materials. Furthermore, these materials should have a high fatigue resistance and high fracture toughness.

How can a material fulfill these requirements? The properties of aluminum are improved by addition of alloying elements and a higher strength to weight ratio is achieved by heat treatment. The multiplicity of possible alloying elements and the appropriate commitment in aluminum is an own science. Solid solution hardening, precipitation hardening, grain refinement and strain hardening are the four strengthening mechanisms. Not all of these strengthening mechanisms are possible for each aluminum alloy and often combinations of different methods are applied. To keep in mind, also the manufacturing process has an influence on the material´s properties.

Many investigations have been made to achieve improvements of aluminum alloys. The question is if further improvements might be achieved. The investigation of different alloying elements plays one of the most significant roles to improve the material´s properties. Further improvements can be obtained with the manufacturing process (e.g. electromagnetic casting). Equipments for producing aluminum alloys are expensive. Before starting the mass-production of a new material, many analyses have to be made in laboratories.

In a nutshell, the production of new aluminum alloys with a state of the technology induction furnace and the analysis of the produced material play a significant role. To gain knowledge about the manufacturing process, some tests must be done with already available materials previous using such a furnace. As an advantage, the manufactured materials can be compared with literature.

In this work, the effects of different furnace atmospheres on the material properties during melting are analyzed. This should give an answer to the question if material properties can be improved by changing the surrounding area. Moreover, producing an alloy with the induction furnace should lead to a homogeneous distribution of the alloying elements. If the stirring motions of the induction coil are given, it is also inspected with microscope inspection. In order to see if the manufacturing process has been successful the hardness values and differential scanning calorimetry (DSC) curves of the manufactured alloys are compared with results from literature. Additionally, microstructural characterization methods are applied on a defined aluminum alloy in order to obtain the necessary know-how for further research of the manufactured alloys.

2 Objectives

The properties of aluminium alloys depend on complex interaction of containing chemical elements, microstructural features developed during solidification, thermal treatments, and for wrought products on deformation process. During this investigation pure Al-Cu and pure Al-Cu-Mg alloys are produced in lab scale and by using induction furnace. After casting the material will be homogenized and extruded. The main objective is to investigate different controlling parameters in the production route and to characterize the materials at each process step.

- Investigation of the manufacturing process of Al-Cu and Al-Cu-Mg alloys and gathering the necessary know-how to use correctly the induction furnace.
- Experimentation with different crucibles and melting in different environment (vacuum, argon, air) to gain knowledge about the influence on the alloy´s properties.
- Characterize the microstructure in the as-cast, homogenized and extruded condition with light and scanning electron microscope to identify porosities and homogeneous/ inhomogeneous alloying element distribution.
- Using differential scanning calorimetry analysis and hardness measurements for the homogenized and extruded alloys to characterize the precipitation kinetics of the manufactured materials.

To have a comparison between industrial alloys (which include trace elements) and our lab production alloys (with pure elements), microstructure and precipitation kinetics of an industrial alloy type 2024 is compared with the Al-Cu-Mg alloy with the same amount of major alloying elements.

3 State of the art

3.1 Background

In this chapter, some basics were summarized to relieve the understanding of the following literature. These basics are classification, binary and ternary phase diagrams (Al-Cu, Al-Mg, Al-Mn and Al-Cu-Mg) and a chapter about the influence of alloying elements and heat treatment.

3.1.1 Classification

Primarily, aluminum alloys are classified as wrought or cast alloys on the basis of the processing techniques. Wrought aluminum alloys are produced by hot or cold plastic deformation of cast ingots into semi-finished forms (such as extrusions, sheets, rods, bars, tubes, wires and forgings etc.). The composition-based classification of wrought aluminum alloys by international alloy designation system (IADS) is shown in Table 3.1.1a. [1]

Table 3.1.1a: Classification of the wrought aluminum alloys by IADS [1]

Series	Main alloying elements
1xxx	Unalloyed (>99% Al)
2xxx	Copper (Cu)
3xxx	Manganese (Mn)
4xxx	Silicon (Si)
5xxx	Magnesium (Mg)
6xxx	Magnesium (Mg) and Silicon (Si)
7xxx	Zinc (Zn)
8xxx	Miscellaneous alloys

Aluminum alloys are further classified into heat treatable and non-heat treatable alloys. Heat treatable aluminum alloys (2xxx, 6xxx, and 7xxx series) are significantly strengthened by precipitation hardening resulting from heat treatments incorporating solution treatment, quenching and aging processes. Non-heat treatable alloys (1xxx, 3xxx and 5xxx series) do not respond to aging heat treatments and are strengthened mainly by cold working and solution strengthening. The temper designation for wrought aluminum alloys are presented in Table 3.1.1b. [1]

Table 3.1.1b: Temper designation system for wrought aluminum alloys [1]

Suffix letter	Description
F	As fabricated
O	Annealed (wrought products only)
H	Cold worked / strain hardened
W	Solution heat treated
T	Heat treated (stable)

In casting alloys, castability is improved through the addition of silicon up to 13%. Dimensional stability upon heating (pistons) is assured by silicon contents up to 25%. [2]

3.1.2 Phase diagrams

3.1.2.1 Al-Cu, Al-Mg and Al-Mn binary phase diagrams

Fig. 3.1.2.1a shows the Al-Cu binary phase diagram. Aluminum forms an eutectic with the constituent designated θ ($CuAl_2$), the eutectic point lying at 33% Cu and 548°C. There is an appreciable solid solubility at the aluminum end, the solid solution containing 5,7% Cu at the eutectic temperature, falling to 0,045% at 300°C. The constituent θ has a body-centered-tetragonal lattice and the unit cell contains 4 copper and 8 aluminum atoms. It is thus based on the composition $CuAl_2$, although alloys having this exact composition lie outside the homogeneity range of the constituent. [3]

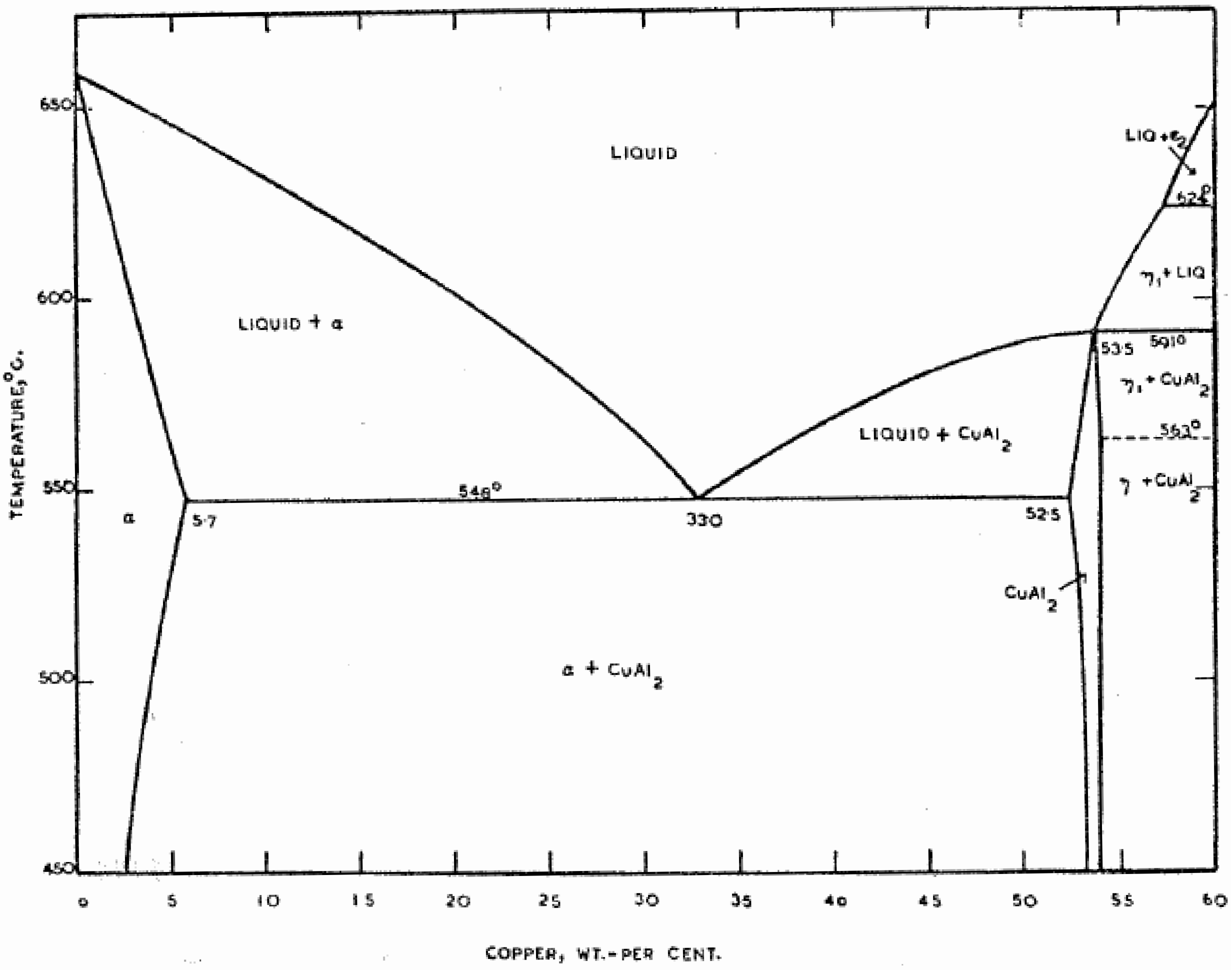

Fig. 3.1.2.1a: Binary phase diagram of Al-Cu [3]

Fig. 3.1.2.1b shows the Al-Mg binary phase diagram. The aluminum-rich alloys exhibit an appreciable solid solubility at the aluminum end, the eutectic, of which the second constituent is that designated β or Mg_2Al_3, lying at 35% Mg and 450°C. The constituent β has a homogeneity range extending from 35 to 37% Mg at it´s temperature of solidification. For convenience, however, the latter designation is often used. It has a hexagonal lattice and the aluminum-rich solid solution contains 15,35% Mg at the eutectic temperature. [3]

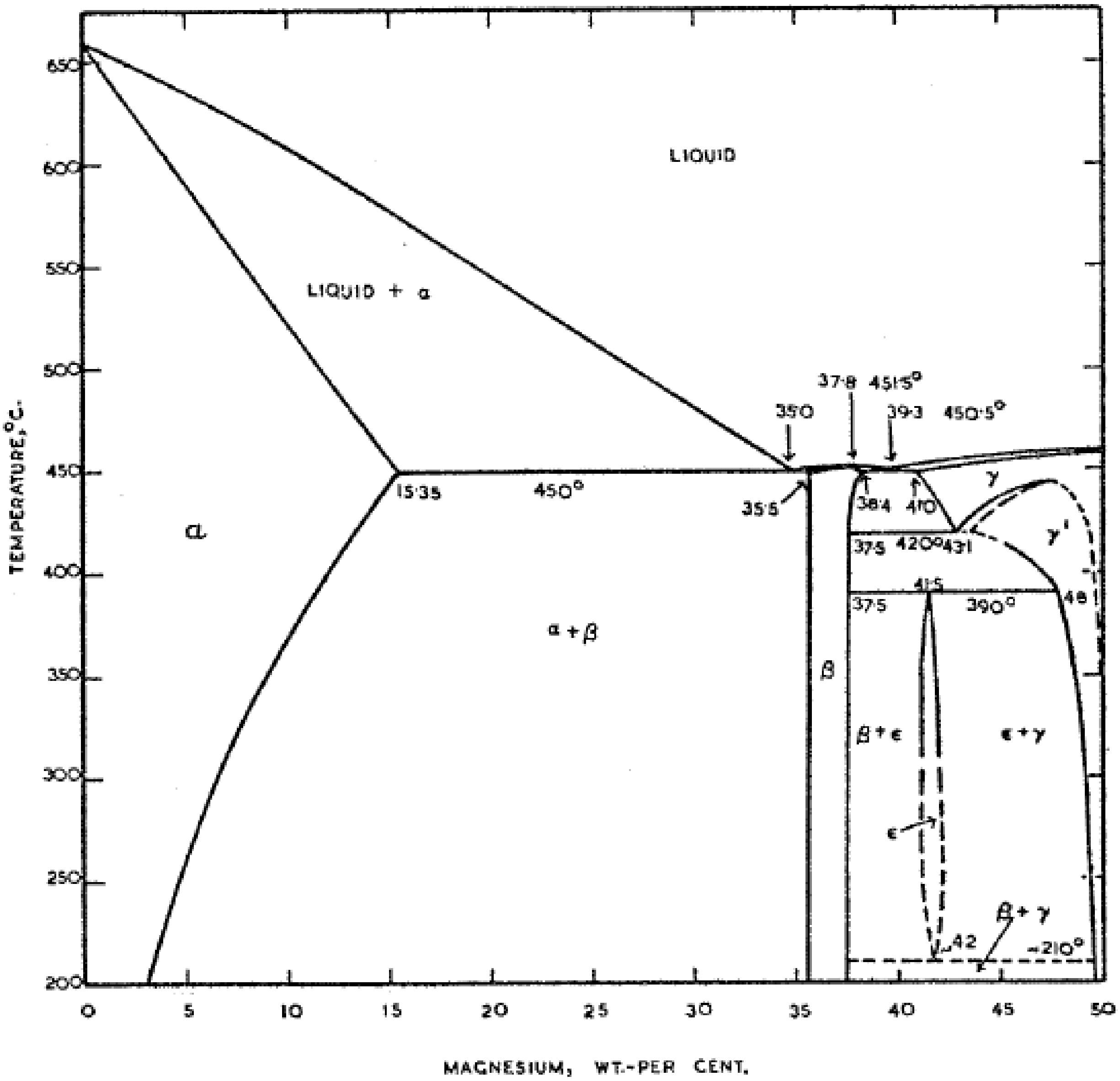

Fig. 3.1.2.1b: Binary phase diagram of Al-Mg [3]

Fig. 3.1.2.1c shows the Al-Mn binary phase diagram. The eutectic, between $MnAl_6$ and the aluminum-rich solid solution, lies at 2% Mn and 658,5°C, the solid solution containing 1,82% Mn. On the manganese side of the eutectic point, the liquidus rises steeply, the primary constituent remaining $MnAl_6$ until a composition of 4,1% Mn and a temperature of 710°C is reached, at which a peritectic reaction occurs between $MnAl_4$ and liquid to form $MnAl_6$. $MnAl_4$ remains the primary constituent as far as 13% Mn and 822°C. The former of $MnAl_4$ and $MnAl_6$ is hexagonal. [3]

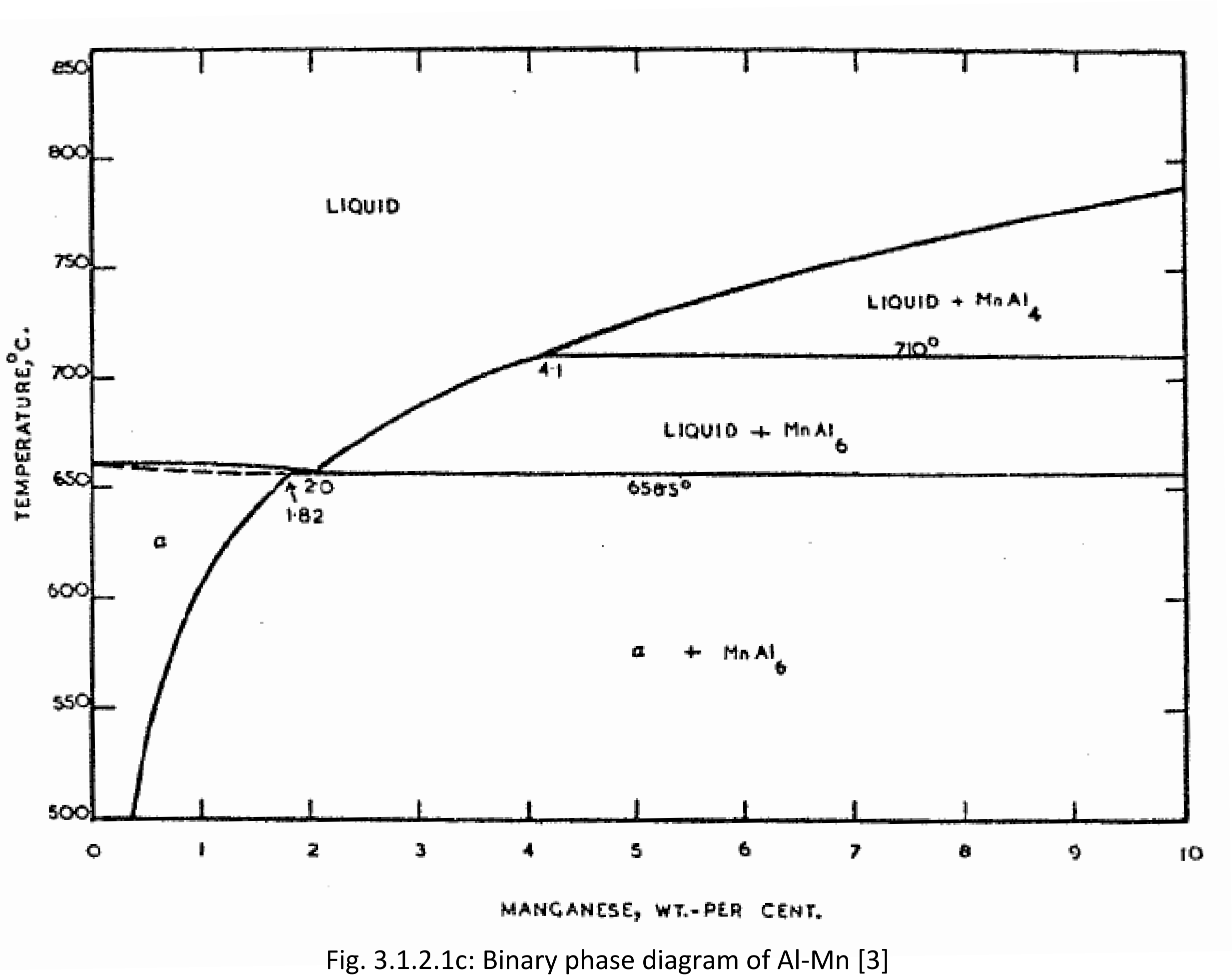

Fig. 3.1.2.1c: Binary phase diagram of Al-Mn [3]

3.1.2.2 Al-Cu-Mg ternary phase diagram

The diagram plotted in Fig. 3.1.2.2 covers the entire ternary system. Along the Al-Mg side of the triangle, the only constituent that is of interest in connection with aluminum-rich alloys is Mg_2Al_3, or β, as it is frequently designated. It forms an eutectic with aluminum containing 35% Mg and freezing at 450°C, the aluminum-rich phase containing 15,35% Mg in solid solution. Along the Al-Cu axis there are again a number of phases, but the only one of interest is that designated $CuAl_2$ or θ, which forms an eutectic with aluminum containing 33% Cu and freezing at 548°C. The aluminum contains 5,7% Cu in solid solution. In the Cu-Mg system, there are two intermetallic phases, Mg_2Cu and $MgCu_2$, both melting without decompositions and both forming eutectics with the adjacent phases. $MgCu_2$ melts at 820°C and has a face-centred cubic lattice. Over the greater part of the ternary system the primary constituent is U. It´s liquidus rises to a maximum at 950°C, at the ringed point, from which a ridge runs down continuously to the $MgCu_2$ maximum in the binary system. U, however, is said to have a body-centred cubic lattice. It has an extended homogeneity range at temperatures below the solidus. U reacts peritectically to form S, Q and V. The boundary between the U and S fields rises to a flat maximum at 550°C, and as the line joining U and S is not continuous with that joining aluminum and S, it is not correct to say that the Al-S system is quasy-binary, thought the statement is correct once the U-S peritectic reaction has been completed. S has a small homogeneity range and is based on the formula $CuMgAl_2$. The constituent Q has a very limited homogeneity range and itself reacts peritectically to form T. V, which is formed peritectically from U, has also a very limited range of homogeneity. The constituent V and U both have primary fields crossing the line joining S and $CuAl_2$. It is therefore clear that the latter section cannot, as formerly suggested, be quasi-binary.

The only constituents that can exist in equilibrium with aluminum at temperatures at and below the solidus are $CuAl_2$, S ($CuMgAl_2$), T and Mg_2Al_3, but because of incomplete peritectic reactions, others, such as U, V and Q may occur in cast alloys. [3]

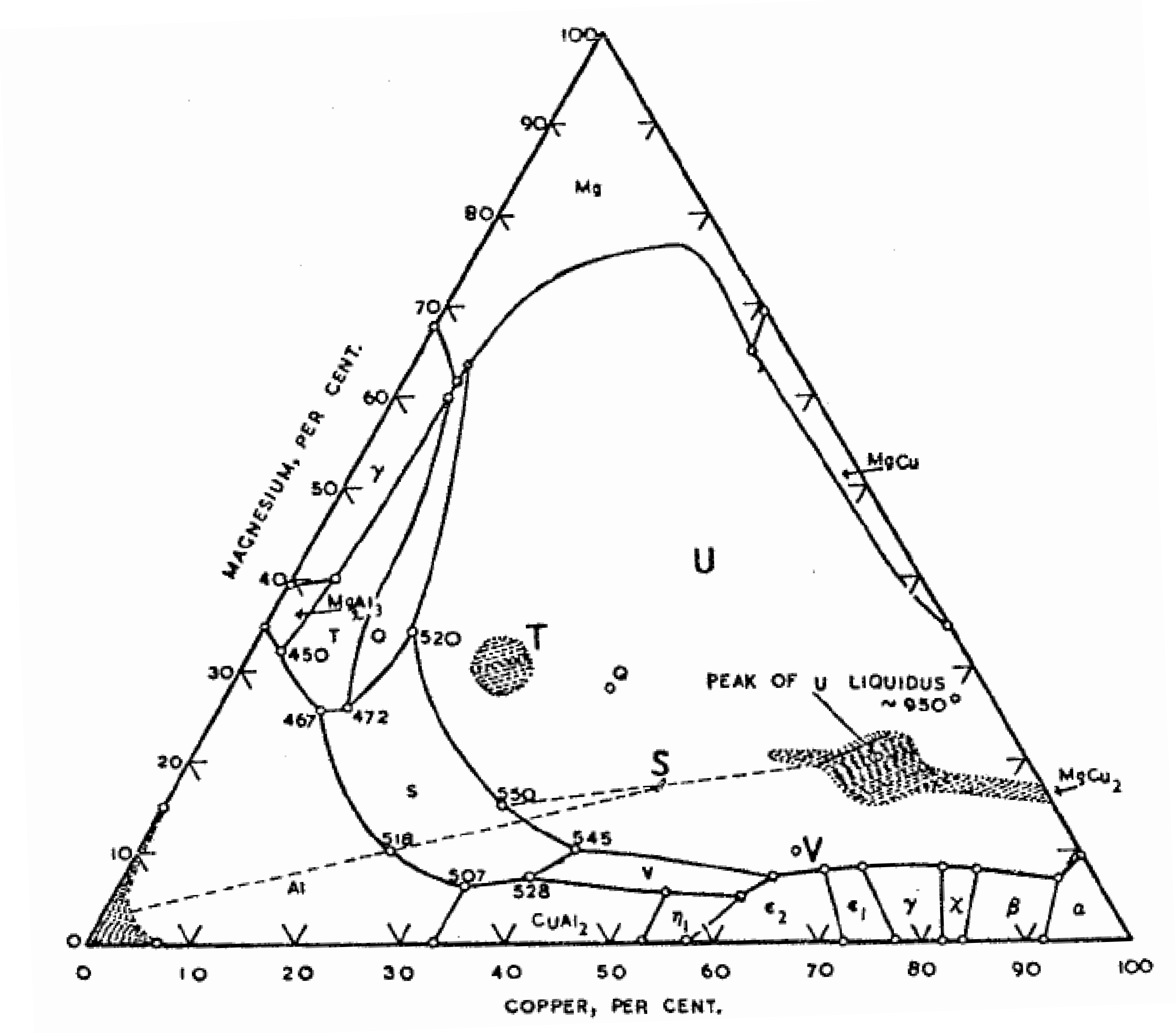

Fig. 3.1.2.2: Ternary phase diagram of Al-Cu-Mg alloys [3]

3.1.3 Alloying elements and heat treatment

The alloying is mainly done to improve the strength and mechanical properties but it also affects the physical properties (such as density, melting temperature, coefficient of the thermal expansion, thermal and electrical properties) and the corrosion resistance of aluminum. The main alloying elements such as copper (Cu), zinc (Zn), magnesium (Mg), silicon (Si), manganese (Mn) and lithium (Li) improve the strengthening of aluminum. While small additions of boron (B), bismuth (Bi), cerium (Ce), chromium (Cr), nickel (Ni), lead (Pb), tin (Sn), titanium (Ti), vanadium (V) and zirconium (Zr) in aluminum affect the machinability, fluidity, electrical resistivity, corrosion-resistance, strength, ductility, etc. Iron (Fe) is the main impurity which is always present in all commercial aluminum alloys in small amounts ranging typically between 0.05 – 0.4 wt%. [1]

In Table 3.1.3a, for aluminum, copper, magnesium and manganese, the melting and boiling points are listed.

Table 3.1.3a: Melting and boiling point of selected elements [4]

Element	Melting point [°C]	Boiling point [°C]
Aluminum	660,32	2467
Copper	1084,4	2567
Magnesium	650	1090
Manganese	1246	2061

Especially, the boiling point of magnesium under vacuum has to be considered because it decreases fast below 200 mbar with decreasing pressure, see Fig. 3.1.3b. The boiling point decreases up to 700°C under a pressure of about 1Pa (= 1x10^{-2} mbar). [5, 6]

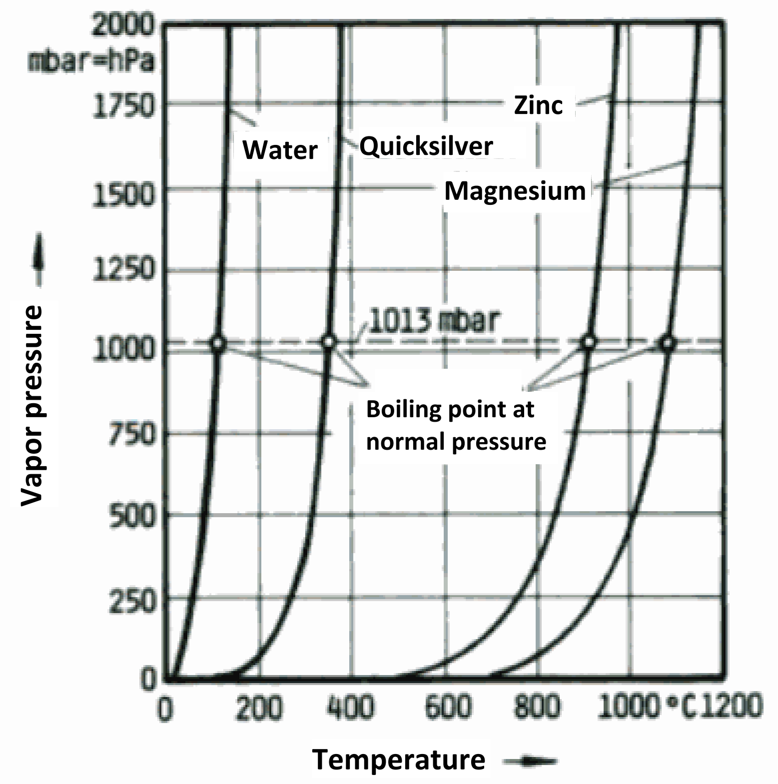

Fig. 3.1.3b: Vapor curve of water, quicksilver, zinc and magnesium [6]

The denotation of abbreviated temper designation is explained in Table 3.1.3b.

Table 3.1.3b: Overview of temper designations [7]

Temper designation	Explanation
T1	Quenched from the hot-working temperature and natural aged
T2	Quenched from the hot-working temperature, cold worked, natural aged
T3	Solution heat treated, cold worked and natural aged
T4	Solution heat treated, quenched and natural aged
T5	Quenched from the hot-working temperature and artificial aged
T6	Solution heat treated, quenched and artificial aged
T7	Solution heat treated, quenched, artificial aged and overcured
T8	Solution heat treated, cold worked and artificial aged
T9	Solution heat treated, artificial aged and cold worked

Hot working, cold working and stretching enhance the number of dislocations. Solid solution heat treatment and quenching generates vacancies. The strength of heat treatable aluminum alloys is significantly improved by precipitation strengthening caused by the resistance to dislocation motion by precipitates formed from the supersaturated solid solution during aging. The fatigue resistance and fracture toughness of aluminum alloys may be improved by lowering the iron and silicon contents. Table 3.1.3c gives an overview of the solid solubilities of selected alloying elements. [1]

Table 3.1.3c: Solid solubilities of selected alloying elements in aluminum [1]

Element	**Temperature [°C]**	**Solid Solubility**	
		wt %	**at %**
Cu	548	5.67	2.48
Fe	655	0.052	0.025
Mg	450	14.9	16.25
Mn	659	1.82	0.90
Si	580	1.65	1.59
Zn	380	82.8	66.4

3.2 Properties of Al-Cu alloys

3.2.1 Precipitation sequence

Many investigations have been devoted to examining the details of the precipitation sequence in this alloy system using both theoretical models and several newly developed techniques.

The copper solubility decreases with decreasing temperature, and it is lower than 0.1 at% copper for temperatures below 200°C. When an alloy with a composition Al - (0.5-2.48) at% Cu is solution heat treated at about 540°C and subsequently quenched to a lower temperature, the copper is retained in a supersaturated solid solution. Upon heat treatment this single-phase alloy will decompose into a sequence of metastable and stable phases.

The precise precipitation sequence is a function of the alloy composition and the aging temperature, but usually follows the order:

Supersaturated solid solution (ssss) => GP zones => θ´´-phase (or GPII) => metastable θ´-phase => stable θ-phase.

The structure of these phases which form within the aluminum host lattice has been extensively investigated by diffraction methods since their first report. A generally accepted consensus concerning their atomic arrangement is illustrated schematically in Fig. 3.2.1a. [8]

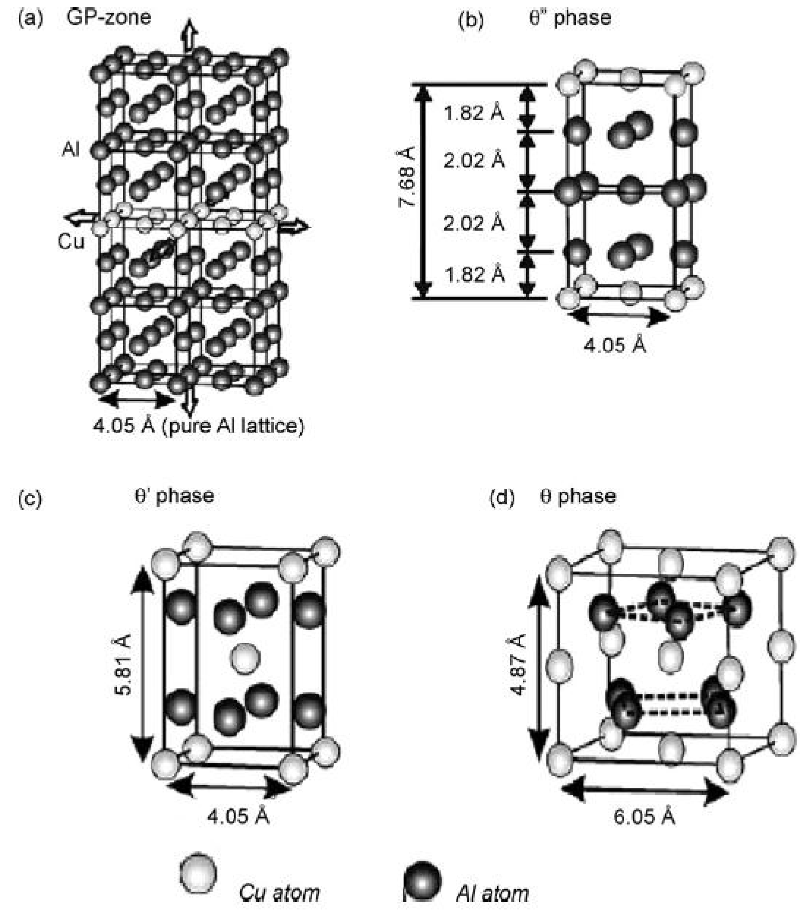

Fig. 3.2.1a: The crystal structures of the GP-zones, θ´´-phase, θ´-phase and θ-phase [8]

Guiner-Preston (GP) zones: They form in many alloys in the early stages of phase separation during the decomposition of supersaturated solid solutions. They have different morphologies (platelets, spheres, needles) depending on the difference in atomic diameters of solute and solvent elements. GP zones in Al-Cu alloys still attract much interest and definitive conclusions on their structure. It is widely believed that Guiner-Preston zones can consist of disks of Cu atoms, of order 40-200 Å (1 Å = 100 pm = 0,1 nm = 10^{-4} µm = 10^{-7} mm) in diameter, on substitutional sites on {100} planes in the fcc Al lattice. Because of the distinctly smaller size of Cu atoms (r_{Al}= 0.143nm and r_{Cu}=0.128nm) the matrix planes surrounding GP zones collapse towards the Cu layers.

θ´´-phase: With formal stoichiometry $CuAl_3$, consists of layers (disks) of Cu atoms in substitutional sites on {100} planes of the fcc Al lattice.

θ´-phase: Is a tetragonal distortion of the fluorite structure (Fig. 3.2.1a *(c)*) with axes aligned along those of the host lattice and is incoherent with it along the θ´-phase c-axis .

θ-phase: The ultimately stable structure, is a more elaborate distortion of the fluorite structure and is wholly incoherent with the host lattice, The structure is tetragonal, with one distinguishable Cu and Al atom per unit cell.

Taking into account the differences between these structures, the microstructural evolutions during heating of Al-Cu alloys, can be easily determined by using simple calorimetry analysis. [8]

The metastable solvus boundaries for GP zones, θ´´ and θ´, together with the equilibrium solvus line for the θ phase show Fig. 3.2.1b.

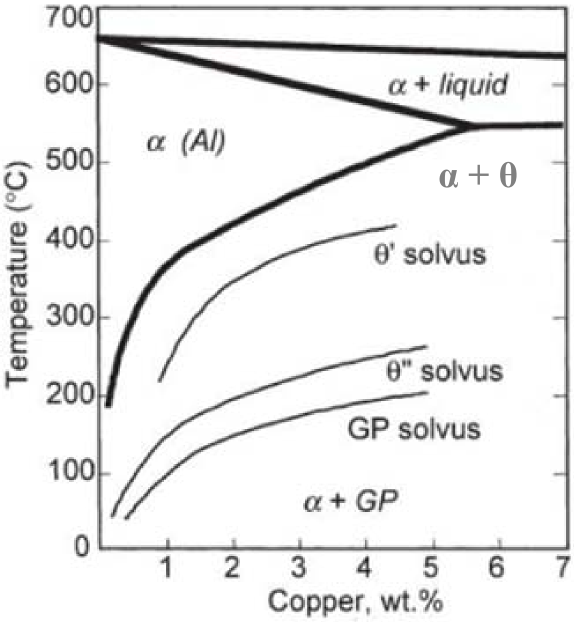

Fig. 3.2.1b: Al-rich corner of the Al-Cu phase diagram showing the different phases [9]

An important condition for hardening of an alloy is the decreasing solution with decreasing temperature of the basic metal aluminum for the alloying elements. The solubility of the α-solid solution for copper at the eutectic temperature (548°C) is 5,7%. It decreases with decreasing temperature and at 20°C, in the α-solid solution the copper is practical insoluble. During slow cooling from the area of the homogeneous α-solid solution, a precipitation of copper at the grain boundaries of the solid solution in form of the θ-phase ($CuAl_2$) occurs, see Fig. 3.2.1b.

The intent of solution heat treatment in the area of the homogeneous solid solution is the complete decomposition of the θ-phase in the solid solution matrix. Therefore the annealing temperature has to be higher than the solibility line of the α-solid solution. To avoid structure damage of the homogene solid solution, the boundary line to the phase (α+liquid) area must not be overstept during annealing.

During quenching in water, the diffusion processes of copper and aluminum atoms and in relation the precipitation process α => α + θ will be eliminated. The α-solid solutions which are supersaturated with copper, exist at 20°C and are metastable. A hardening effect has not appeared yet. At this condition, cold forming is applied to improve the hardening effect in the following aging step.

Depending on the aging temperature and time, the α-solid solutions decompose. At low aging temperatures this happens with the creation of Guiner-Preston I-Zones, a local accumulation of copper atoms which are coherent connected with the metal matrix. Higher aging temperatures enhance the diffusion processes and lead to the creation of partially coherent Guiner-Preston II-Zones (θ´´-phase). Too high aging temperatures lead to a creation of noncoherent precipitation of the θ-phase and therefore the Guiner-Preston II-Zones disappear. Both, Guiner-Preston I- and II-Zones (θ´´-phase) increase the tensile strength of the material. [10]

3.2.2 Study of DSC curves and hardness

Son et.al. have investigated very nicely precipitation behavior of Al-Cu alloys and for more clarification the results are brought partly here [11]. The compositions of the Al–Cu alloys prepared are given in Table 3.2.2. All specimens used for the experiments were solution-treated for 60min at 550°C and quenched in ice-water. Artificial aging was conducted consecutively at 130°C for various periods using oil-baths. A Shimadzu HMV-2000 Vickers microhardness tester was conducted with a test force of 0.98 N. The DSC measurements were made using a Rigaku TAS300-8230D apparatus with a heating rate of 10K/min. [11]

Table 3.2.2: Alloy compositions of the Al–Cu specimens in at% and wt% [11]

	C	E	G	H	J
Cu [at%]	0,56	1,18	1,66	1,94	2,18
Cu [wt%]	1,28	2,70	3,80	4,44	4,98

Fig. 3.2.2a shows the Vickers microhardness (HV) curves for the five Al–Cu specimens (C, E, G, H and J) aged at 130°C. Specimen C changes little over the annealing time. The HV curve for specimen E increases proportionally until 1.0x10^7s, and then slowly decreased. The hardness curves for specimens J, H and G with high copper contents exhibit a similar tendency. The curves show five stages up to 3.6x10^7s. The hardness increased at the first stage, but the increase of the HV curves stopped at the second stage after about 5x10^3 s. At the third stage, the curves rose again and peak hardness was attained. After reaching the peak, the curves slightly decreased at the fourth stage and finally the hardness rapidly dropped at the fifth stage.

Fig. 3.2.2b shows the DSC curves for an Al–4,44Cu (wt%) specimen aged for different times (600s until 3,6x10^7s) at 130°C with a heating rate of 10K/min (0.167 K/s). [11]

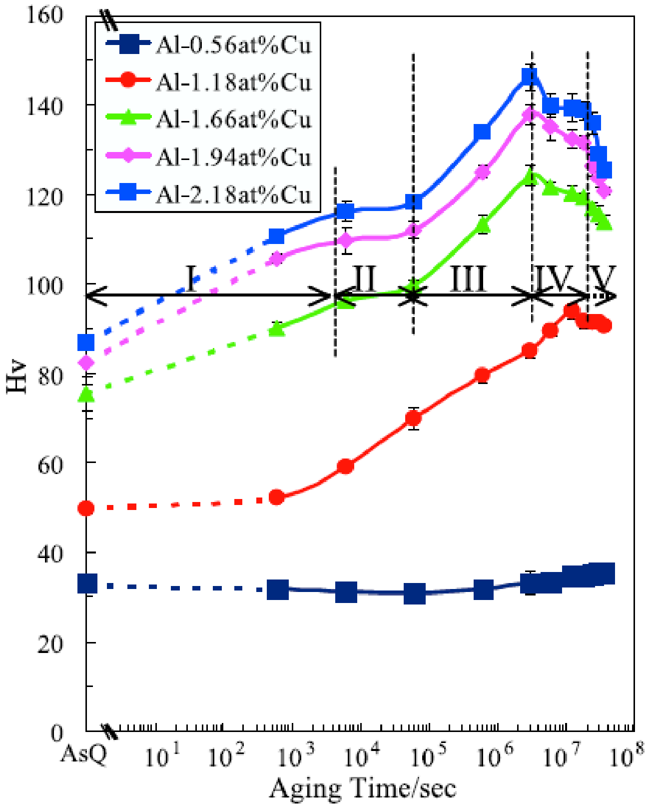

Fig. 3.2.2a: Vickers hardness of al-Cu specimens in isothermal aging at 130°C [11]

The DSC curves show six endothermic peaks appearing on dissolution of the stable/metastable phases which were previously formed during isothermal annealing. Through several previous investigations, the second endothermic peak b was attributed to GP I, the third peak c to GP II, the fifth peak e to θ´ and the sixth peak f to stable θ. The reason that the precipitates of peaks a and d were not explicitly recognized is probably due to the fact that the precipitate of peak a has a thermal stability and structure close to the zones of peak b, and the precipitate of peak d has a thermal stability and structure close to the zones of peak c, respectively, and they are simultaneously observed in X-ray diffraction experiments and TEM observations at the peak condition. Unlike the previous interpretation, the first peak a was named “quenched clusters” and the new fourth peak d, “the θ´´-phase”, which should be independent of GP II. [11]

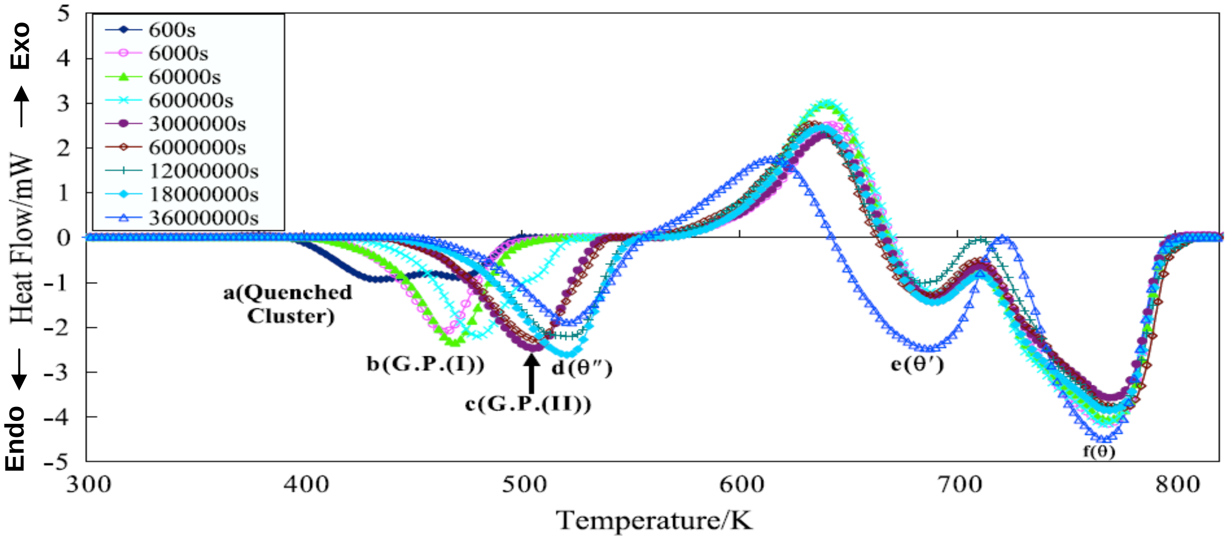

Fig. 3.2.2b: DSC curves of an Al–4,44Cu (wt%) alloy aged at 403 K with a heating rate of 10K/min [11]

A new interpretation of the precipitation behavior in an Al–Cu alloy was established, using a new terminology [11]:

Supersaturated solid solution (ssss) => quenched clusters => GP I => GP II

=> θ´´ (independent of GP II) => θ´ => stable θ

The structures of metastable phases are briefly described as follows. A quenched cluster is a monolayer Cu-rich plate approximately a few nm Cu in size. GP I is also a monolayer copper platelet, but is slightly larger than the cluster. GP II and θ´´ are bilayer and multilayer structures, comprising at least three copper-layers, respectively. θ´ is a thick planar precipitate. The Vickers microhardness was increased by the formation of quenched clusters and GP II, but the formation of θ´ explicitly caused a decrease in the hardness of an Al–Cu alloy during isothermal aging at low temperatures. GP I and θ´´ are formed at the intermediate stages which little influence the strength. [11]

3.3 Properties of Al-Cu-Mg alloys

3.3.1 Precipitation sequence

To characterize the precipitation processes that take place in a solution treated and quenched alloy during continuous heating at various heating rates, the differential scanning calorimetry is utilized. Fig. 3.3.1 shows typical non-isothermal DSC thermograms of the supersaturated Al-0.63Mg-0.5Cu-0.37Si (wt%) alloy performed at heating rates of 5, 10 and 30 K/min [12]. The DSC scans were carried out from room temperature to 527°C. Eight main processes can be identified from the DSC thermograms indicated by (I)–(VIII). Out of these processes, six are exothermic reactions labeled as I, II, IV, V, VI and VIII and two are endothermic labeled as III and VII. These reactions are shifted towards higher temperatures as the heating rate increases. This information indicates that these reactions are thermally activated. [12]

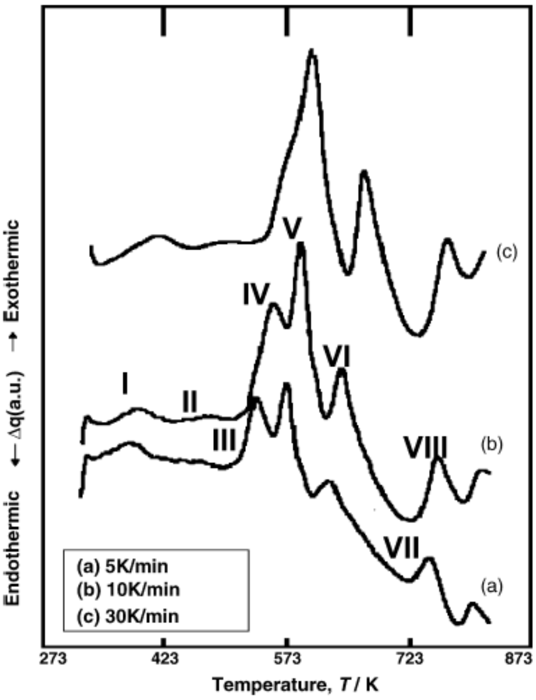

Fig. 3.3.1: Typical non-isothermal DSC thermograms of Al-0,63Mg-0,5Cu-0,37Si (wt%) performed at constant heating rates of 5, 10 and 30 K/min in the as quenched condition [12]

With respect to the DSC scan performed at 10 K/min, the above processes can be explained as:

I: The exothermic reaction I takes place at 385.5 K. This reaction can be ascribed to the early stage clustering of Si–Mg-Vacancy clusters and nucleation of G.P.zones.

II: Reaction peak I is followed by a very broad peak located at 460.5K for the specimen heated at a heating rate of 10 K/min. This broad peak is attributed to the precipitation of random precipitates.

III: The endothermic process III, could be attributed to the dissociation of vacancies and annealing out leaving behind the vacancy-free precipitates.

IV: The precipitation peak IV which has taken place at ~538K when heated at a rate of 10 K/min can be explained by the precipitation of ordered precipitates aligned parallel to the matrix. These precipitates might be the initial stage of nucleation of Q´ (Al-Mg-Si-Cu) precipitates. This nucleation is relatively rapid, as shown by the DSC thermogram (Fig. 3.3.1) which means that the activation energy of this reaction is relatively low, and consequently, its driving force is low. Therefore, this peak has a tendency to overlap with the next reaction peak as the heating rate increases.

V: The next exothermic reaction V appears at ~568K and is supposed to be due to the precipitation of Q´-phase. As it can be observed from DSC thermograms, that the reaction peak V of Q´ precipitates shifts towards higher temperature with increasing the heating rate slower than that of the preceding precipitates, so that the two reaction peaks IV and V overlap as the heating rate reaches 30 K/min and higher (curve c in Fig. 3.3.1). Consequently, one can predict the coexistence of the two types of precipitates when the alloy is heated at a rate of 30 K/min or higher to the corresponding peak temperature.

VI: The exothermic reaction VI occurred in the range 603.5–672 K and heating rates from 2.5 to 60 K/min. This reaction is characterized by the co-existence of β´ and S´ precipitates.

VII: Reaction VI is followed by an endothermic process, which can be explained by the dissolution of the preformed precipitates.

VIII: The peak of the exothermic reaction VIII shifts slowly with increasing the heating rate, which implies that this possesses has a high driving force. This reaction is attributed to the precipitation of large β-(Mg_2Si) precipitates. This reaction is followed by a dissolution endothermic process. This reaction shows, practically, slow or no shift towards higher temperatures with increasing heating rates. The reaction occurs at approximately a constant temperature of 775 K. This behavior indicates that this process is not thermally activated, but rather, is dominated by its temperature-dependent thermodynamic equilibrium. [12]

3.3.2 Study of DSC curves and hardness

During hardening in Al–Cu–Mg based alloys, DSC experiments clearly show a dissolution effect evidencing that a metastable pre-precipitate has formed.

Two commercial purity Al–Cu–Mg alloy plates with Cu:Mg ratio close to 1 (atomic ratio) have been studied [13], the compositions are reported in Table 3.3.2. For both alloys, 99.90wt.% aluminium was used as base to ensure comparable impurity contents that reflect commercial alloys of relatively high purity. Fe and Si contents of the alloys are expected to be between 0.02 and 0.03at.%. All samples were solution treated at 495°C and subsequently quenched in water at room temperature before the aging treatments commenced. Room temperature aging was performed at about 25°C.

Table 3.3.2: Composition of the alloys [13]

Alloy	Cu (at%)	Cu (wt%)	Mg (at%)	Mg (wt%)	Mn (at%)	Mn (wt%)
Al-1,2Cu-1,2Mg	1,21	2,77	1,19	1,09	0,21	0,42
Al-1,9Cu-1,6Mg	1,89	4,32	1,56	1,43	0,21	0,42

DSC runs were carried out over the temperature range 5–540°C at a constant heating rate of 10K/min, see Fig. 3.3.2b [13]. Vickers hardness tests were performed on quenched and naturally aged specimens. The hardness evolution during room temperature aging at 25°C of solution treated samples shows hardening within a few hours, see Fig. 3.3.2a.

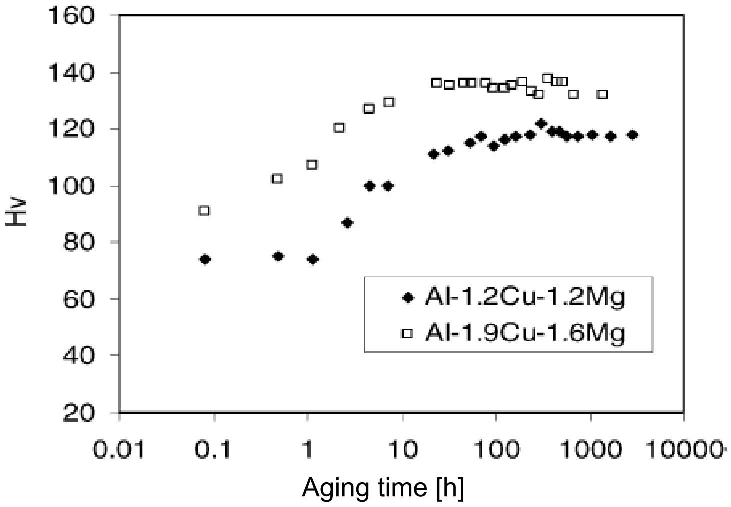

Fig. 3.3.2a: Age hardening of the Al-Cu-Mg alloys at 25°C [13]

DSC curves for the Al–1,9Cu–1,6Mg (at%) alloy after aging at 25°C show four effects (two exothermic and two endothermic), numbered I–IV. Effects III and IV can be identified as due to S phase formation (Effect III, in the range of 230–320°C) and S phase dissolution (Effect IV, in the range of 330–470°C). These effects are unrelated to rapid aging.

Effect I is thought to be due to the formation of Cu–Mg co-clusters. Comparison of Fig. 3.3.2a and Fig. 3.3.2b shows that the progress of this reaction coincides with the increase in hardness. Effect II is thought to be due predominantly to dissolution of clusters [13].

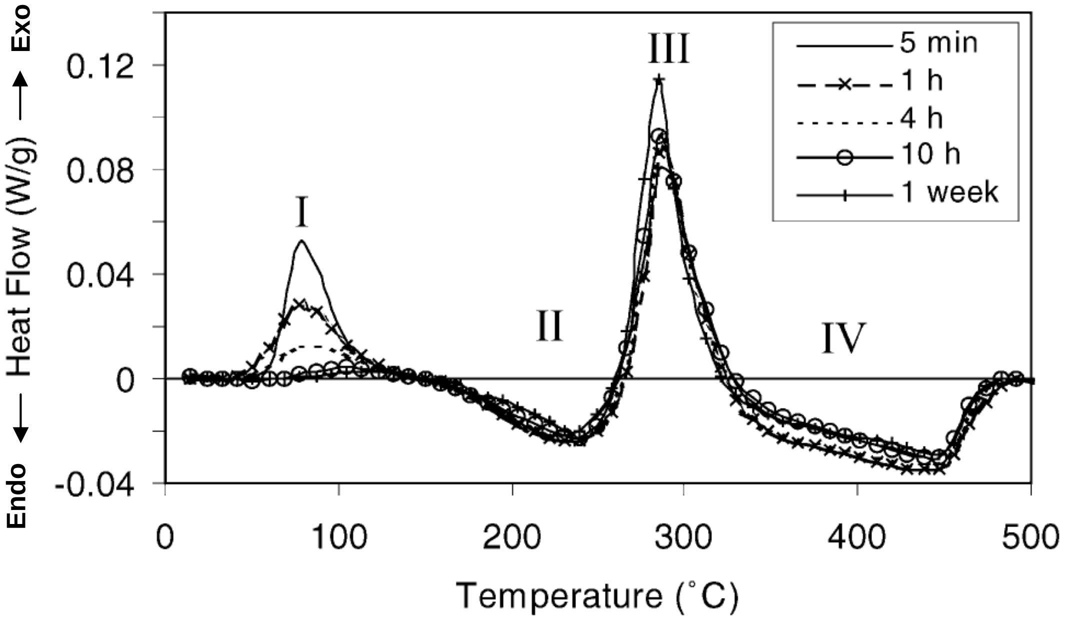

Fig. 3.3.2b: Curves of the Al-1,9Cu–1,6Mg (at%) alloy after aging for several intervals at 25°C [13]

3.3.3 Properties of 2024 and 2324 aluminum alloys

In the early 1950s, Guiner-Preston Bagaryatsky first proposed a four-stage precipitation sequence for the aging of Al–Cu–Mg alloys [14]:

SSSS => GPB zone => S´´/GPB2 => S´ => S ($CuMgAl_2$)

SSSS stands for supersaturated solid solution and GPB stands for Guiner–Preston Bagaryatsky. Bagaryatsky considered the GPB zone to be a short-range ordering of Cu and Mg solute atoms. The structure of S´´/GPB2 has not been clearly confirmed. Orthorhombic, cubic, tetragonal and monoclinic structures have been proposed for the S´´/GPB2 structure. An S phase with a composition of $CuMgAl_2$ has been determined as an orthorhombic structure. The S phase is an equilibrium phase and is incoherent with the Al matrix. The S´ phase has generally been considered as semi-coherent with the matrix, possessing the same structure as the S phase but with slightly different lattice parameters. As the proposed S´ structures have essentially the same crystal structures as the S phase, with very small differences in lattice parameters, many recent publications make no distinction between the S´ and S phases [14].

The chemical compositions of the AA2024 and AA2324 alloys studied in reference [14] are given in Table 3.3.3a. The Si and Fe contents are close to the maximum allowable for the two alloys. The alloys were supplied in the form of 13 mm plate in T351 condition.

The temper designation T351 indicates the following: T3 means solution heat treated, cold worked and naturally aged to a substantially stable condition. Tx51 (of which T351 is one example) is an additional designation used specifically for plate, rolled or cold-finished bars, die or ring forgings, or rolled rings that have been stress relieved by stretching. Typical values of permanent set after stretching are 1.5–3% for plate, 1-3% for rod, bar, shapes, or extruded tubes, and 0.5-3% for drawn tubes. No further straightening is applied after stretching. [15]

Table 3.3.3a: Chemical compositions of AA2024 and AA2324 alloys in wt% [14]

Alloy	Cu	Mg	Mn	Si	Fe	Al
AA2024	4,19	1,5	0,62	0,49	0,48	Bal
AA2324	4,19	1,5	0,62	0,08	0,06	Bal

Table 3.3.3b shows the heat treatments and working performed on the samples. For all treatments, slices of initially about 3 mm thickness and diameter about 5 mm were used. [14]

Table 3.3.3b: Heat treatments for DSC samples [14]

Designated names for heat treatments	**Details**
T351	Solution treated at 495°C, quenched, stretched 1.5–3% and aged at room temperature for several months
WQ	T351 + solution treated at 495°C for 30 min + water quenched
WQ+cold worked	T351 + solution treated at 495°C for 30 min + water quenched + immediately cold worked by 10%

All solution treatments were performed at 495°C. Cold working was achieved by uniaxially compressing the samples (essentially a miniature cold forging) to reduce the thickness by 10%. DSC runs were performed using a Perkin–Elmer Pyris 1 apparatus at a constant heating rate of 10°C/min. The reference sample was an empty pure aluminium pan. Tests were carried out using a nitrogen gas flow. All presented DSC curves reflect the heat flow due to reactions. Due to the strong differences in the DSC curves from the different samples, slight inaccuracies in baseline determination in the order of $\pm 5 \times 10^{-3}$ W/g may remain. DSC experiments on all samples except the as-received T351 sample were started within 1 min of the final treatment.

Fig 3.3.3a shows the DSC curves of the AA2324 alloy in three different conditions. Five main effects may be identified in these thermograms: an exothermic peak, A, between 60 and 110°C, is due to the formation of co-clusters; an endothermic effect, B, between 160 and 240°C, may be attributed to Cu–Mg co-cluster dissolution (with possibly some GPB2 dissolution); an exothermic effect, C (containing two overlapping reactions; see below), between about 230 and 340°C, is attributed to the formation of S phase precipitates; a broad endothermic effect, D, at 340–500°C, is identified as progressive dissolution of the S precipitates; and an endothermic sharp peak, E, between 505 and 515°C, is believed to be due to the partial melting of S + θ eutectics.

It is commonly accepted that there are three ways to form an S phase:

- by heterogeneous nucleation from vacancy loops
- by heterogeneous nucleation on dislocations

- by transformation of or nucleation on the intermediate precipitate S´´

Si inhibits the formation of vacancy loops during/after quenching, and therefore suppresses the availability of heterogeneous nucleation sites. [14]

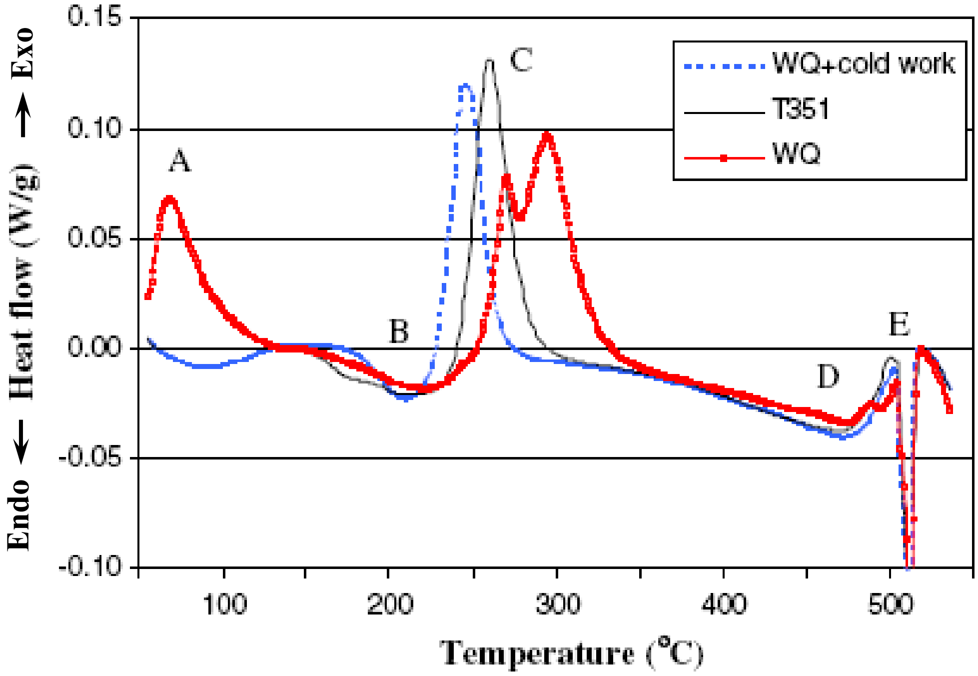

Fig. 3.3.3a: DSC thermogram of the AA2324 alloy in T351, WQ and WQ+cold worked conditions [14]

In this study, basically exothermic effect C is analyzed. For the deformed samples, T351 (1.5–3% stretch) and WQ+cold worked, exothermic effect C shows only one single peak. This peak shifts to lower temperature with increasing deformation. This is considered to be due to an increase in heterogeneous nucleation sites for S phase (predominantly dislocations). In contrast, the sample in the WQ condition shows two distinct peaks. To confirm which kind of precipitates are responsible for these two exothermic effects, the samples were heated in DSC at a heating rate of 10°C/min up to 270 and 400°C respectively. Then the samples were prepared and observed in TEM. The combination of DSC and TEM experiments in Al–Cu–Mg alloys confirm the existence of two distinct S phase precipitates, which correspond to two exothermic DSC effects in solution treated samples between 230 and 350°C (see Fig 3.3.3b).

Fig. 3.3.3b reveals that two exothermic peaks appear in both curves: the first peak C_I is due to the formation of Type I precipitates and the second peak C_{II} is due to the formation of Type II precipitates. The peak temperatures for the formation of Type II precipitates (peak C_{II}) does not vary significantly between the AA2024 and the AA2324 sample:

~296°C for AA2024 alloy with 0.49 wt.% Si and ~300°C for AA2324 alloy with 0.08 wt.% Si. However, the increased Si content enhances the amount of Type I S phase forming and reduces the amount of Type II S phase forming. [14]

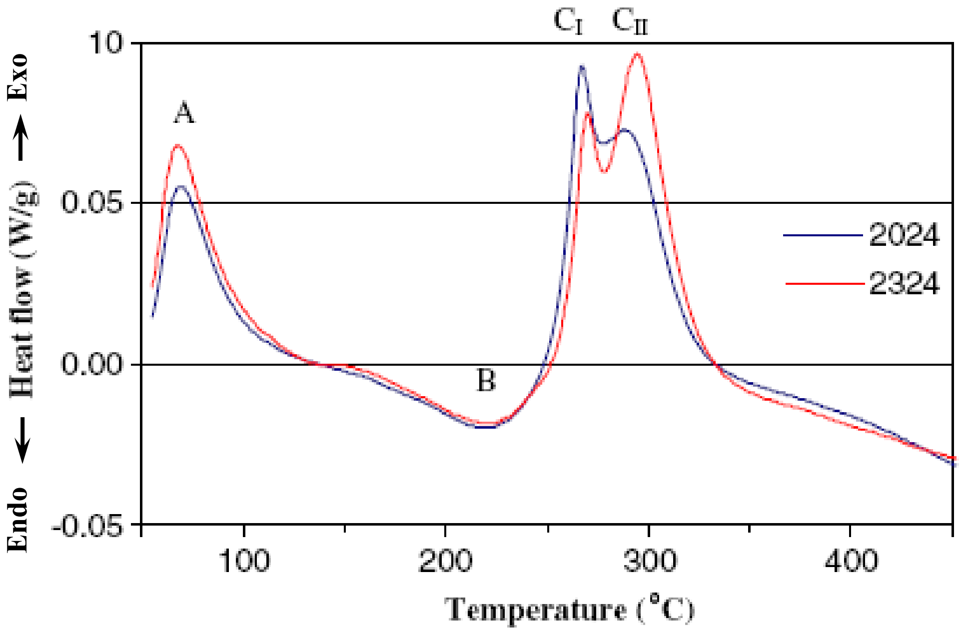

Fig. 3.3.3b: DSC thermograms of AA2024 and AA2324 alloys in WQ conditions [14]

Combining the present findings with further literature, the sequence for the formation of S phase by homogeneous nucleation is suggested to be best represented as [14]:

SSSS => GPB zone => S´´/GPB2 => S (Type I) => S (Type II)

In solution treated, quenched and subsequently cold worked samples, extensive formation of Type I occurs, whilst formation of Type II is suppressed. The formation of Type II phase precipitates is strongly dependent on solution treatment and cold work. Type II phase has random interfaces with the matrix, which indicates that the transformation from Type I to Type II is not the result of an invariant line transformation strain. [14]

To have an idea about solution treatment temperature, it is of interest to find the temperature at which the first liquid fraction appears. Fig. 3.3.3c shows the liquid fraction in % for Al 7075, Al 2024 and Al 6061 wrought alloys obtained from DSC analysis. In Al 2024 alloys, liquid fraction appears first at about 534°C and the curve rise steeply after 620°C. [16]

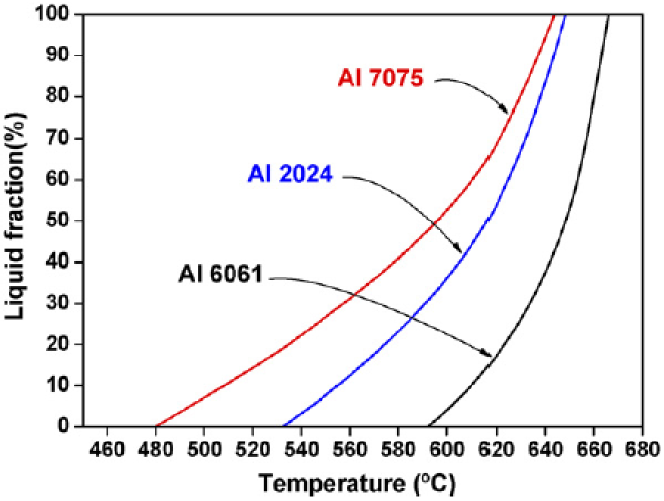

Fig. 3.3.3c: The curve of liquid fraction vs. temperature in wrought aluminum alloys [16]

3.4 Direct chill and electromagnetic casting

The principle of electromagnetic casting (EMC) and direct chill casting (DCC) are shown in Fig. 3.4a. The main parts of the EMC equipment is the shaping system composed of inductor, screen, cooling water box and bottom block. Other parts consist of delivery system, casting control system, melt furnace and power supply, etc. The interaction of alternating magnetic field and induced current generates the electromagnetic force directed toward the center of ingot. This force located within the upper liquid part of the ingot prevents the metal from touching the mold. A metal ring screen is used to control the magnetic field on the top of the melt, to keep the balance between the electromagnetic pressure and the hydrostatic pressure. After adjusting the position of the inductor, screen, water jacket, and bottom block, the cooling system is operated and then the power supply is turned on. Molten aluminum flows through a metal delivery system into a pool of liquid metal above the previously solidified aluminum. [17]

The main parts of the DCC equipment are: 1 - feed trough, 2 – nozzle, 3 – float valve, 4 – distributor, 5 – mold, 6 – solidifying ingot, 7 – sump, 8 – water cooling sprays, 9 – stool cap, 10 – stool. Liquid metal flows through a nozzle into the hollow, formed by the water-cooled mold. The hydraulic ram starts to descend slowly and water sprays on the thin solid skin. [18]

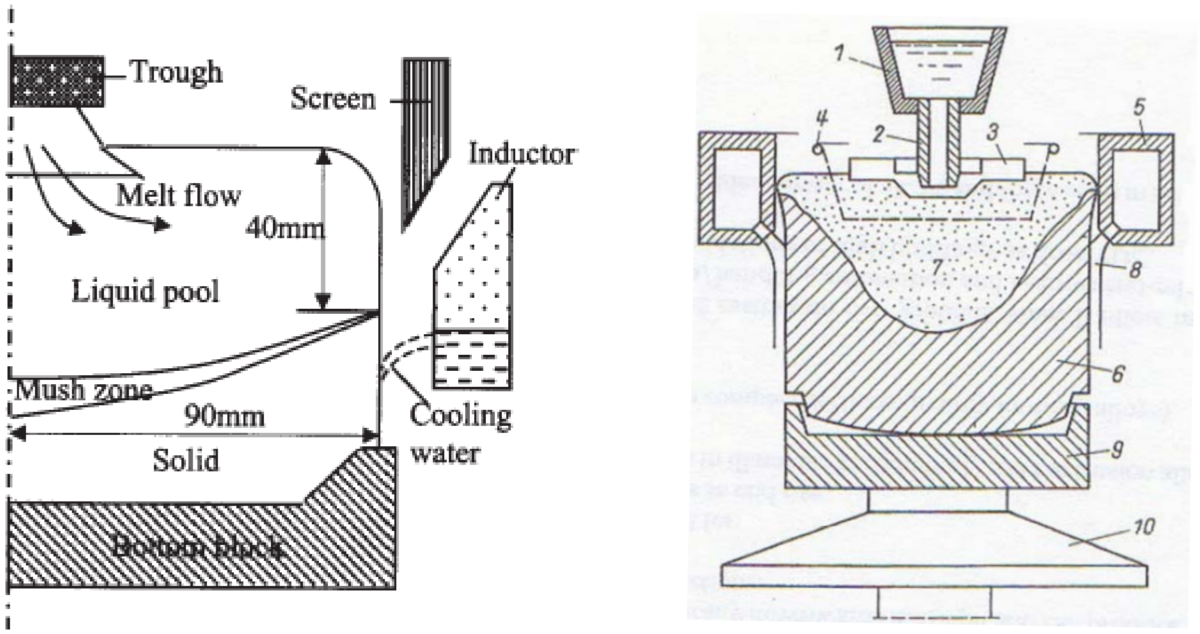

Fig. 3.4a: Principle of electromagnetic casting (on the left) and direct chill casting (on the right) [17, 18]

The distinct advantages of the electromagnetic casting (EMC) process consist in the presence of stirring motions in the melt, which lead to significant grain size reduction in solidified ingot. Furthermore, surface and subsurface qualities are improved due to the absence of ingot mold. However, it is impossible to achieve the aforementioned advantages in conventional direct chill casting (DCC). In order to contrast the before and after heat treatments of the microstructural and mechanical characteristics of EMC and DCC 2024 aluminium alloys, optical microscopy, scanning electron microscopy, transmission electron microscopy (TEM), X-ray diffractions (XRD), differential scanning calorimetry (DSC), etc. were carried out. Compared with the DCC ingot, the EMC ingot has better mechanical properties not only in the as-cast condition but also in the as-aged condition.

Figure 3.4b shows the transverse sectional grain structures of 2024 DCC and EMC specimens in the as-cast state. It is clear that the grains of EMC are small and equiaxed, no matter at edge, midthickness, or center of ingots. In the DCC condition, the grain size becomes coarse from the surface to the center of the ingot. This is due to its higher cooling rate at the ingot surface area. This situation is different from the EMC process. In the EMC process, the grain is more homogeneous over the entire cross section of the EMC ingot. [17]

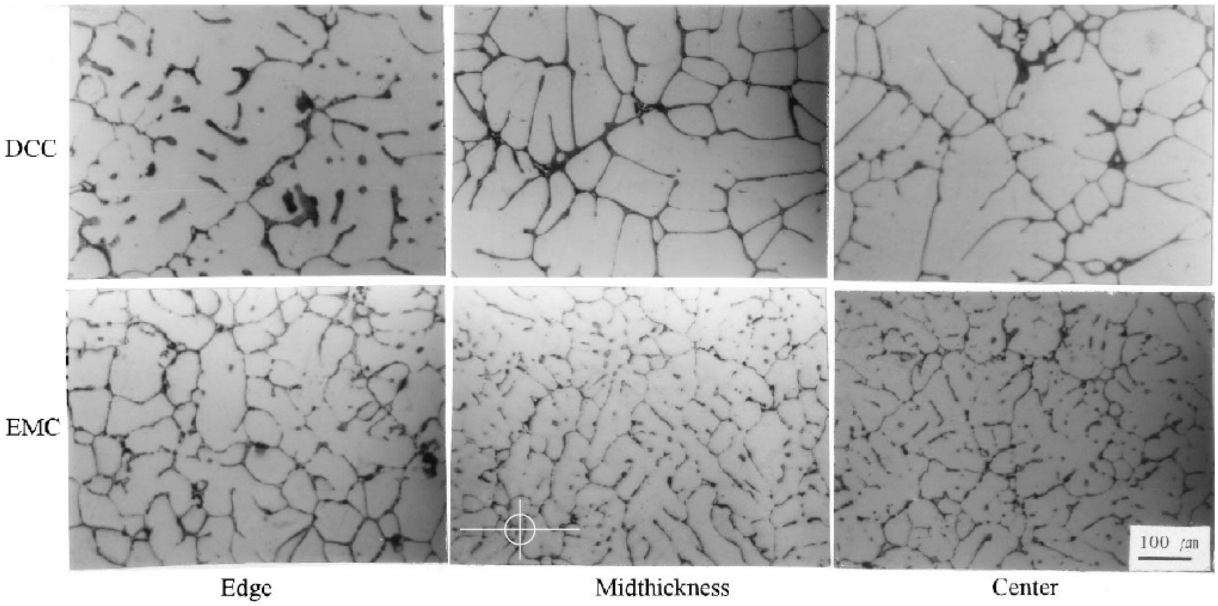

Fig. 3.4b: Microstructural comparison of 2024 DCC and EMC ingots at as-cast state [17]

DSC curves showed that the EMC specimens have high enthalpy, i.e., the thermal kinetic energy to form precipitates during the aging treatment process. Despite heat treatments applied to the DCC ingot, it fails to attain the same mechanical properties as the EMC ingot. Moreover, considering the expensive scalping operation for DCC ingots, the EMC technique, which offers a lower manufacturing cost, is one of the best manufacturing methods used in obtaining the ingots of wrought aluminum alloys. [17]

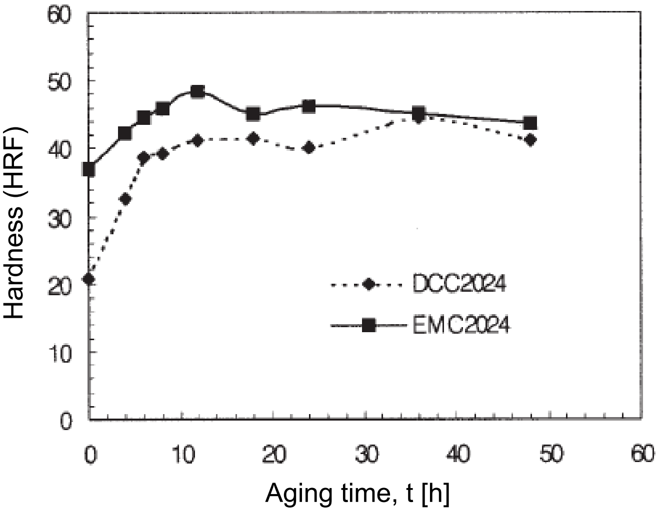

Fig. 3.4c: Age-hardening curves of EMC and DCC 2024 alloys at room temperature [17]

The age-hardening curves at room temperature for the 2024 alloy are plotted in Fig. 3.4c. The hardness of EMC specimens is 2 times higher than that of the DCC ones in the as-cast state, owing to the much finer grain structure of the former. The increase in hardness with aging time is due to precipitation of the GP zones and other intermediate phases.

The EMC specimens reached a peak of 48.52 at around 12 hours, while the DCC ones reached their peak of 44.4 after 36 hours room temperature aging. This means that the EMC ingots display faster kinetics of precipitation, compared with the DCC ones, because of the difference in cooling time. [17]

3.5 Homogenization

In most cases, concentration differences during solidification lead to the formation of segregation gradients. The segregation gradients can be dissolved through homogenization which means holding at a temperature of about 0,7–0,8 x T_M (T_M....temperature of first melt) for a long time. The workability of the cast ingot is determined by chemical composition, microstructure, heat treatment and mechanical process. The microstructure is effected by homogenization temperature and cooling rate. For example in a 2014 aluminum alloy, intermetallic phases like AlFeSi, Cu_2MnAl, $CuAl_2$ and Mg_2Si may occur. $CuAl_2$ phase, the hardest phase, is dissolved with increasing temperature, specifically above 450°C. Hot deformation of homogenized ingots is easier than that of nonhomogenized ingots. In addition, the surface of the product obtained is smoother. Because the goals of the deformation stage are the highest manufacture rate but the lowest stress value, the ingot needs to be homogenized after casting, and heated to the deformation temperature. [19]

Wrought aluminum alloys are often given a homogenization heat treatment before extrusion or rolling. Foundry alloys are sometimes given a solution heat treatment before age hardening. The purpose is:

- to remove particles and segregation gradients that will give films or areas with low melting temperatures, in order to avoid tearing during extrusion and rolling
- to round off hard particles with sharp edges, which give poor ductility and holes in thin walled products
- to form secondary particles (dispersoids) for grain size control during extrusion and rolling;
- to obtain a uniform distribution of alloying elements in solid solution before rolling, extrusion or age hardening.

Industrial homogenization for aluminum is a two- or three-step process, with heating, holding at high temperature and often subsequent cooling. When the heating starts at room temperature, the solid solution is strongly supersaturated. The first reactions are nucleation and precipitation. Many of the freshly formed precipitates redissolve at higher temperature, and tare thus of little industrial interest, but they may serve as nuclei for other particles. The freshly formed particles that tend to survive a successful homogenization are Fe-, Cr-, Mn, and Zr- bearing dispersoids, although a high fraction may dissolve before the holding temperature is reached.

In some cases the next reaction during heating is local melting. Industrial solidification is so fast that there is little time for solid-state diffusion, which means that the last liquid to solidify may contain eutectic composition. Rapid heating will result in remelting at the same temperature, even though the equilibrium solidus temperature of the alloy may be several tens of degrees higher. Slower heating will give the low-melting phases time to dissolve. When a whole batch of cold rolling slabs or extrusion billets is heated together, the heating takes time, and the rate of heating is determined by the capacitiy of the furnace. With modern furnaces where extrusion billets are introduced one by one, the rate of heating becomes a point of consideration. The holding temperature is usually chosen as high as possible, with a reasonable safety limit relative to the equilibrium solidus temperature of the alloy. Lower temperatures may be used if a high density of Cr-, Mn- or Zr-bearing dispersoids is wanted.

Billets and solution heat-treated net shape cast components are cooled without deformation. Rolling slabs are deformed during the cooling stage when new particles will nucleate and grow. Vacancies will disappear during slow cooling without deformation in billets and net shape castings, but form, together with dislocations and subgrains, during the rolling of slabs. Precipitation of Mg, Si and Cu as particles during the cooling is mainly undesirable, the removal of these phases was the original objective of the homogenization. For economical reasons, industrial heat treatments should be as short as possible. This is not easy to combine with slow heating, long holding and may be even slow cooling. Optimizing the homogenization process is therefore a science of compromises. [20]

4 Experimental

4.1 Materials

In Table 4.1, the properties of the aluminum alloys are summarized to provide an overview.

Table 4.1: Overview of the used aluminum alloys

Designation	**Alloying elements [wt%]**	**Origin**
Sample 1	3,85Cu	Manufactured in our own laboratory
Sample 2	3,85Cu	
Sample 3	4,3Cu	
Sample 5	4,3Cu	
Sample 6	4,3Cu	
Sample 4	4,3Cu, 1,49Mg	
Sample 7	4,3Cu, 1,49Mg	
AA 2024	4,3Cu, 1,49Mg, 0,71Mn, 0,13 Fe, 0,07Si, < 0,01 Cr and Ni	Industrial

4.2 Equipment and general test conditions

4.2.1 Induction furnace

Generally, the Lifumat10 induction furnace with a capacity of 10kW was used to melt the material in a crucible. The frequency range of the furnace deviates between 7 and 29 kHz and it regulates automatically, depending on the material which is heated (see Fig. 4.2.1).

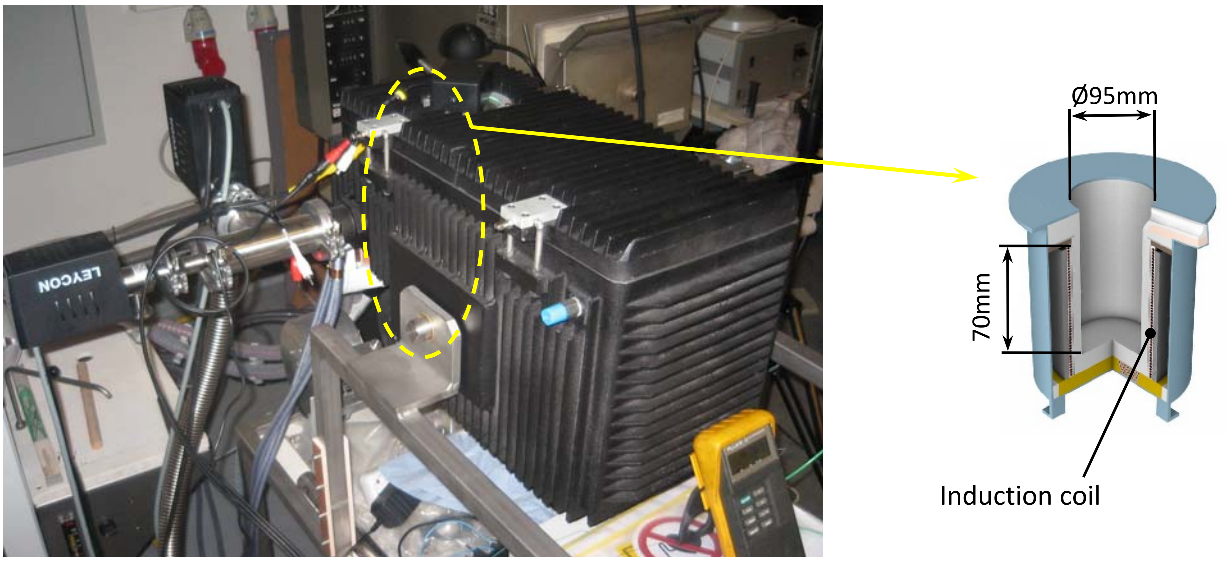

Fig. 4.2.1: Lifumat10 induction furnace

The induction coil can be controlled manually or with a temperature regulator. For pilot-controlling, the temperature in the crucible has to be measured.

4.2.2 Crucibles

The properties of different materials which were available to be used for crucibles are listed in Table 4.2.2.

Table 4.2.2: Physical properties of crucible materials [21]

Physical properties	**Material**		
	Graphite (pyrolytic 2.19)	SiO_2 (Composition: 17.1% SiC, 13.6% Al_2O_3, 1.8% other)	Boron nitride (hot pressed, commercial purity)
Density [kg/m^3]	2150 – 2230	2400 – 2540	2230-2270
Price [€/kg]	8 – 13	14 – 21	26 – 40
Max. service temperature [°C]	2350	1490	1640
Fracture toughness [MP*m^1/2]	2,4 – 2,6	3,3 – 3,7	2,5 – 5
Thermal conductivity [W/(m*K)]	100 – 250	43 – 55	24 – 30
Dielectric breakdown [MV/m]	-	9,6 – 10,4	35 – 45
Electrical resistivity [µOhm*cm]	34,7 – 6030	$1*10^{12} – 1*10^{13}$	$3,16*10^{20} – 3,16*10^{21}$

In comparison: aluminum has a thermal conductivity of 200 – 234 W/(m*K) and an electrical resistivity of 3,6 – 3,8 µOhm*cm. [21]

The dimensions of the used graphite and boron nitride crucible are illustrated in Fig. 4.2.2.

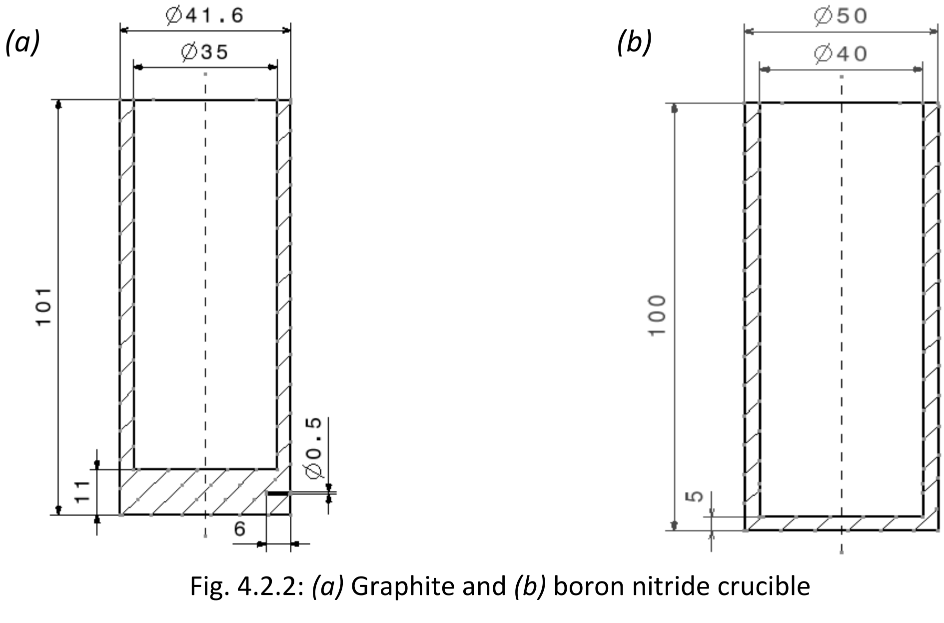

Fig. 4.2.2: *(a)* Graphite and *(b)* boron nitride crucible

4.2.3 Extruder

Extrusion was carried out at the “Institut für Chemische Technologien und Analytik“. The extruder used was from the company “V. Jessernigg u. Urban” with an operating pressure of max. 290 bar, see Fig. 4.2.3. The recipient of the extrusion machine has a defined diameter of 40mm.

Fig. 4.2.3: Extruder (Type Str. Pr. 200MP)

4.2.4 Light microscopy

The used device: (Zeiss Axioplan) has five lenses which allow different magnification rates. Additionally a magnification of 10x was obtained through the ocular. That means a complete magnification of 25x, 100x, 200x, 500x and 1000x are possible.

Every specimen used for light microscopy analyses was grinded with a semiautomatic machine.

4.2.5 Scanning electron microscopy

Scanning electron microscopy “Type Philips XL 30 equipped with EDX” were used for more detailed investigations.

The parameters of the used electron microscopy are listed in Table 4.2.5.

Table 4.2.5: Parameters of Philips ESEM FEG XL 30

Parameter	**Value**
Acceleration voltage	200V – 30kV
Resolution	> 2nm
Vacuum cathodic room	< 10^{-11} Pa
Probe room	1333 Pa (10 Torr)... 10^{-9} Pa

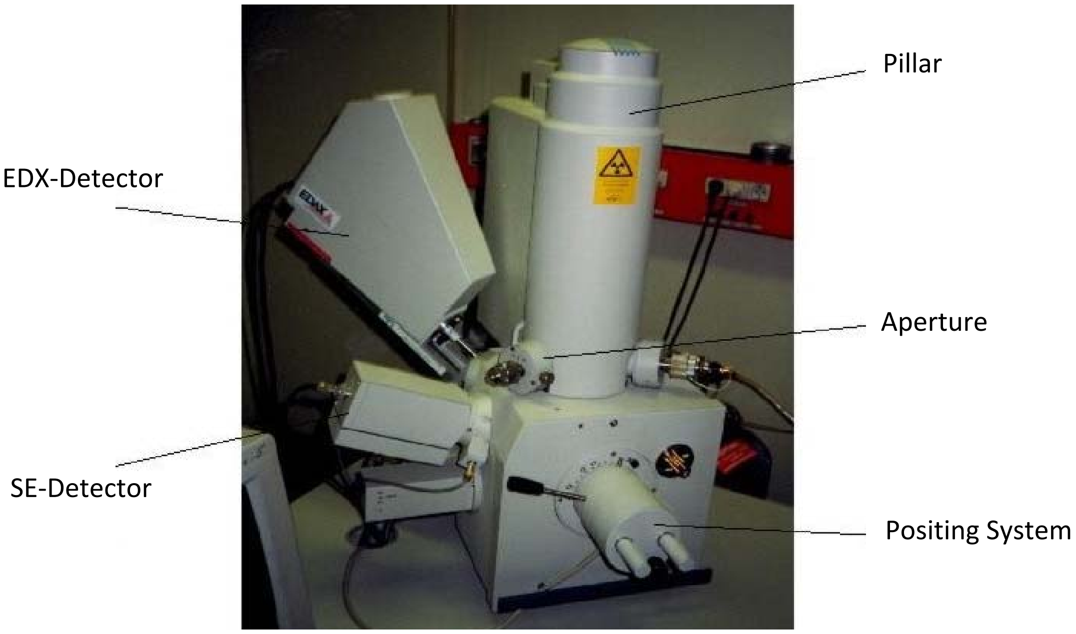

Fig. 4.2.5a: Philips ESEM FEG XL 30

EDAX (Energy dispersive X-ray spectroscopy), an analytical technique that uses characteristic x ray radiation for compositional analysis was used to quantify the chemical composition of the produced alloys.

A magnification rate of 50x was used for scanning electron microscopy to measure quantitatively the elements such as Al, Cu, Mg, Mn, etc. with EDX, see as example Fig. 4.2.5b.

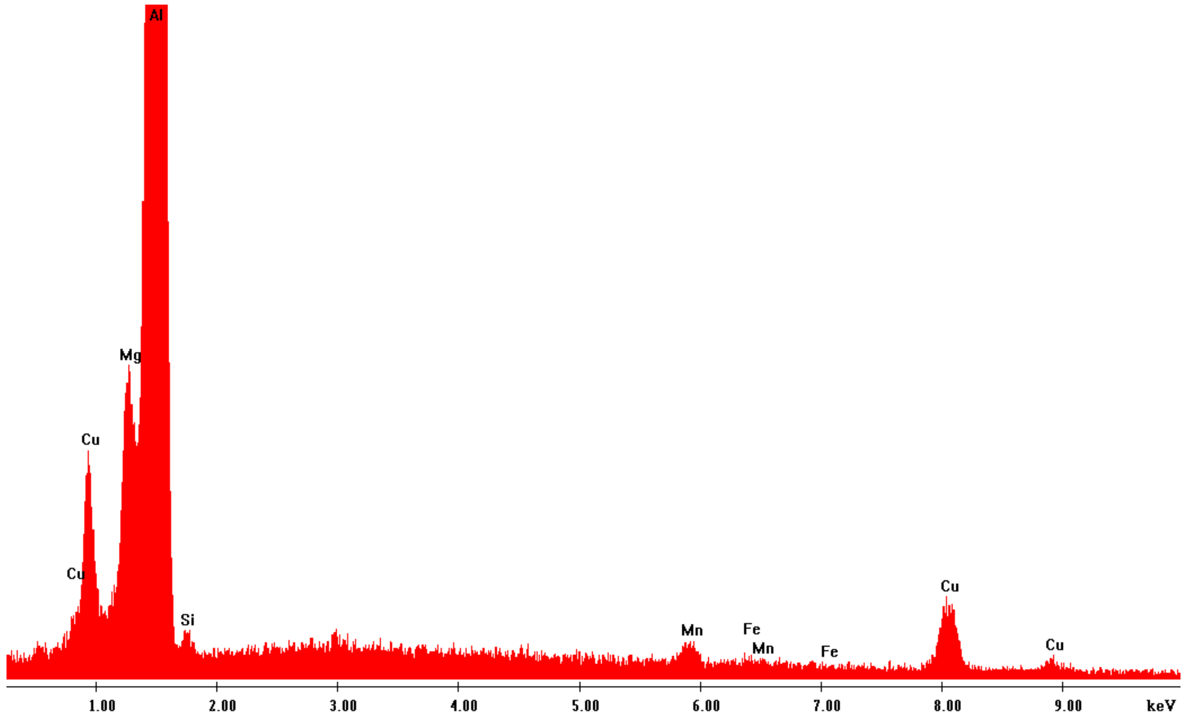

Fig. 4.2.5b: Example of an EDX analysis; determination of the components Al, Cu, Mg, Mn, Fe and Si

Determination of element occurrence with scanning electron microscopy is not 100% exact and accuracy of EDX spectrum can be affected by many variants. Every specimen used for scanning electron microscope analysis was grinded with a semiautomatic machine.

4.2.6 Hardness measurement

Hardness measurements were carried out with the durometer EMCO Test M1C 010 B. Details of the device are presented in Table 4.2.6.

Table 4.2.6: Parameters of EMCO Test M1C 010 B

Parameter	**Value**
Test loads	0,98 – 306 N 0,1 – 31,25kgf
LED lighting	0 – 12 mA
Frequency	50/60Hz
Safety class	IP20

Hardness measurements were carried out according to EN ISO 6501-1 (Brinell hardness).

- For extruded and rolled specimens, the hardness was measured with a sphere diameter of 1mm. A dwell time of 10s and a load level of 10 N (according to the standard for light metals) were chosen.
- For specimens in the as-cast condition, the hardness was measured with a bigger sphere diameter of 2,5mm. A dwell time of 10s and a load level of 15,625 N (according to the standard for light metals) were chosen.

The observation of the minimum displacement between test points (3 times diameter of the impression) and between test points and edge (2,5 times diameter of the impression) was considered.

4.2.7 Differential Scanning calorimetry

Differential scanning calorimetry analyses were carried out with a DSC 2920CE device according to the heat flux measuring principle, see Fig. 4.2.7a. High purity Al samples of the similar mass to that of the specimens were used as reference. During DSC measurements, the samples were protected with flowing nitrogen. Diameter of the DSC samples was 6,23 mm and they had been stamped from the prepared aluminum sheets.

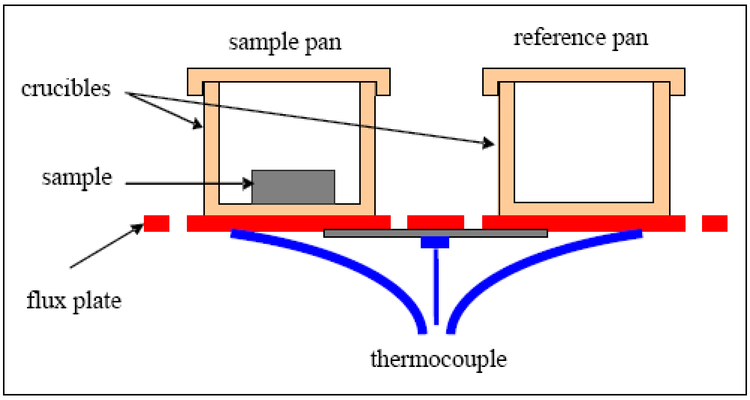

Fig. 4.2.7a: Schematics of a heat flux DSC [1]

In some cases, 3 different heating rates were used in the first run: 5, 10 and 20K/min (see Fig. 4.2.7b). Three different rates were used to gain knowledge about which heating rate is the best representative of the used alloy. For every heating rate the second run was carried out with the heating rate of 5K/min to check the validity of experiments because the second identical run should give the same DSC curve for each material.

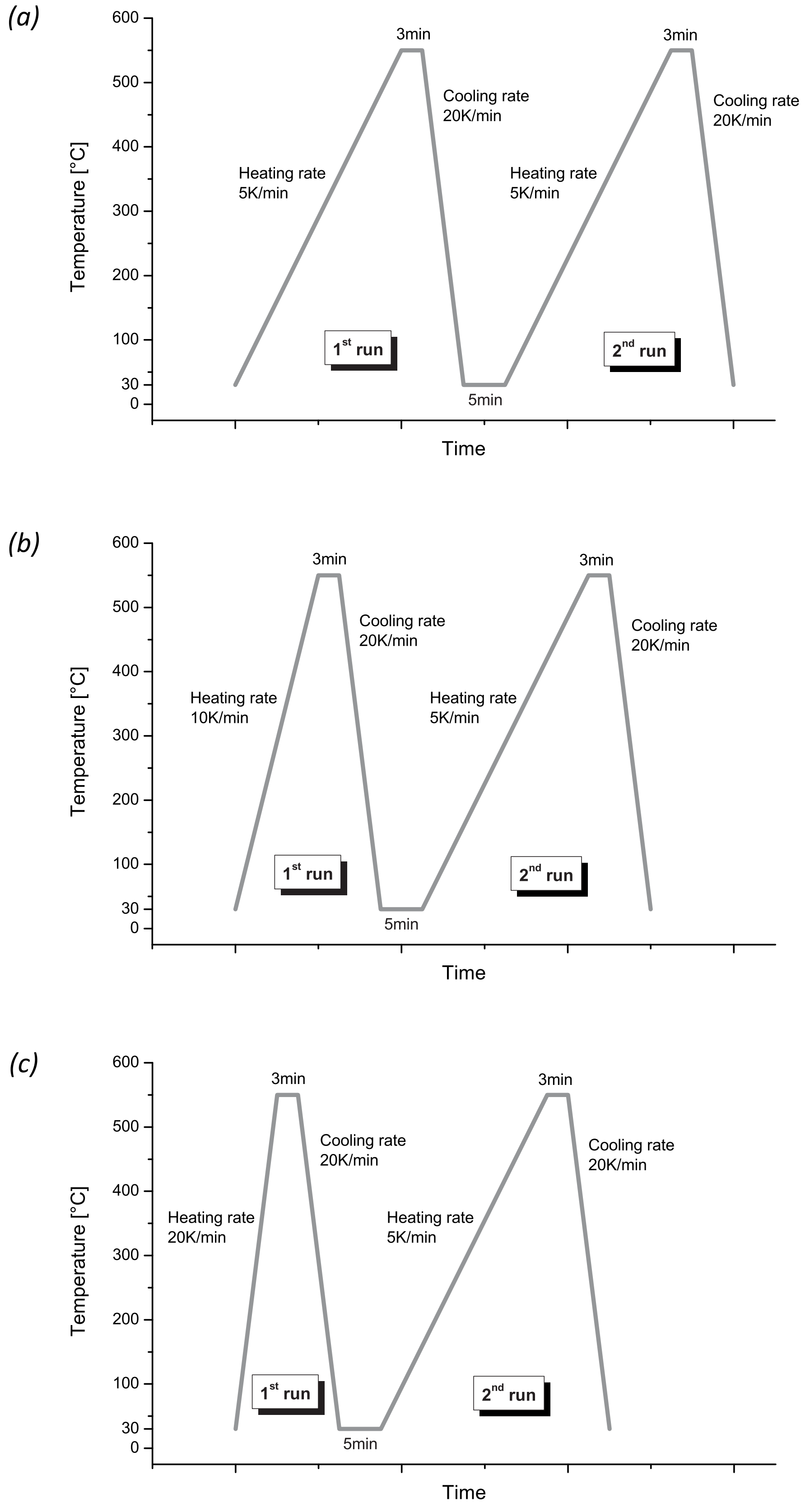

Fig. 4.2.7b: DSC cycles for different heating rates: *(a)* 5K/min, *(b)* 10K/min and *(c)* 20K/min

4.3 Manufacturing procedure

Using crucibles made out of different materials means crucibles with different physical properties that can affect alloying element distribution in the casts. By using the graphite crucible, because of high thermal conductivity, it was possible to measure the temperature of the melt by measuring the temperature of the graphite crucible. But, because of very low thermal conductivity of ceramic crucibles, the temperature measurement of the melt with the thermocouple contacting the crucible body was not possible and inserting the thermocouple in the crucible and contacting the solid metals was problematic.

For the first manufacturing process, a silicium oxide crucible with an inner diameter of 72mm was used to get more knowledge about the induction furnace. Afterwards, attempts with graphite crucibles were made because of the better thermal conductivity (100–250 W/(m*K)) of graphite compared to ceramic (5-30 W/(m*K)), temperature was measured by inserting a thermocouple in a drilled hole 5mm above the bottom of the crucible (see Fig 4.2.2). Further manufacturing attempts were made with a boron nitride crucible which had a higher inner diameter than the graphite one. For extrusion, a sample diameter of 40mm was most suitable.

Boron nitride (hot pressed, commercial purity) has an electrical resistivity of $3,16*10^{20}$ – $3,16*10^{21}$ µOhm*cm and graphite (pyrolytic 2.19) of 34,7 – 6030 µOhm*cm [21]. The higher electrical conductivity of the graphite crucible could have an effect on the stirring motions in the melt. Reducing stirring motions can have a negative effect on homogeneous distribution of the alloying elements.

In Table 4.3, the type of crucibles and furnace atmosphere of the manufactured Al-Cu and Al-Cu-Mg alloys are summarized to provide an overview.

Table 4.3: Manufacturing characteristics of sample 1 to 7

Designation	Composition [wt%]	Used crucible	Furnace atmosphere
Sample 1	Al-3,85Cu	Silicon oxide	Vacuum
Sample 2	Al-3,85Cu	Graphite	Vacuum
Sample 3	Al-4,3Cu	Graphite	Argon
Sample 5	Al-4,3Cu	Graphite	Vacuum
Sample 6	Al-4,3Cu	Boron nitride	Vacuum
Sample 4	Al-4,3Cu-1,49Mg	Graphite	Vacuum
Sample 7	Al-4,3Cu-1,49Mg	Boron nitride	Argon

4.3.1 Manufacturing of Al-Cu alloys

4.3.1.1 Al-3,85Cu manufactured in a silicon oxide crucible under vacuum

First experiment with first procedure: a silicon oxide crucible was used for the manufacturing of an Al-Cu alloy with 3,85wt% copper (named sample 1). Due to the fact that there was no knowledge about the furnace, aluminum with a purity of 99,85% was used for the first test. Pieces of copper and aluminum were put into the crucible. The performance of the induction coil was pilot-controlled. Therefore, the temperature had to be measured with a thermocouple. Due to the crucible´s low thermal conductivity value, the thermocouple was directly dipped into the crucible contacting the metal to measure the temperature.

Composition of the alloy: 240,0g Al with a purity of 99,85%

9,6g Cu => that gives an Al-Cu alloy with 3,85wt% copper

The temperature regulator was set to 700°C and heating was started at a vacuum of $5,2x10^{-2}$ mbar. During heating, the thermocouple sensor was not able to withstand the heat and melted. Therefor a temperature measurement was not possible anymore and the induction furnace was switched off. Both materials (aluminum and copper) stayed in the solid form. The reason why the heading of the thermocouple melted was it´s misalignment directly in the crucible.

First experiment with second procedure: It was carried out without a temperature regulator. The temperature was regulated manually and the melt was observed through the inspection glass. The induction furnace was switched off 10 minutes after both materials were molten. During cooling and after the melt solidified, the vacuum pump was shut down. In this procedure, no knowledge could be obtained about the temperature at which the alloy will be melted and can be manufactured.

4.3.1.2 Al-3,85Cu manufactured in a graphite crucible under vacuum

In the second experiment, a graphite crucible was used for the manufacturing of an Al-Cu alloy with 3,85wt% copper (named sample 2).

Aluminum in the form of small rectangles (see Fig. 4.3.1.2a) with a purity of 99,99% was used. The copper was put on the top of the aluminum (see Fig. 4.3.1.2b).

The thermocouple was inserted in the bottom hole of the crucible contacting the crucible wall.

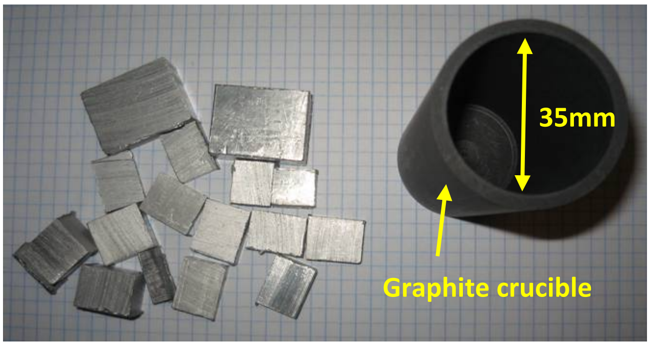

Fig. 4.3.1.2a: Aluminum rectangles and graphite crucible

Composition of the alloy: 140,4g Al with a purity of 99,99%

5,62g Cu => that gives an Al-Cu alloy with 3,85wt% copper

Because the crucible is graphite with high conductivity, heat transfer to the metal is mostly through conduction and radiation. Therefore, the materials have to be put into the crucible with the consideration that it does not wedge together during heating. If the materials wedged together, it wouldn´t glide into the melt at the bottom and may not melt at the top.

The temperature regulator was set to 750°C and heating started at a vacuum of $5,6x10^{-2}$ mbar. A second thermocouple was applied at the top of the crucible (see Fig. 4.3.1.2b). This should give an insight how high the temperature difference between the bottom and the top of the crucible is and if the induction coil heats the graphite crucible stronger as the material inside (for results see Table 5.1.2).

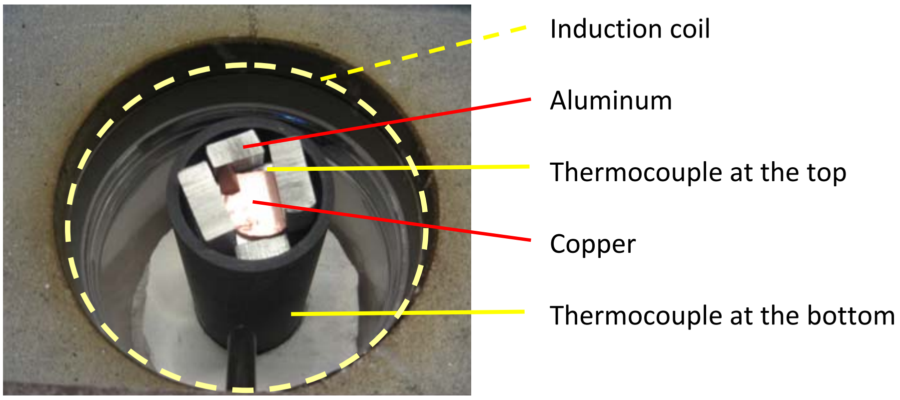

Fig. 4.3.1.2b: Induction furnace with graphite crucible

The thermocouple measured the temperature in the bottom of the crucible. After 750°C was reached, the temperature regulator was set to 800°C and this temperature has been hold for 10min before the power was switched off. The vacuum pump was shut down during cooling at 500°C and the valves of the induction furnace have been kept closed until approximately 400°C. Hence, a very slow cooling rate has been reached.

4.3.1.3 Al-4,3Cu manufactured in a graphite crucible under argon

An Al-Cu alloy with 4,3wt% copper (named sample 3) was manufactured in a graphite crucible under vacuum. Aluminum in the form of small rectangles was used and copper was put on the top of the aluminum, like in the previous manufacturing process. For this experiment, only one thermocouple was used, which was applied in the bottom of the crucible and had no contact to the melt.

Composition of the alloy:	114,84g Al with a purity of 99,99%	
	5,16g Cu	=> that gives an Al-Cu alloy with 4,3wt% copper

The temperature regulator was set to 750°C. After a vacuum of $2{,}4 \times 10^{-1}$ mbar had been generated, the vacuum pump was switched off. The chamber was filled with the inert gas argon. The pressure in the chamber has been hold at 1200 mbar to ensure, that the melt was always surrounded by argon. After 750°C was reached, the temperature regulator was set to 800°C and this temperature has been hold for 10min before the power was switched off. Feeding the chamber with argon was stopped at 500°C and the valves of the induction furnace have been kept closed until approximately 400°C were reached. Hence, a very slow cooling rate was achieved.

This experiment should give an insight if the microscopic structure of the Al-Cu alloy changes when it is manufactured under argon atmosphere instead of vacuum. Sample 3 was therefore compared with sample 5, which was manufactured under vacuum and includes the same amount of copper.

4.3.1.4 Al-4,3Cu manufactured in a graphite crucible under vacuum

In this experiment, an Al-4,3Cu alloy (named sample 5) was manufactured in a graphite crucible under vacuum. Temperature measurement was done in the same way as for sample 3.

Composition of the alloy:	114,84g Al with a purity of 99,99%	
	5,16g Cu	=> that gives an Al-Cu alloy with 4,3wt% copper

The temperature regulator was set to 750°C and heating started at a vacuum of $6,7x10^{-2}$ mbar. After 750°C was reached, the temperature regulator was set to 800°C and this temperature has been hold for 10min before the power was switched off. The vacuum pump was shut down at 500°C and the valves of the induction furnace have been kept closed until approximately 400°C.

4.3.1.5 Al-4,3Cu manufactured in a boron nitride crucible under vacuum

In this procedure, an Al-4,3Cu alloy (named sample 6) was manufactured in a boron nitride crucible and under vacuum. Due to the low thermal conductivity of boron nitride, the process was executed without a temperature regulation. The melt was observed through the inspection glass and the induction coil capacitiy was regulated manually.

Composition of the alloy: 172,26g Al with a purity of 99,99%

7,74g Cu => that gives an Al-Cu alloy with 4,3wt% copper

Heating was started at a vacuum of $6,9x10^{-2}$ mbar. To gain knowledge about the necessary capacity and the time for melting of the elements, different adjustments were tested, see Table 4.3.1.5. In the right column some comments are mentioned.

Table 4.3.1.5: Adjustment of the induction coil during manufacturing of sample 6, Al-4.3Cu

Power set [%]	**Holding time [min]**	**Vacuum at the beginning of holding time [mbar]**	**Comment**
100	17	$6,9x10^{-2}$	Material melt after 14 minutes, Vacuum decreased
80	2	$1x10^{-1}$	Vacuum lower
70	2	$7,1x10^{-2}$	No visible change
60	3	$5,8x10^{-2}$	No visible change
40	1	$5,5x10^{-2}$	Melt cooled down because power was too low
100	2	$5,7x10^{-2}$	Increasing temperature leads to decreasing vacuum

The vacuum pump has been shut down after the induction coil was switched off and before the melt solidified. The valves of the induction furnace have been kept closed until approximately 400°C were reached.

4.3.2 Manufacturing of Al-Cu-Mg alloys

The same induction furnace as for the manufacturing of the Al-Cu alloys was used. Two Al-Cu-Mg alloys were manufactured, one in the graphite crucible and the second one in the boron nitride crucible.

4.3.2.1 Al-4,3Cu-1,49Mg manufactured in a graphite crucible under vacuum

In this experiment, a graphite crucible was used for the manufacturing of an Al-Cu-Mg alloy with 4,3wt% copper and 1,49wt% magnesium (named sample 4). The alloy was manufactured according to the same conditions as sample 5.

Composition of the alloy: 113,05g Al with a purity of 99,99%

5,16g Cu

1,79g Mg with a purity of 99,8%

=> that gives an Al-Cu-Mg alloy with 4,3wt% copper and 1,49wt% magnesium

The temperature regulator was set to 750°C and heating started at a vacuum of 6,8x10^{-2} mbar. After 750°C was reached, the temperature regulator was set to 800°C and this temperature has been hold for 10min before the power was switched off. The vacuum pump was shut down at 500°C and the valves of the induction furnace have been kept closed until approximately 400°C were reached. During this manufacturing route some sublimation of magnesium was noted.

4.3.2.2 Al-4,3Cu-1,49Mg manufactured in a boron nitride crucible under argon

In this procedure, an Al-4,3Cu-1,49Mg alloy (named sample 7) was manufactured in a boron nitride crucible under argon. Due to the low thermal conductivity of boron nitride, the process was executed without a temperature regulation. The melt was observed through the inspection glass and the induction coil capacitiy was regulated manually.

Composition of the alloy: 207,26g Al with a purity of 99,99%

9,46g Cu

3,28g Mg with a purity of 99,8%

=> that gives an Al-Cu-Mg alloy with 4,3wt% copper and 1,49wt% magnesium

After the generation of a vacuum of 1x10^{-1} mbar, the furnace chamber was filled with the inert gas argon. The pressure in the chamber was hold at 1200 mbar to ensure, that the melt was always surrounded by argon. To get knowledge about the necessary power capacity and time for melting the elements, different adjustments were tested, see Table 4.3.2.2.

Table 4.3.2.2: Adjustment of the induction coil during manufacturing of sample 7, Al-4.3Cu-1.49Mg

Power set [%]	Holding time [min]	Pressure [mbar]	Comment
100	14	1200	Material melts after 10 minutes
80	4	1200	No visible change
70	1	1200	Melt cooled down because power was too low
100	4	1200	Melt was heated to ensure a fully dissolution of the alloying elements

During cooling, feeding the chamber with argon was stopped when the melt solidified. The valves of the induction furnace have been kept closed until approximately 400°C.

4.4 Homogenization and extrusion of the manufactured Al-Cu and Al-Cu-Mg alloys

Before extrusion, every sample has been homogenized for 5 hours. The deformation degrees during extrusion were linked to the dimension of the samples in the as-cast condition before extrusion. Every sample was extruded to a diameter of 10,5mm. An overview of the deformation degree is illustrated in Table 4.4.2.

4.4.1 Homogenization

The homogenization temperature was chosen between 0,7 and 0,8 x T_M (T_M....temperature of the first melt) to achieve practical results. T_M was determined with the Al-Cu phase diagram for a copper content of 4,3wt%. The boundary line between the phase α+liquid and α for 4,3% Cu stands for a temperature of about 570°C. This gives a homogenization temperature between:

T_M x 0,7: 0,7x570°C = 399°C and T_M x 0,8: 0,8x570°C = 456°C.

=> The homogenization temperature was chosen at 440°C

The holding time of the homogenization temperature was defined with 5h for every sample. A heating rate from room temperature to the homogenization temperature of around 10K/min and a cooling rate of around 2K/min were chosen.

Furthermore, one specimen of sample 5 (Al-4,3Cu) was homogenized and inspected with the light microscope to inspect the soundness and homogeneity for extrusion.

4.4.2 Extrusion

The homogenized samples were heated before extrusion to make deformation easier. They were put into an oven which was preheated up to 450°C and taken out after 10min. The deformation details are illustrated in Table 4.4.2. After extrusion the samples were cooled down to room temperature.

Table 4.4.2: Sample dimension and deformation degree

	Sample 3	Sample 4	Sample 5	Sample 6	Sample 7
Diameter in the as-cast condition [mm]	34	34	34	39	39
Diameter after extrusion [mm]	10,5	10,5	10,5	10,5	10,5
Deformation degree	3,24	3,24	3,24	3,71	3,71

The sample´s diameter has to be as close to the recipient diameter as much as possible. Smaller diameter means that the sample could be expanded to recipient diameter before it is compressed. Too small diameters might lead to buckling the sample and interference between surface and core by instable flow line. For the samples which were manufactured in the boron nitride crucible with a diameter equal to recipient, a higher deformation degree was achieved.

4.5 Material characterization

To characterize the manufactured materials, light microscope and scanning electron microscope were used. Furthermore hardness tests and differential scanning calorimetry were carried out to analyze the precipitation kinetics.

4.5.1 Analysis method of the manufactured alloys in the as-cast condition

Generally, every manufactured sample was inspected with the light microscope before further tests were done. With the exception of sample 1, every sample was inspected with the scanning electron microscope too. Therewith, the alloy´s composition was determined at the top and bottom of each sample to check the homogeneous distribution of the consisting elements. Furthermore, specimen number 5 has been inspected with light microscope after homogenization at 440°C for 5h and before extrusion.

In the as-cast condition, the hardness of the Al-Cu alloys (sample 3, 5 and 6) was measured. To capture a bigger surface area, a bigger sphere diameter (2,5mm instead of normally used 1mm) was chosen. The hardness was measured in the middle of the sample as well as at the edge of each sample. For every specimen the average value of 8 measurements was calculated to get more exact and representative results.

4.5.2 Analysis method of the manufactured alloys after homogenization and extrusion

The homogenized and extruded samples are sample 3 to7. Light and scanning electron microscopy were used for investigating every sample. Hardness tests were carried out for sample 5, 6 and 7.

The Al-4,3Cu alloys (sample 5 and 6) were solution heat treated at 550°C for 25min, quenched in water to room temperature and naturally aged. Hardness measurements were carried out at different time steps after quenching, see Fig. 4.5.2a. Every time, the average value of 5 hardness measurements was calculated to get more exact results.

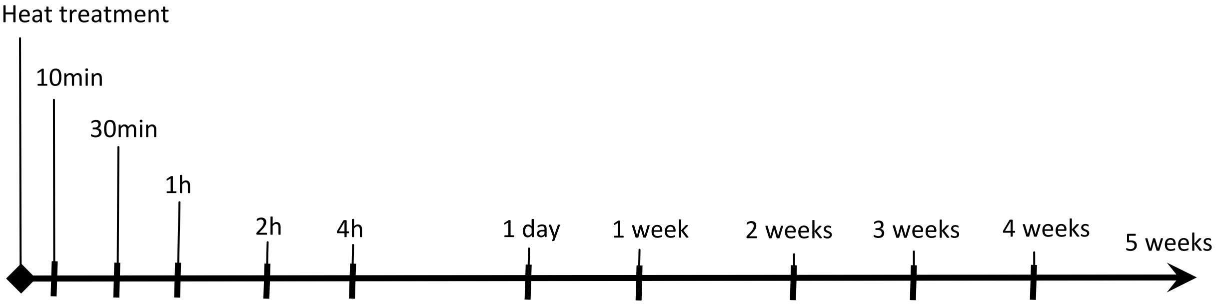

Fig. 4.5.2a: Plan of hardness measurements for the manufactured Al-Cu alloys

The Al-4,3Cu-1,49Mg alloy (sample7) was solution heat treated at 495°C for 30min, quenched in water to room temperature and naturally aged. Hardness measurements were carried out at different time steps after quenching, see Fig. 4.5.2b. At every time step, the average value of 5 measurements was calculated to get more exact results.

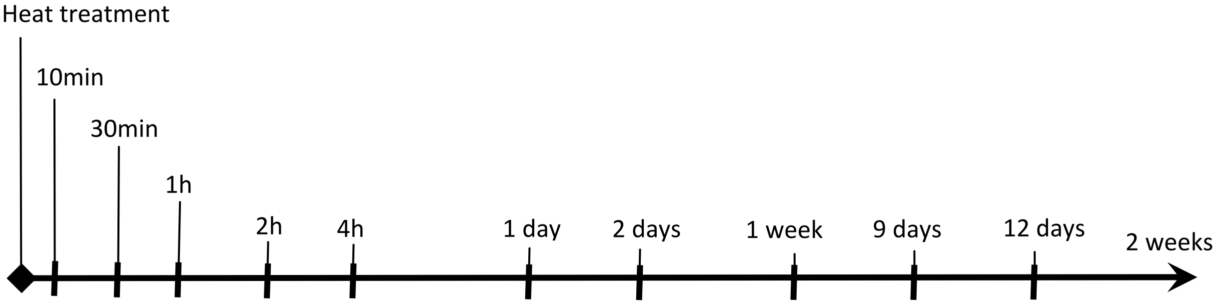

Fig. 4.5.2a: Plan of hardness measurements for the manufactured Al-Cu-Mg alloys

Differential scanning calorimetry was applied for sample 5 and 7. To gain knowledge about which heating rate is the best for sample 5, 3 different heating rates (5, 10 and 20K/min) were analyzed (see Fig. 4.2.7b). For every heating rate the second run was carried out with a heating rate of 5K/min to check the soundness of first cycle. According to the literature [13, 14], a heating rate of 10K/min was chosen for sample 7.

The DSC specimens of sample 5 were solution heat treated at 550°C for 25 minutes and quenched in water to room temperature. Afterwards they were naturally aged for 30 minutes and 2 weeks.

The DSC specimens of sample 7 were solution heat treated at 495°C for 30 minutes and quenched in water to room temperature. Afterwards they were naturally aged for 30 minutes, 2 days and 2 weeks.

4.5.3 Analysis method of an industrial 2024 aluminum alloy

Formerly the rolled alloy was covered with two pure aluminum layers (see Fig. 4.5.3a). Light and scanning electron microscopy was used for the analysis of the alloy´s microstructure.

In the experiment, a specimen was solution heat treated at 550°C for 25min and quenched in water. Two mapping analyses with a resolution of 256x200 and a magnification rate of 1000x were applied to illustrate the alloy´s element distribution in the solution heat treated and in the original condition.

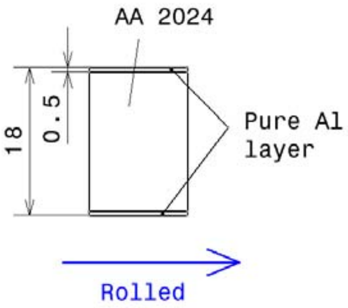

Fig. 4.5.3a: Specimen dimension of the 2024 aluminum alloy

Two specimens were solution heat treated for 25min at a temperature of 550°C and 495°C. Subsequently they were quenched in water to room temperature. Hardness measurements were carried out at different times after quenching (Fig. 4.5.3b). Every time, the average value of 5 measurements was calculated in order to get more exact results.

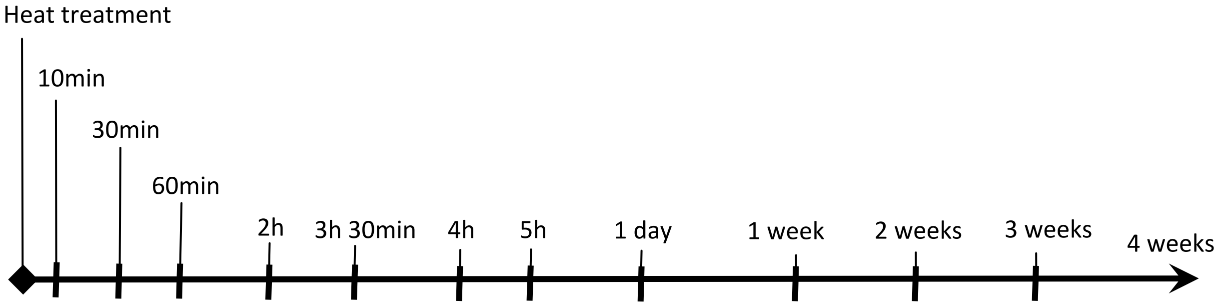

Fig. 4.5.3b: Plan of hardness measurements for the 2024 aluminum alloy

The DSC specimens were solution heat treated at 550°C for 25min, quenched in water and room temperature aged for 30min. To gain knowledge about which heating rate is the best for the alloy, 3 different heating rates (5, 10 and 20K/min) were analyzed (see Fig. 4.2.7b). The second run was carried out just for validation of the first run. After two weeks room temperature aging, another DSC curve was recorded with the former defined best heating rate.

To gain knowledge about the influence of the solution heat treatment temperature and to be able to compare the results better with literature, further DSC curves were recorded. For this measurement, the specimens were solution heat treated at 495°C for 25min, quenched in water and room temperature aged for 30min and 2 weeks. The specimens were heated according to Fig. 4.2.7b with a heating rate of 10K/min.

5 Results

5.1 Characteristics of Al-Cu alloys in the as-cast condition

5.1.1 Al-3,85Cu manufactured in a silicon oxide crucible under vacuum

For sample 1, only light microscope inspection was applied to see if the copper is equally distributed in the aluminum matrix. The results are shown in Fig. 5.1.1.1.

5.1.1.1 Light microscope analysis

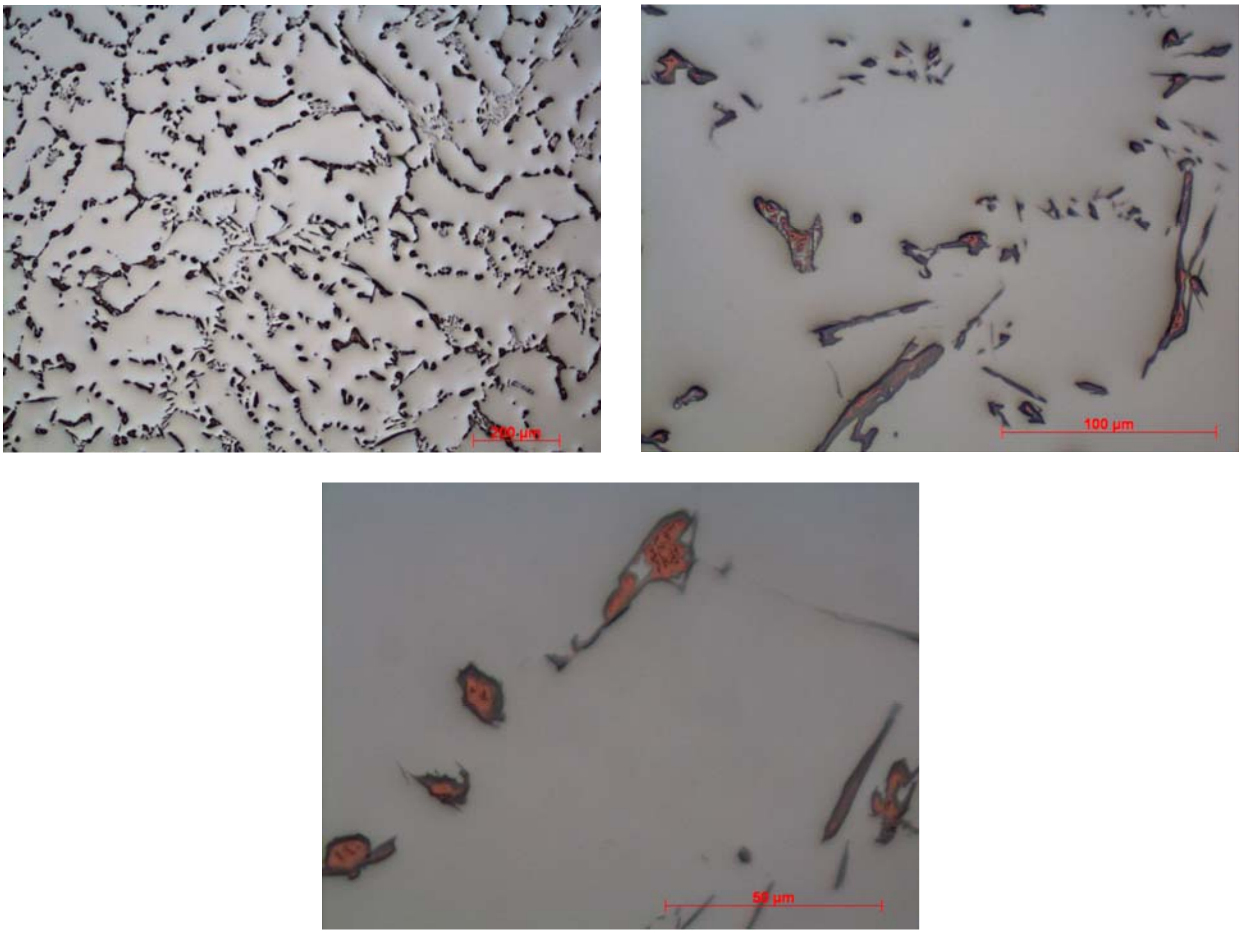

Fig. 5.1.1.1: Light microscope view of sample 1 (Al-3,85Cu) with different magnifications

5.1.2 Al-3,85Cu manufactured in a graphite crucible under vacuum

Sample 2 was investigated by light microscope and scanning electron microscope analyses in the as-cast condition. The results obtained from temperature measurement with the thermocouples at the top (insert in the crucible) and at the bottom of the graphite crucible (contacted to the crucible wall) are shown in Table 5.1.2.

Table 5.1.2: Temperature difference between the top and the bottom of the graphite crucible during heating

Temperature at the bottom	190°C	300°C	650°C	670°C	760°C
Temperature at the top	45°C	82°C	285°C	380°C	540°C

The results show that the temperature measured by the thermocouple at the bottom of the crucible is always higher and more reliable for control of the furnace temperature than at the top. During heating, the material was observed through the inspection glass. At 650°C, aluminum began to melt at the bottom and after reaching 690°C the solid aluminum bars glided into the melt.

Al and Cu have different densities and to investigate the influence of gravity on the copper distribution in the cast is important for producing a homogeneous alloy. Sample 2 was cut 9mm below the top, through the middle and 6mm above the bottom. A longitudinal cross section specimen was also provided to get more exact information about the Cu distribution at the top (see Fig. 5.1.2). The first impression was that at the top, the sample surface was more contaminated than at the bottom.

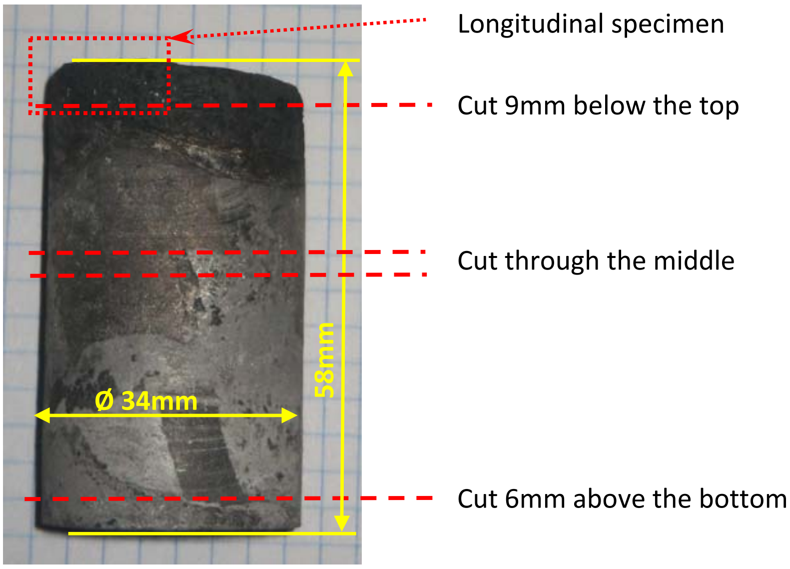

Fig. 5.1.2: Locations for microscopic analysis of sample 2, Al-3,85Cu

5.1.2.1 Light microscope analysis

In order to see if the copper is homogeneously distributed in the aluminum matrix the specimens were inspected in unetched condition as well at the edge as in the middle. Besides, every specimen was scanned with light microscope to find porosities. For every part of sample 2, the locations of the view positions are shown in Fig. 5.1.2.1.

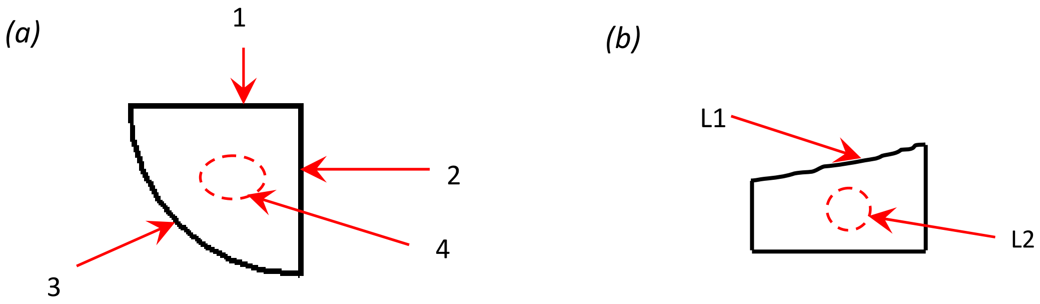

Fig. 5.1.2.1: Locations of the view positions *(a)* at the bottom, middle and top; *(b)* at the longitudinal specimen

Results for the “bottom-specimen”:

As it can be observed in Fig. 5.1.2.1a – f, the copper (reddish) distribution in the aluminum matrix (white) is consistent as well at the edge as in the middle of the specimen. In chapter 5.1.2.2 this was also proved with the scanning electron microscope. Porosities appear at every part of the specimen but there are also many areas without them. Fig. 5.1.2.1f shows clearly the interdendritic pores at a higher magnification in position 4.

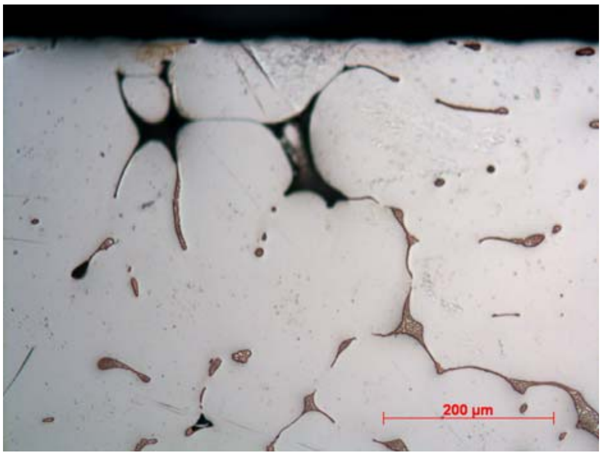

Fig. 5.1.2.1a: As-cast microscopic view at position 1

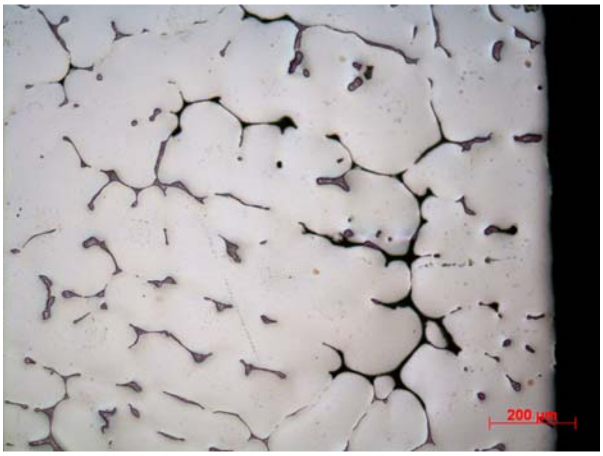

Fig. 5.1.2.1b: Microscopic view at position 2, porosity present in interdendritic spaces

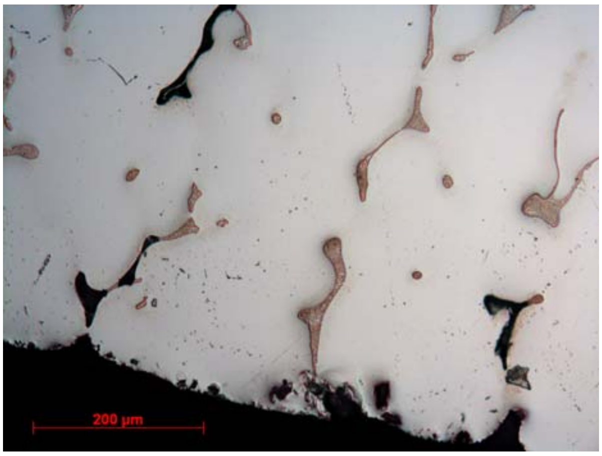

Fig. 5.1.2.1c: Microscopic view at position 3

Fig. 5.1.2.1d: Microscopic view at position 3

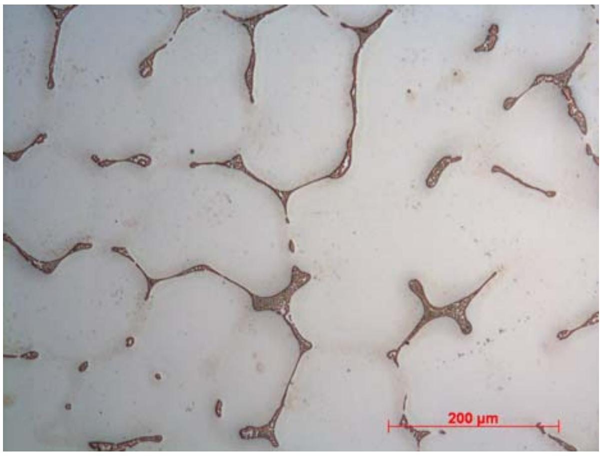

Fig. 5.1.2.1e: Microscopic view at position 4

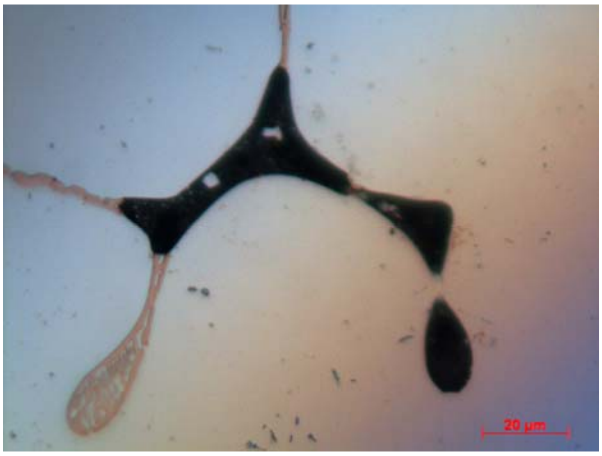

Fig. 5.1.2.1f: Microscopic view at position 4

Results for the "middle-specimen":

As it can be observed in Fig. 5.1.2.1g – j, porosities appear at every position of the specimen.

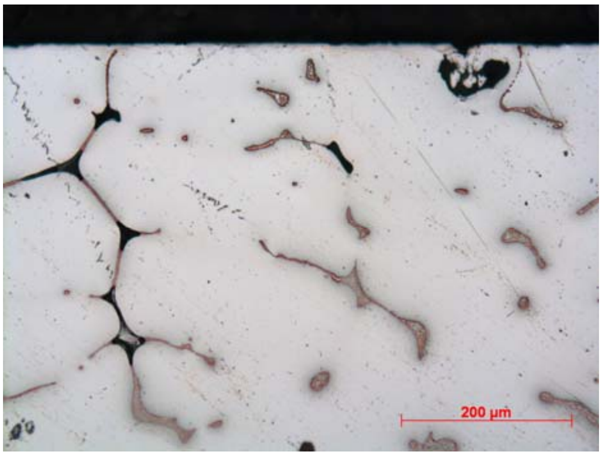

Fig. 5.1.2.1g: Microscopic view at position 1

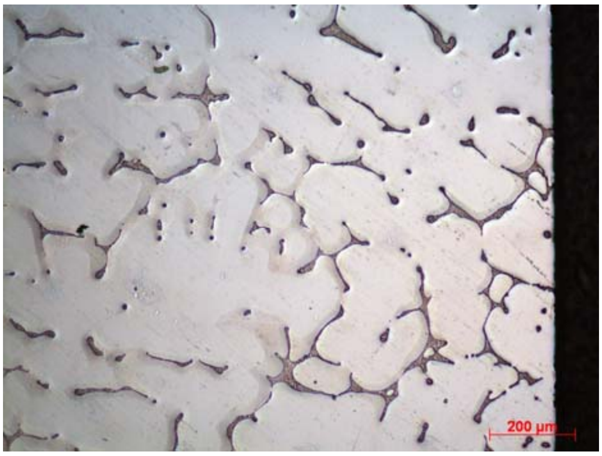

Fig. 5.1.2.1h: Microscopic view at position 2

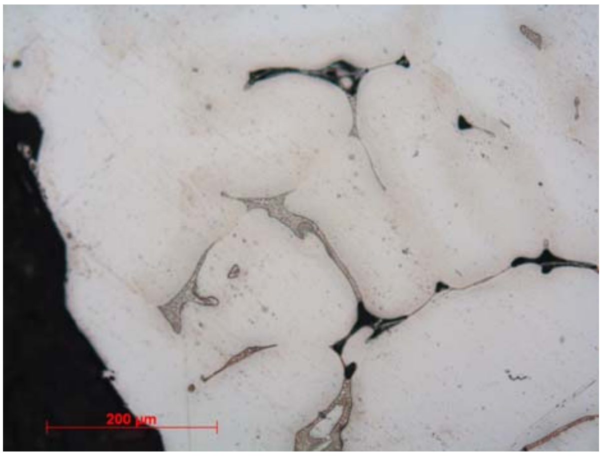

Fig. 5.1.2.1i: Microscopic view at position 3

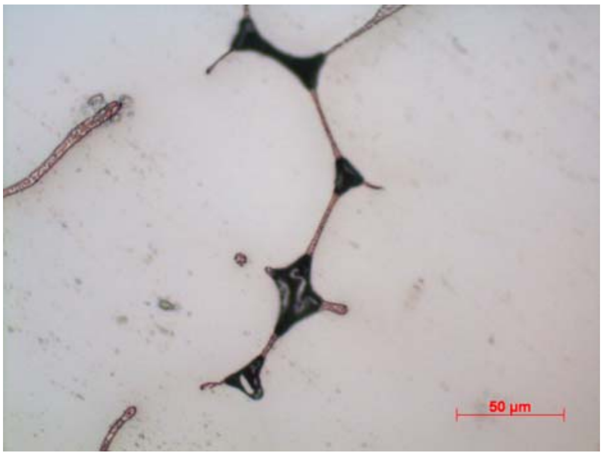

Fig. 5.1.2.1j: Microscopic view at position 4

Results for the "top-specimen":

At the top of sample 2, the same results were obtained as at the bottom and in the middle (see Fig. 5.1.2.1k – l).

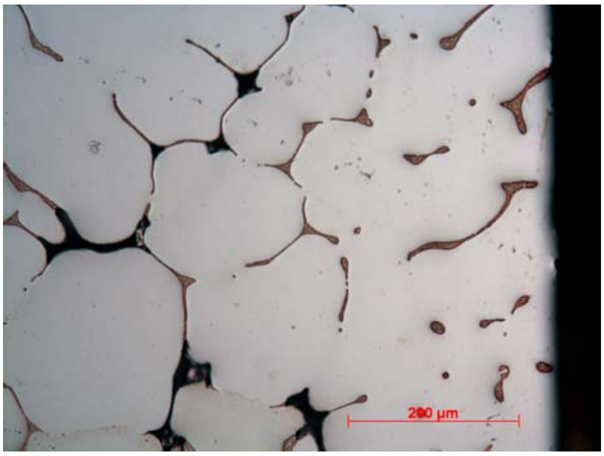

Fig. 5.1.2.1k: Microscopic view at position 2

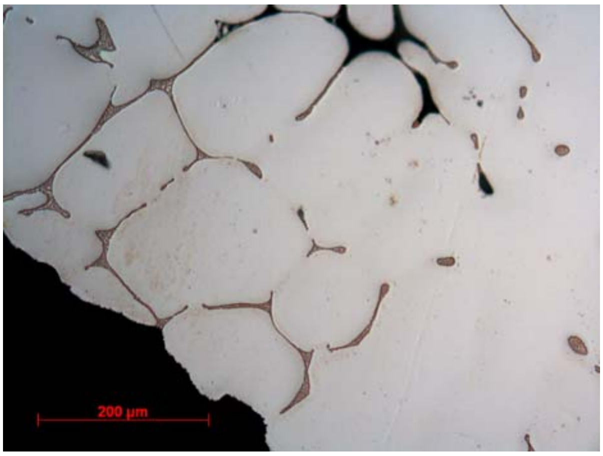

Fig. 5.1.2.1l: Microscopic view at position

Results for the "longitudinal-specimen":

For the longitudinal specimen of sample 2, again, the same results were obtained as at the bottom, in the middle and at the top (see Fig. 5.1.2.1m-n). The copper distribution satisfies the expectations.

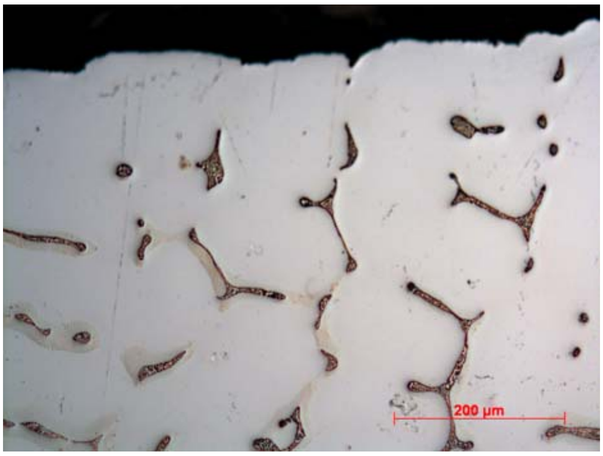

Fig. 5.1.2.1m: Microscopic view at position L1

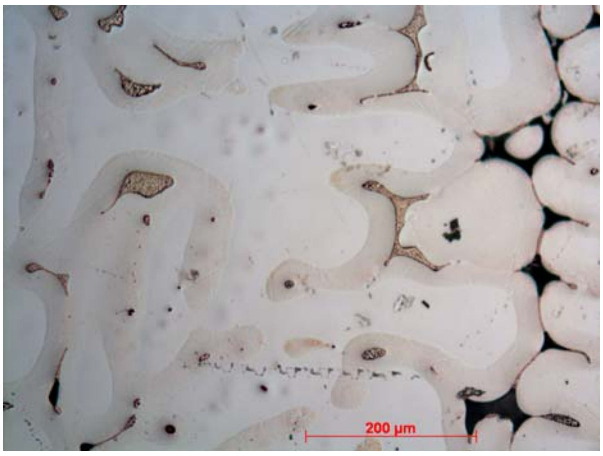

Fig. 5.1.2.1n: Microscopic view at position L2

5.1.2.2 Scanning electron microscope analysis

According to the Al-Cu phase diagram, slow cooling rates lead to α + θ -phase. The composition of the reddish copper regions, which are represented in chapter 5.1.2.1, was determined at higher magnification rates to see the morphology in more detail and to measure local and average chemical composition. Fig. 5.1.2.2 shows copper regions at different magnification.

For Fig. 5.1.2.2 *(d)*, the composition was determined at a magnification rate of 5000x. The composition of the alloy measured by EDX in *(d)* contains 67,07 wt% Al and 32,93 wt% Cu. This region indicates typical eutectic structure at grain boundaries consisting of intermetallic phase θ ($CuAl_2$) and Al.

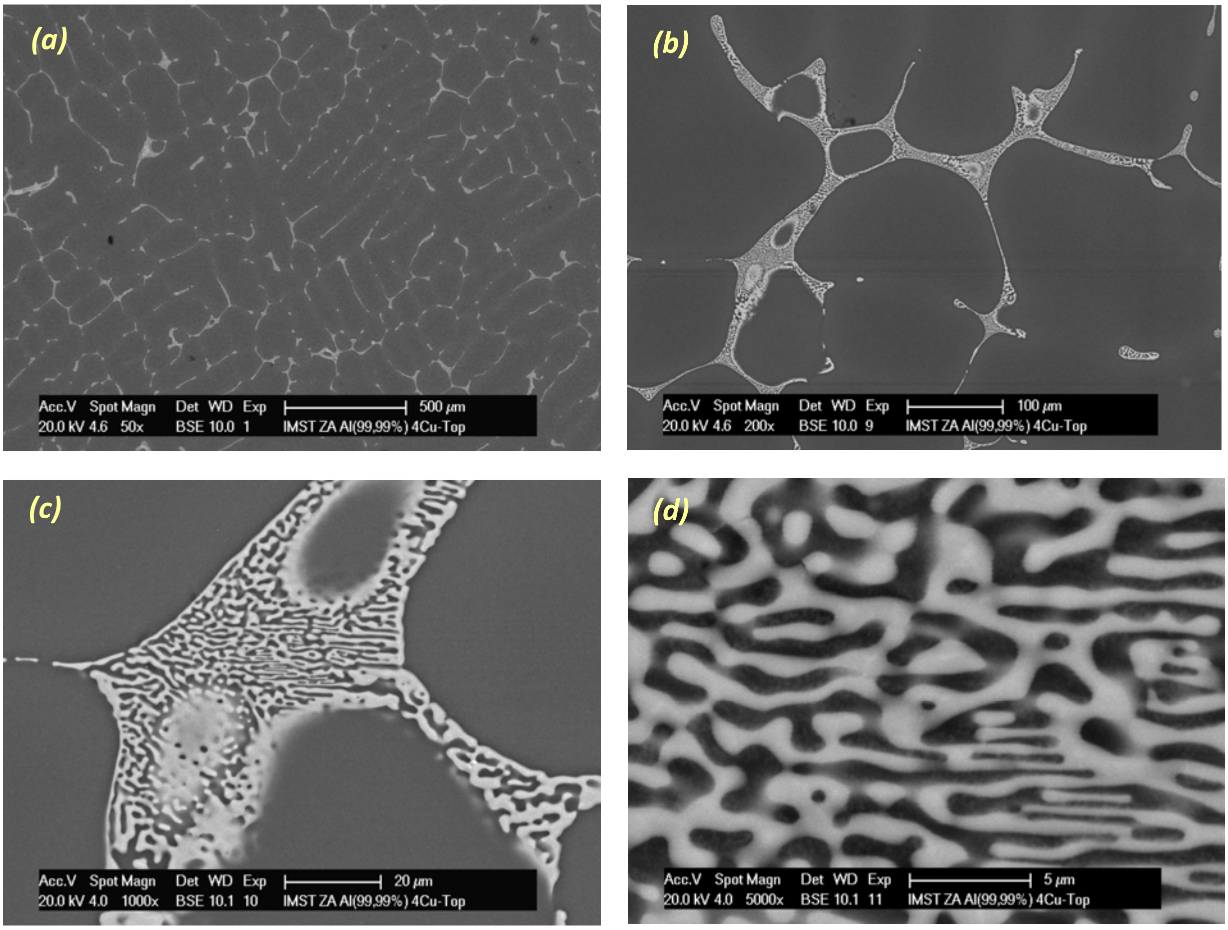

Fig. 5.1.2.2: Scanning electron microscope view of sample 2 at the top with different magnifications

In the backscattered electron (BSE) images above heavier elements look like brighter in image. The intermetallic phases which are heavier differ from the Al matrix and are therefore easily recognizable. In (a), the grain boundaries are decorated with intermetallic phases. Grain size is estimated to be between 100µm and 200µm. In (b, c and d) the eutectic structure and porosities are present in interdendritic spaces which are visible at higher magnifications.

The ratio of aluminum and copper at the bottom, middle and top of the sample was determined. The aim of this analysis was to get more information about the copper distribution in the aluminum matrix. At every part (bottom, middle and top) of the specimen, four measurements were made to get more representative results. Furthermore, at the longitudinal test specimen, also four measurements were made (see Fig. 5.1.2.2a). All measurements were carried out at a magnification of 50x. Table 5.1.2.2a-d represents the results of the Al and Cu content of the alloy at every measurement point. In Table 5.1.2.2a–d, the average value of the alloy´s composition was calculated for every specimen.

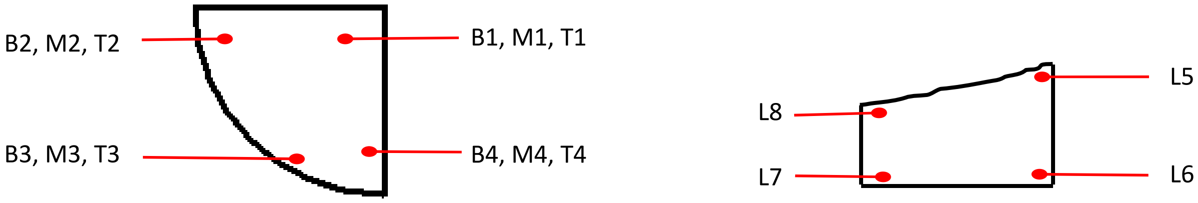

Fig. 5.1.2.2a: Locations of the measurement positions

Table 5.1.2.2a: Results for the alloy´s element distribution at the bottom of sample 2

Element	Alloy composition in wt% at different positions				Average
	Measurement B1	Measurement B2	Measurement B3	Measurement B4	
Al	95,21	94,90	95,31	95,64	95,265
Cu	4,79	5,10	4,69	4,36	4,735

Table 5.1.2.2b: Results for the alloy´s element distribution in the middle of sample 2

Element	Alloy composition in wt% at different positions				Average
	Measurement M1	Measurement M2	Measurement M3	Measurement M4	
Al	94,66	95,16	95,95	94,48	95,0625
Cu	5,34	4,84	4,05	5,52	4,9375

Table 5.1.2.2c: Results for the alloy´s element distribution at the top of sample 2

Element	Alloy composition in wt% at different positions				Average
	Measurement T1	Measurement T2	Measurement T3	Measurement T4	
Al	95,67	95,37	95,93	94,79	95,44
Cu	4,33	4,63	4,07	5,21	4,56

Table 5.1.2.2d: Results for the alloy´s element distribution at the longitudinal specimen of sample 2

Element	Alloy composition in wt% at different positions				Average
	Measurement L5	Measurement L6	Measurement L7	Measurement L8	
Al	94,77	94,86	95,28	94,83	94,935
Cu	5,23	5,14	4,72	5,17	5,065

Finally, the deviation of the average values from the reference input was determined at the bottom, middle, top and for the longitudinal specimen. Summary of the results is presented in Table 5.1.2.2.

Table 5.1.2.2: Sample 2: Deviation of the alloy´s composition from the reference input of 3,85 wt% Cu

Element	Average alloy composition in wt% at different positions				Overall average alloy composition in wt%
	Bottom	Middle	Top	Longitudinal	
Al	95,265	95,0625	95,44	94,935	95,1756
Cu	4,735	4,9375	4,56	5,065	4,8244
Element	Deviation from the reference input of 3,85 wt% Cu in [%]				
	Bottom	Middle	Top	Longitudinal	Overall
Cu	+22,99	+28,25	+18,44	+31,56	+25,31

The alloy´s composition in wt% at all measurement positions is higher than the reference input of 3,85% Cu. Gravity had no influence on the copper content between top and bottom of sample 2 because the deviation of the reference input at the bottom is 22,99%, at the top 18,44% and in the longitudinal specimen 31,56%. The overall average deviation value is 25,31% Cu.

Measurement uncertainty is present but the values are for every specimen higher than the reference input and do not vary strongly. The scanning electron microscope analysis is therefore exact enough to prove a homogeneous copper distribution in the alloy.

5.1.3 Al-4,3Cu manufactured in a graphite crucible under argon

Sample 3 was manufactured under argon to see the effect of different furnace atmospheres in production of samples. Two specimens, one at the bottom and one at the top were inspected with light microscope and scanning electron microscope.

The sample was cut 8mm below the top and 5mm above the bottom (see Fig. 5.1.3). The same as before the sample top surface seems to be more contaminated than the bottom.

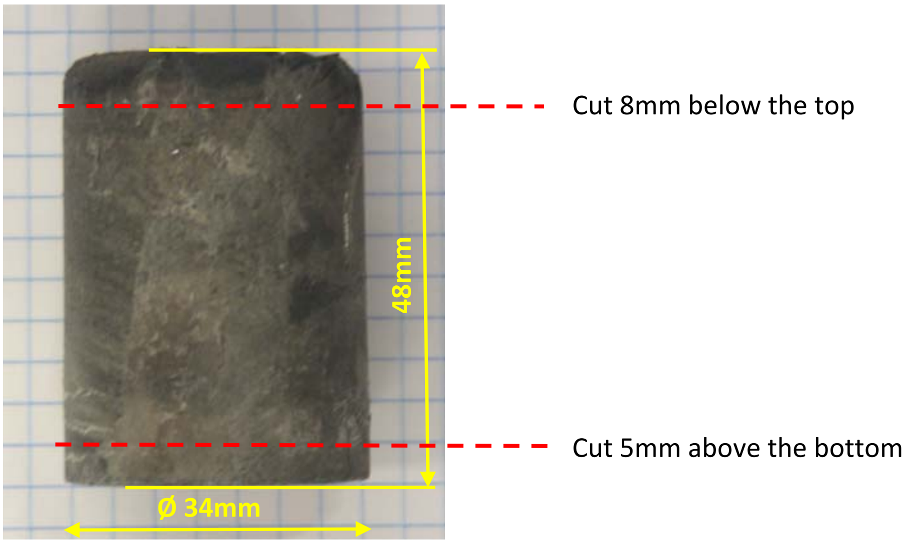

Fig. 5.1.3: Sample 3, Al-4.3Cu manufactured under argon gas

5.1.3.1 Light microscope analysis

The specimens were inspected at defined positions (see Fig. 5.1.3.1) to see the microstructure, to find porosities and to compare them with sample 5.

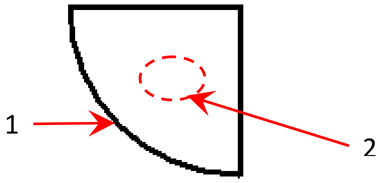

Fig. 5.1.3.1: Locations of the view positions at the top and bottom of sample 3

Results for the "bottom-specimen":

Fig. 5.1.3.1a: Microscopic view at position 1

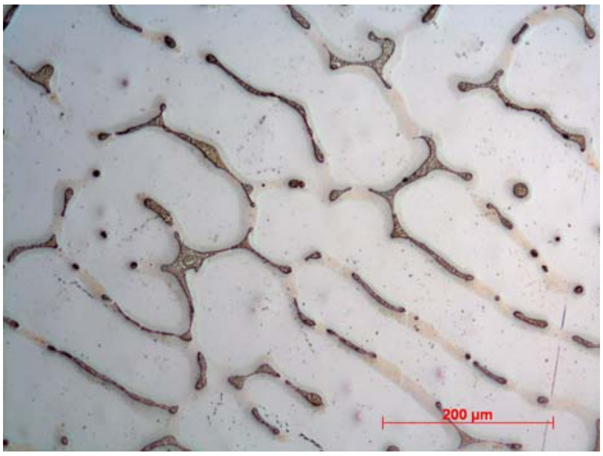

Fig. 5.1.3.1b: Microscopic view at position 2

Results for the “top-specimen”:

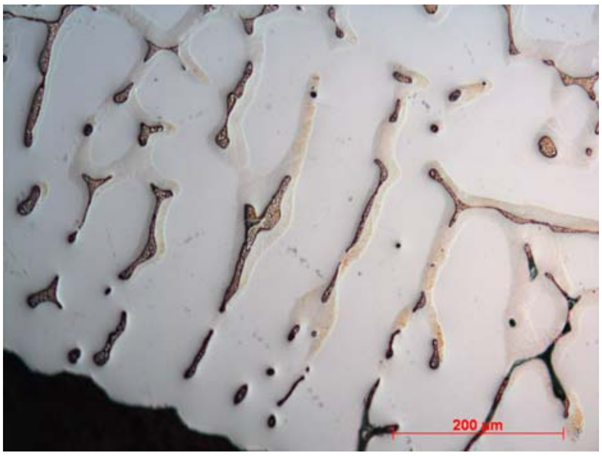

Fig. 5.1.3.1c: Microscopic view at position 1

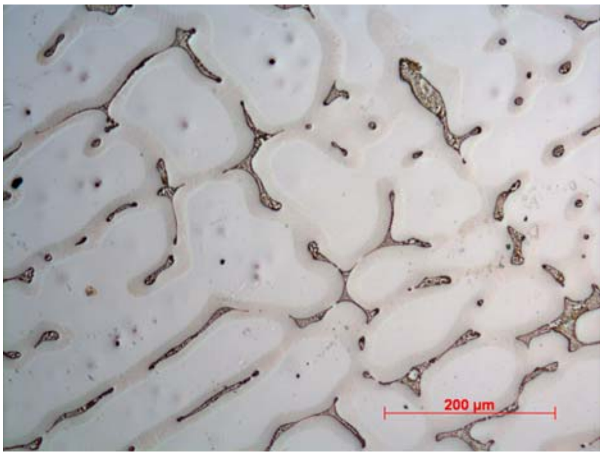

Fig. 5.1.3.1d: Microscopic view at position 2

As it can be seen in Fig. 5.1.3.1c-d, almost the same microstructure as for the bottom of the specimen was obtained. No big pore was noticed in the micrographs.

5.1.3.2 Scanning electron microscope analysis

The ratio of aluminum and copper at the bottom and the top of the sample was determined. The same procedure as stated in chapter 5.1.2.2 was carried out.

Summary of the results is presented in Table 5.1.3.2.

Table 5.1.3.2: Sample 3: Deviation of the alloy´s composition from the reference input of 4,3 wt% Cu

Element	**Average alloy composition in wt% at different positions**		**Overall average alloy composition in wt%**
	Bottom	Top	
Al	94,733	94,763	94,748
Cu	5,267	5,237	5,252
Element	**Deviation from the reference input of 4,3 wt% Cu in [%]**		
	Bottom	Top	**Overall**
Cu	+22,49	+21,79	+22,14

The alloy´s composition in wt% at all measurement positions is higher than the reference input of 4,3% Cu. The deviation values of +22,49% at the bottom and + 21,79% at the top are nearly equal. Measurement uncertainty is present but the values are for every specimen higher than the reference input and do not vary strongly. The scanning electron microscope analysis is therefore exact enough to prove that a homogeneous copper distribution exists in the alloy.

5.1.4 Al-4,3Cu manufactured in a graphite crucible under vacuum

Sample 5 was manufactured under vacuum and has been compared with sample 3 in previous section which has been manufactured under argon atmosphere. Moreover, one piece of the specimen has been homogenized at 440°C for 5 hours and was compared with the specimen before homogenization with light microscopy.

The specimens were inspected for soundness and metallography pictures were prepared at the same positions as in sample 3.

5.1.4.1 Light microscope analysis

The specimens were inspected at the same positions as at sample 3. Besides, every specimen was scanned in order to find porosities. The locations of the view positions are shown Fig. 5.1.4.1.

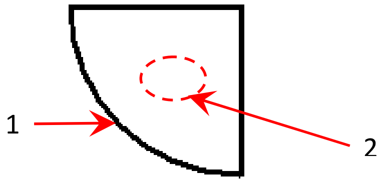

Fig. 5.1.4.1: Locations of the view positions at the top and bottom of sample 5

<u>Results for the “bottom-specimen”:</u>

The left column shows the microscopic structure in the as-cast and the right one in the homogenized condition.

As-cast

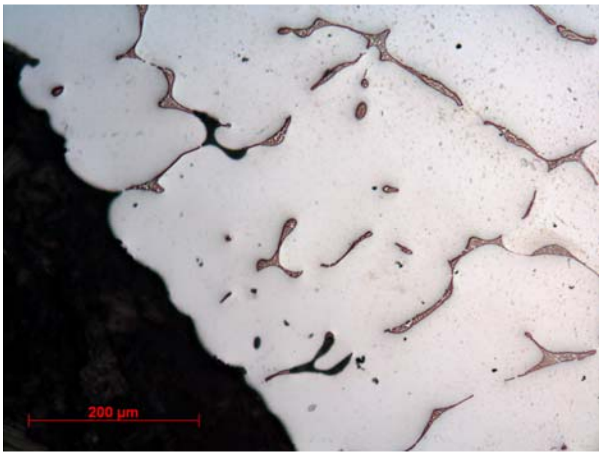

Fig. 5.1.4.1a: Position 1, as-cast condition

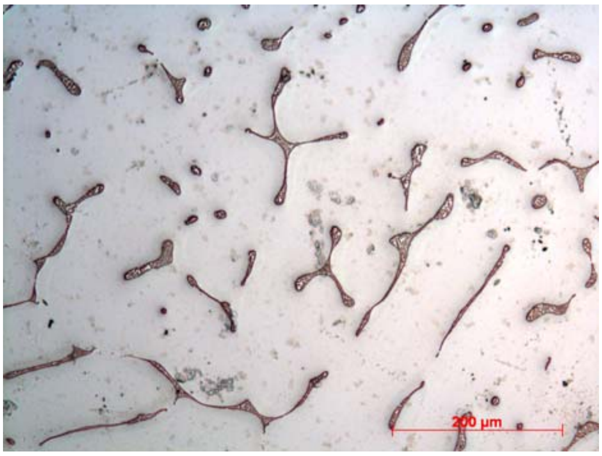

Fig. 5.1.4.1b: Position 2, as-cast condition

Homogenized

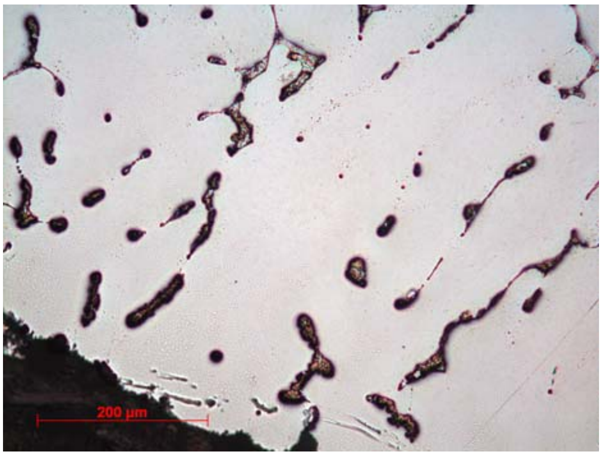

Fig. 5.1.4.1c: Position 1, homogenized

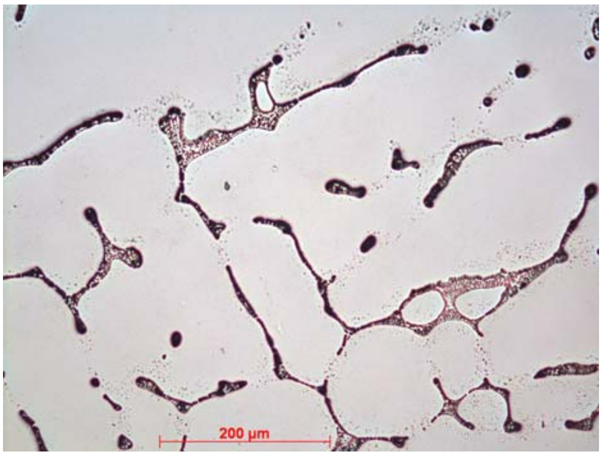

Fig. 5.1.4.1d: Position 2, homogenized

The effect of homogenization is not so much pronounced because the segregation effect is not big in small samples. But anyhow, the homogenized specimen has more round particles than the as-cast one. The microscopic structures of sample 3 in Fig. 5.1.3.1a–b and of sample 5 in Fig. 5.1.4.1a-b were compared with each other. Most significant are the smaller interdendritic spaces in sample 3. It could be due to the higher cooling rate from the melt to solid state in comparison to sample 5 due to the convection effect of argon gas.

5.1.4.2 Scanning electron microscope analysis

Fig. 5.1.4.2 shows the BSE microscopy images of the structure of sample 5 in the as-cast condition at two different magnifications. In *(a)* some porosities are visible which appear as black spots. In (b) with higher magnification, some eutectic structure at grain boundaries consisting of intermetallic phase θ ($CuAl_2$) and Al is visible.

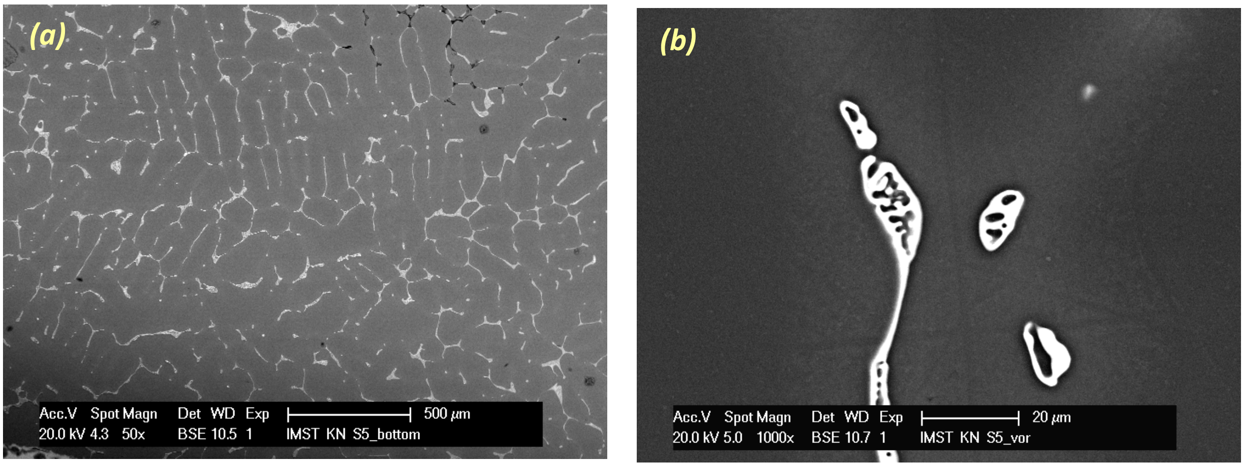

Fig. 5.1.4.2: Backscatter electron microscopy images of sample 5 at two different magnifications

The chemical composition of the alloy, ratio of aluminum and copper at the bottom and top of the specimen was determined by EDX. The procedure is the same as explained before. Summary of the results is given in Table 5.1.4.2.

Table 5.1.4.2: Sample 5: Deviation of the alloy´s composition from the reference input of 4,3 wt% Cu

Element	**Average alloy composition in wt% at different positions**		**Overall average alloy composition in wt%**
	Bottom	Top	
Al	95,083	94,977	95,03
Cu	4,917	5,023	4,97
Element	**Deviation from the reference input of 4,3 wt% Cu in [%]**		
	Bottom	Top	**Overall**
Cu	+14,35	+16,81	+15,58

The alloy´s composition in wt% at all measurement positions is higher than the reference input of 4,3% Cu. The deviation values of +14,35% at the bottom and + 16,81% at the top are nearly equal.

Element-mapping of sample 5 was carried out before and after homogenization. The specimens were taken from the bottom of the sample. A magnification of 200x was chosen for mapping.

As-cast

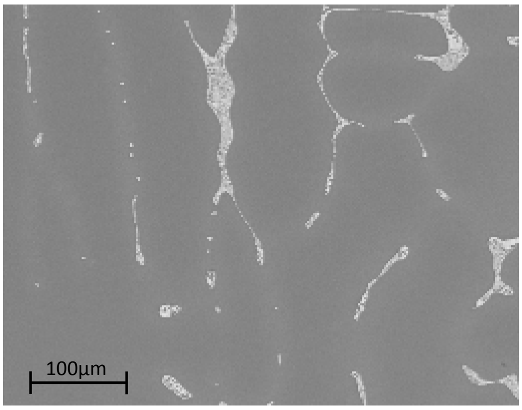

Fig. 5.1.4.2a: Microscopic structure

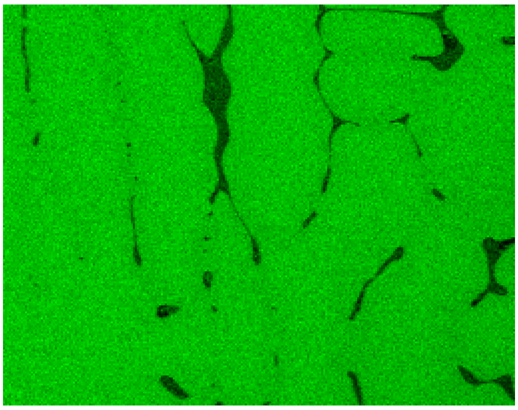

Fig. 5.1.4.2b: Aluminum distribution

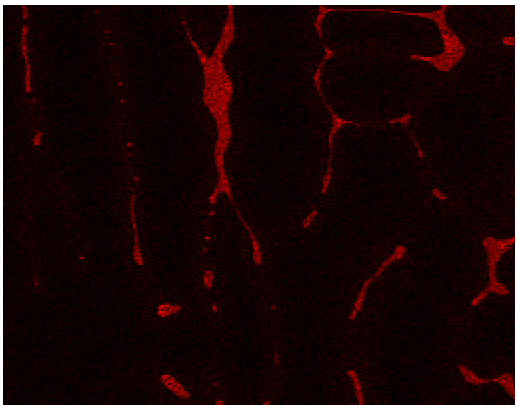

Fig. 5.1.4.2c: Copper distribution

Homogenized

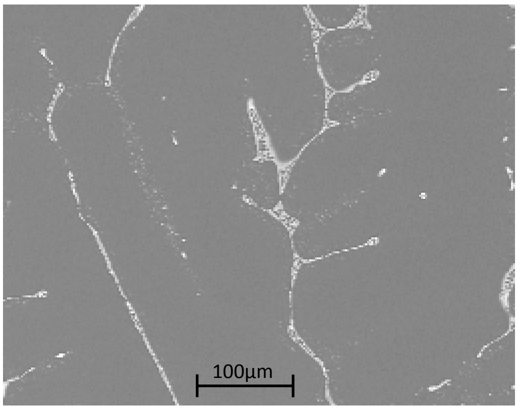

Fig. 5.1.4.2d: Microscopic structure

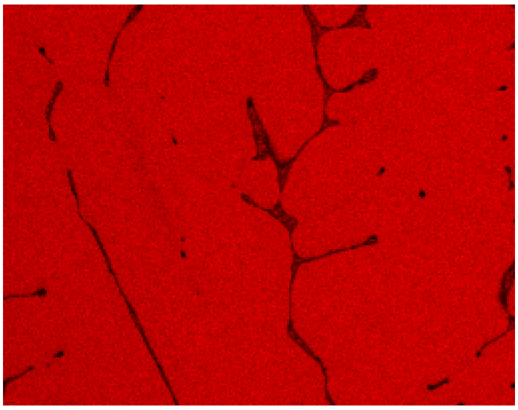

Fig. 5.1.4.2e: Aluminum distribution

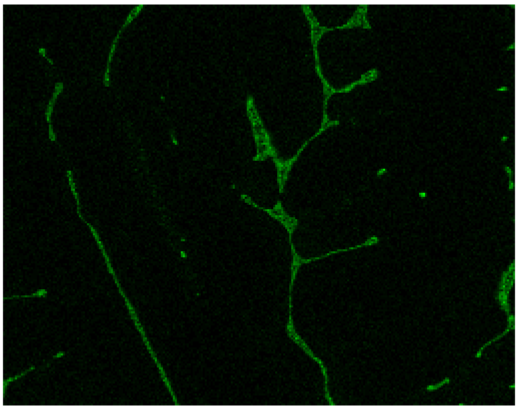

Fig. 5.1.4.2f: Copper distribution

Fig. 5.1.4.2a-f shows the copper distribution in the aluminum matrix. The images confirm that the „reddish“ structure, which was observed with the light microscope, contains copper.

5.1.5 Al-4,3Cu manufactured in a boron nitride crucible under vacuum

Sample 6 was manufactured under vacuum and compared with sample 5 to see if there is a difference in the microscopic structure when a boron nitride crucible is used instead of the graphite one. Two specimens were taken from the top and bottom of the sample. Light and electron microscopy were used to investigate the microstructure and compare it with sample 5.

Dimension of sample 6 with the boron nitride crucible is a cylinder with 39mm diameter and 56mm height.

5.1.5.1 Light microscope analysis

The specimens were inspected at the same positions as sample 5, see Fig. 5.1.4.1 in chapter 5.1.4.1. Besides, every specimen was scanned to find porosities.

Results for the "bottom-specimen":

Two pictures, one at the border and one in the middle of the bottom specimen, are shown in Fig. 5.1.5.1a and b. They were compared with the microscopic structure of sample 5.

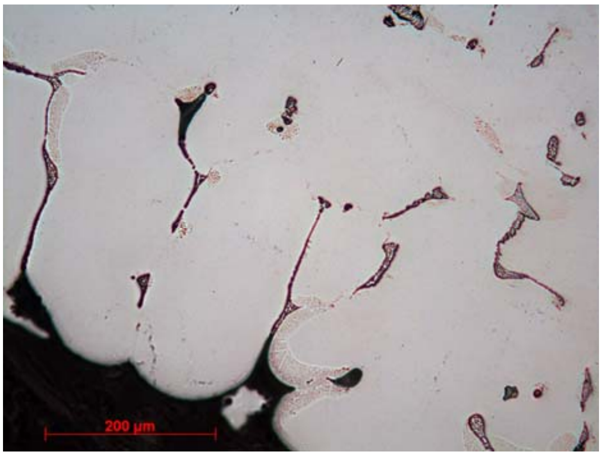

Fig. 5.1.5.1a: Microscopic view at the border

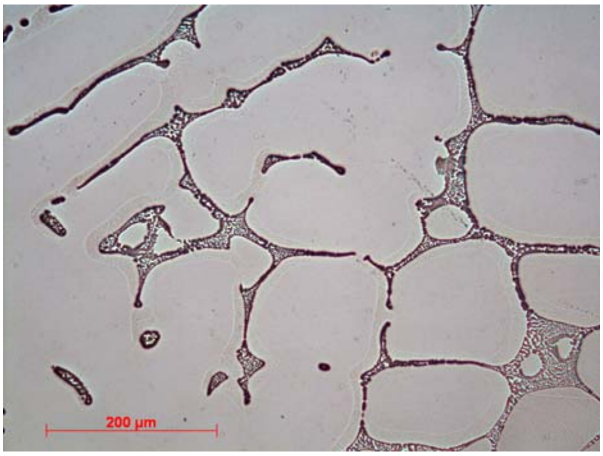

Fig. 5.1.5.1b: Microscopic view in the middle

Results for the "top-specimen":

For the top specimen two pictures are shown in Fig. 5.1.5.1c and d.

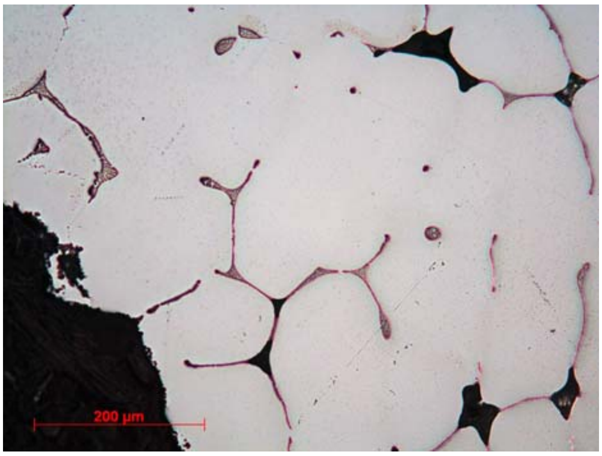

Fig. 5.1.5.1c: Microscopic view at the border

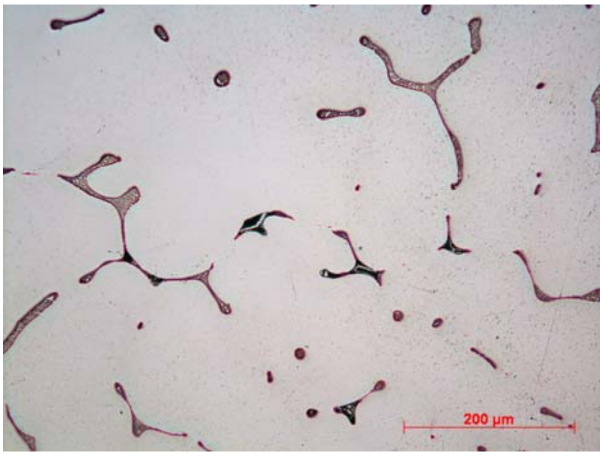

Fig. 5.1.5.1d: Microscopic view in the middle

Results of light microscopy confirm that the boron nitride crucible has no influence on the microstructure of the as-cast sample in compare to samples of the graphite crucible. Samples manufactured in the graphite crucible have almost the same microstructure as observed by the boron nitride crucible. Porosities are also visible and the amount of them is almost the same as in sample 5.

5.1.5.2 Scanning electron microscope analysis

The chemical composition of the alloy at the bottom and top of the specimen was determined by EDX. The procedure of evaluation is the same as explained before. Summary of the results is given in Table 5.1.5.2.

Table 5.1.5.2: Sample 6: Deviation of the alloy´s composition from the reference input of 4,3 wt% Cu

Element	**Average alloy composition in wt% at different positions**		**Overall average alloy composition in wt%**
	Bottom	Top	
Al	94,723	94,843	94,783
Cu	5,277	5,157	5,217
Element	**Deviation from the reference input of 4,3 wt% Cu in [%]**		
	Bottom	Top	**Overall**
Cu	+22,72	+19,93	+21,33

The results confirm that the copper distribution is uniformly. All measurements show a higher copper content than the reference input of 4,3wt%. The deviation values of +22,72% at the bottom and + 19,93% at the top are nearly equal.

As a result, manufacturing with both crucibles, the graphite and the boron nitride one, results in alloys with homogeneous element distribution.

5.1.6 Hardness measurement

The manufacturing procedure can have an effect on the alloy´s hardness. The manufacturing characteristics of the three samples with the same copper content and the hardness values in as-cast condition are given In Table 5.1.6 and Table 9.1.1.

Table 5.1.6: HBW 2,5/15,625 values in the as-cast condition of sample 3, 5 and 6

Designation	Composition [wt%]	Used crucible	Furnace atmosphere	Hardness
Sample 3	Al-4,3Cu	Graphite	Argon	44,7
Sample 5	Al-4,3Cu	Graphite	Vacuum	41,8
Sample 6	Al-4,3Cu	Boron nitride	Vacuum	45,7

5.2 Characteristics of Al-Cu alloys after homogenization and extrusion

In this chapter, the characteristics of sample 5 and 6 after homogenization and extrusion are combined. The microstructures were investigated by light microscopy and scanning electron microscopy. Furthermore, hardness measurements and differential scanning calorimetry were applied to study the precipitation kinetics.

5.2.1 Light microscope analysis

Sample 3, 5 and 6 show the same microstructure in the as-cast condition. Hence, after homogenization and extrusion only the microstructure images of sample 5 and 6, which have different deformation degree after extrusion, are presented. The specimens were inspected at the positions which are shown in Fig. 5.2.1.

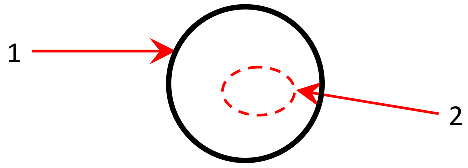

Fig. 5.2.1: Locations of the view positions of sample 5 and 6 after homogenization and extrusion

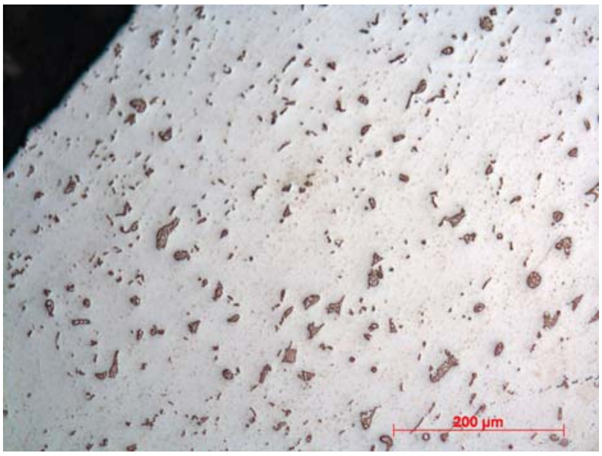

Fig. 5.2.1a: Sample 5, position 1

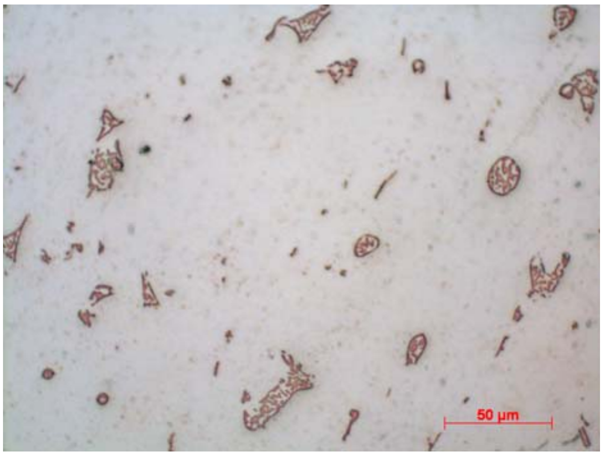

Fig. 5.2.1b: Sample 5, position 2

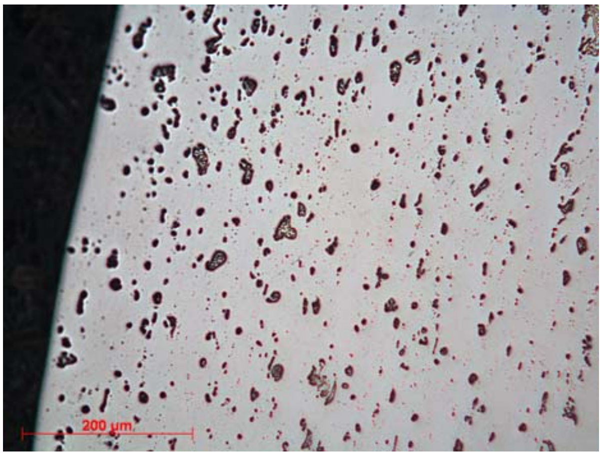

Fig. 5.2.1c: Sample 6, position 1

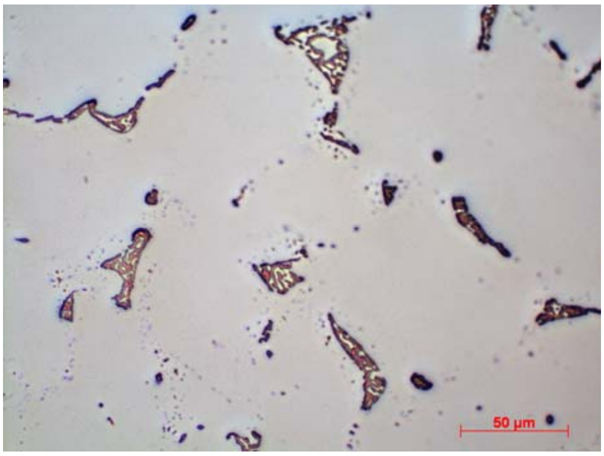

Fig. 5.2.1d: Sample 6, position 2

During light microscopy inspection, no porosities were found because they were closed through extrusion. Most significant change in the images after extrusion is the size of the copper phases. As it can be observed in Fig. 5.2.1a-d, they are much smaller than in the as-cast condition. No significant difference was observed between the microstructure of sample 5 and 6.

5.2.2 Scanning electron microscope analysis

In this chapter, only the results of sample 5 are presented because sample 6 exhibits almost the same properties as sample 5. Fig. 5.2.2 *(b-d)* shows the backscatter electron microscopy images of the structure of the homogenized and extruded specimen at different magnification rates. α + θ - phase are distributed more smoothly than in the as-cast condition, see Fig. 5.2.2 *(a)*.

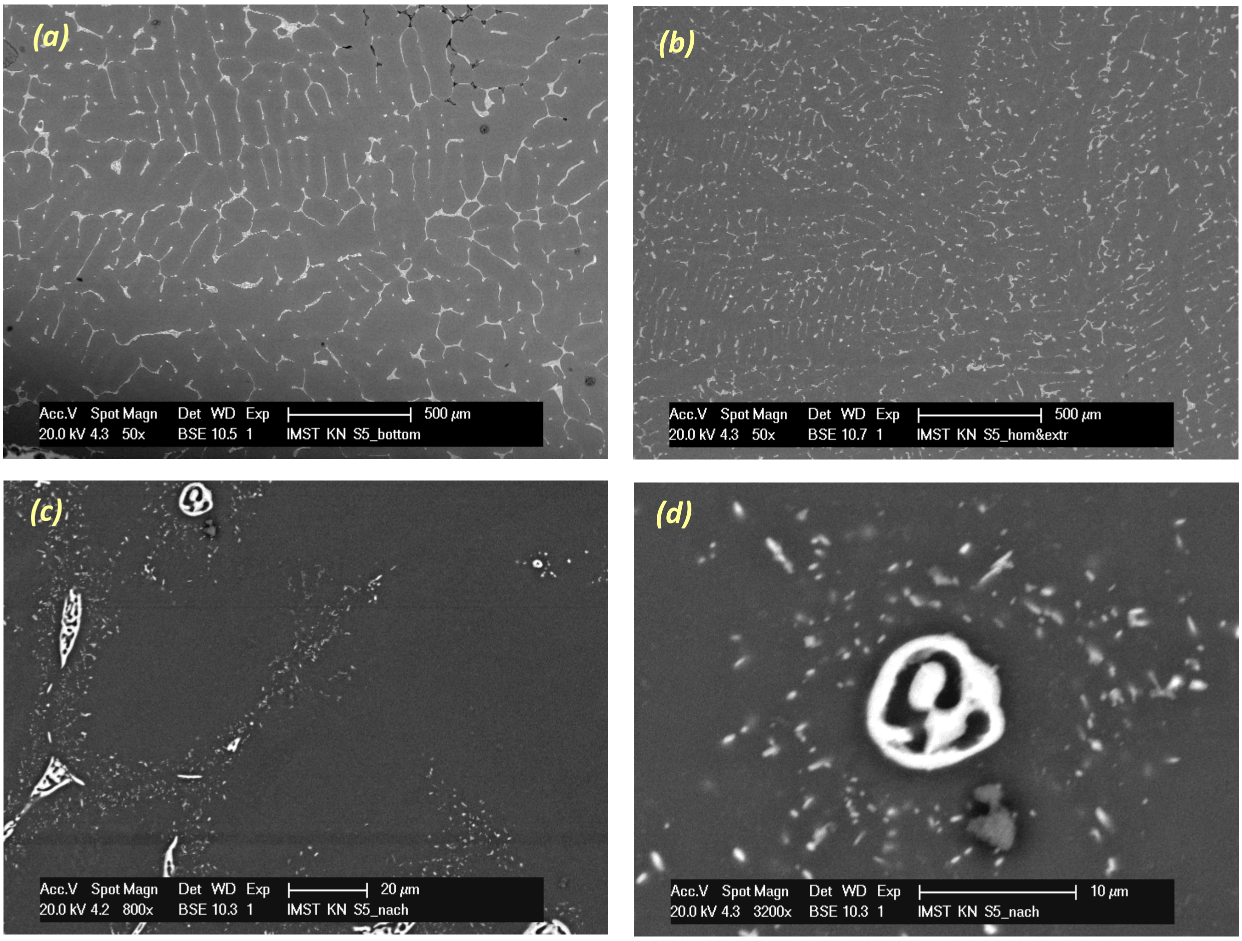

Fig. 5.2.2: Scanning electron microscope view of sample 5 in *(a)* as-cast condition is brought here for comparison; *(b-d)* after homogenization and extrusion

Furthermore, the ratio of aluminum and copper of the specimen was determined. Moreover, a mapping analysis at position 2 was established.

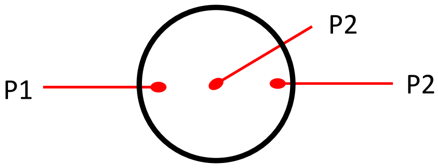

Fig. 5.2.2a: Locations of the measurement positions of sample 5 after homogenization and extrusion

All measurements were carried out at a magnification of 50x. Table 5.2.2 represents the results of the Al and Cu content of the alloy at every measurement point and the average value of the alloy´s composition. The deviation of the average value from the reference input was also determined.

Table 5.2.2: Sample 5: Deviation of the alloy´s composition from the reference input of 4,3 wt% Cu

Element	**Alloy composition in wt% at different positions**			**Average**
	Measurement P1	Measurement P2	Measurement P3	
Al	95,04	94,90	94,90	94,947
Cu	4,96	5,10	5,10	5,053

Element	**Deviation from the reference of 4.3 wt% Cu in [%]**
Cu	+17,51

The alloy´s composition in wt% is almost the same at every measurement position. The deviation values of +15,58% in the as-cast condition and + 17,51% after homogenization and extrusion are almost equal. Measurement uncertainty is present but the values are for every specimen higher than the reference input and do not vary strongly. The scanning electron microscope analysis is therefore exact enough to prove a homogeneous copper distribution in the alloy.

Mapping analysis was carried out for the components Al and Cu at position P2 in Fig. 5.2.2a. For the homogenized and extruded specimen, a higher magnification rate (500x) was chosen than for the specimen in the as-cast condition. Fig. 5.2.2b-f shows the mapping results for sample 5.

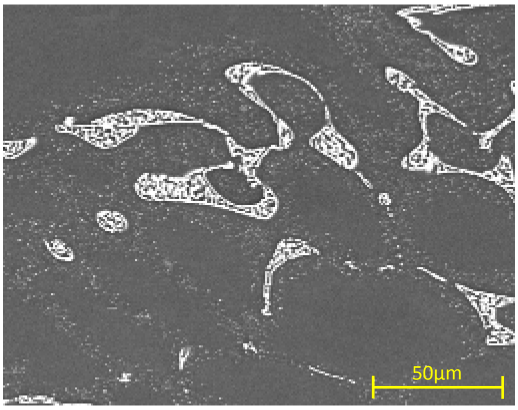

Fig. 5.2.2b: Microscopic structure

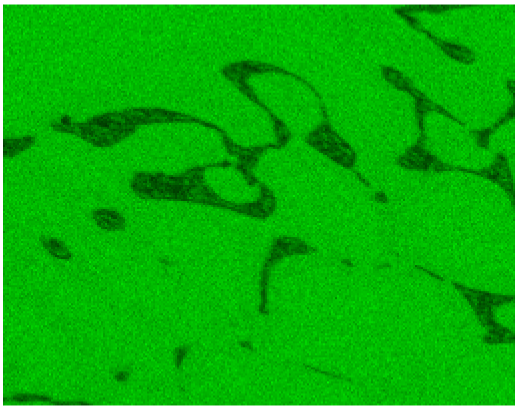

Fig. 5.2.2c: Aluminum distribution

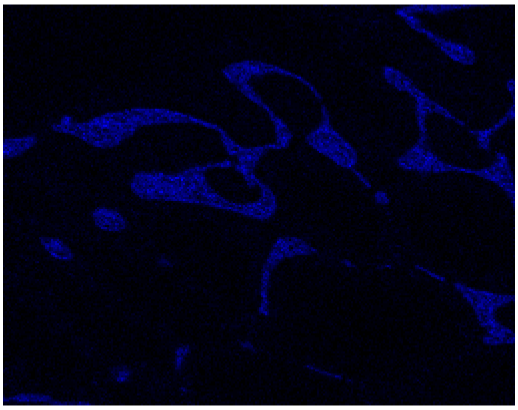

Fig. 5.2.2d: Copper distribution

The Al matrix is shown in green and the distribution of Cu in blue. The blue regions consist of the θ-phase.

5.2.3 Hardness measurement

The hardness of sample 5 and 6 was measured after heat treatment. Every specimen was solution heat treated at 550°C for 25min, quenched in water to room temperature and naturally aged, results see Fig. 5.2.3 and Table 9.1.2a-b. In Table 5.2.3, manufacturing characteristics of the two samples are repeated.

Table 5.2.3: Manufacturing characteristics of sample 3, 5 and 6

Designation	**Composition [wt%]**	**Used crucible**	**Surrounding area**	**Deformation degree during extrusion**
Sample 5	Al-4,3Cu	Graphite	Vacuum	3,24
Sample 6	Al-4,3Cu	Boron nitride	Vacuum	3,71

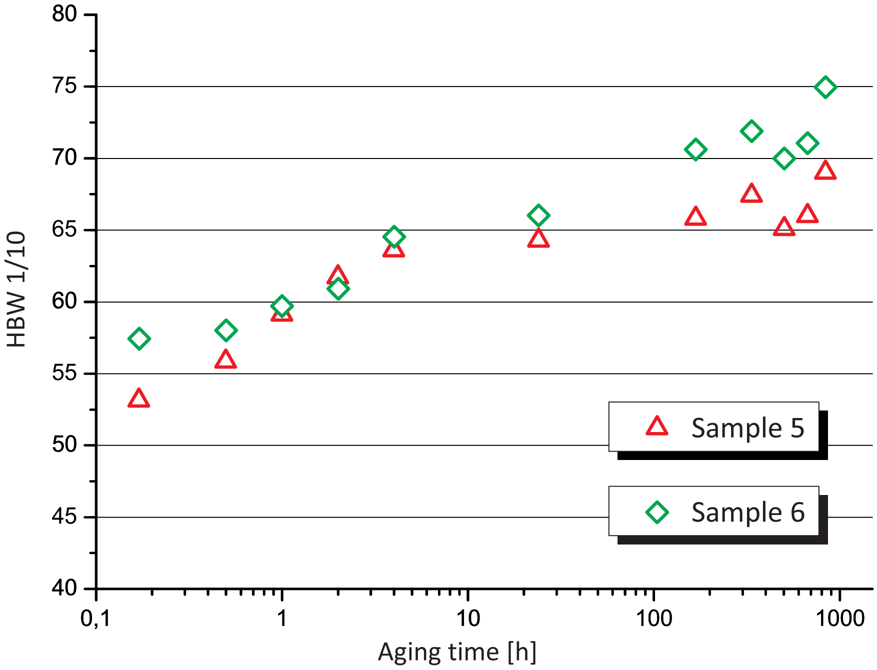

Fig. 5.2.3: Age-hardening curves of the Al-4,3Cu alloys at room temperature

Sample 5 exhibits the lowest hardness values with the exception of the value at 2 hours and reaches 69 HBW after 5 weeks. The hardness increase after quenching is consistent for both samples. Sample 6 exhibits the highest deformation degree during extrusion and reaches a hardness value of 74,9 HBW after 5 weeks. Most significant is the difference of 5,9 HBW between the two samples after 5 weeks which could be due to finer distribution of θ-phase in the matrix of sample 6 after extrusion.

5.2.4 Differential Scanning Calorimetry

For sample 5 the DSC analysis was applied. The DSC curves for the heating rates of 5, 10 and 20K/min are shown in Fig. 5.2.4a. The specimens were solution heat treated at 550°C for 25min, quenched in water to room temperature and aged 30min at room temperature before DSC with the stated rates was applied. The peaks appear most pronounced at a heating rate of 20K/min, but to be able to compare with given values of literature the heating rate of 10K/min was chosen for further DSC tests for this material.

For the heating rate of 10K/min, two exothermic peaks can be identified. Peak A between 80°C and 100°C and C between 325°C and 345°C. Furthermore, three endothermic peaks are visible. B between 160°C and 180°C, D between 405°C and 420°C and E between 470°C and 485°C. It seems, that between peak D and E a further exothermic peak is present, but the curve is deluding because peak E and peak D closely follow one another.

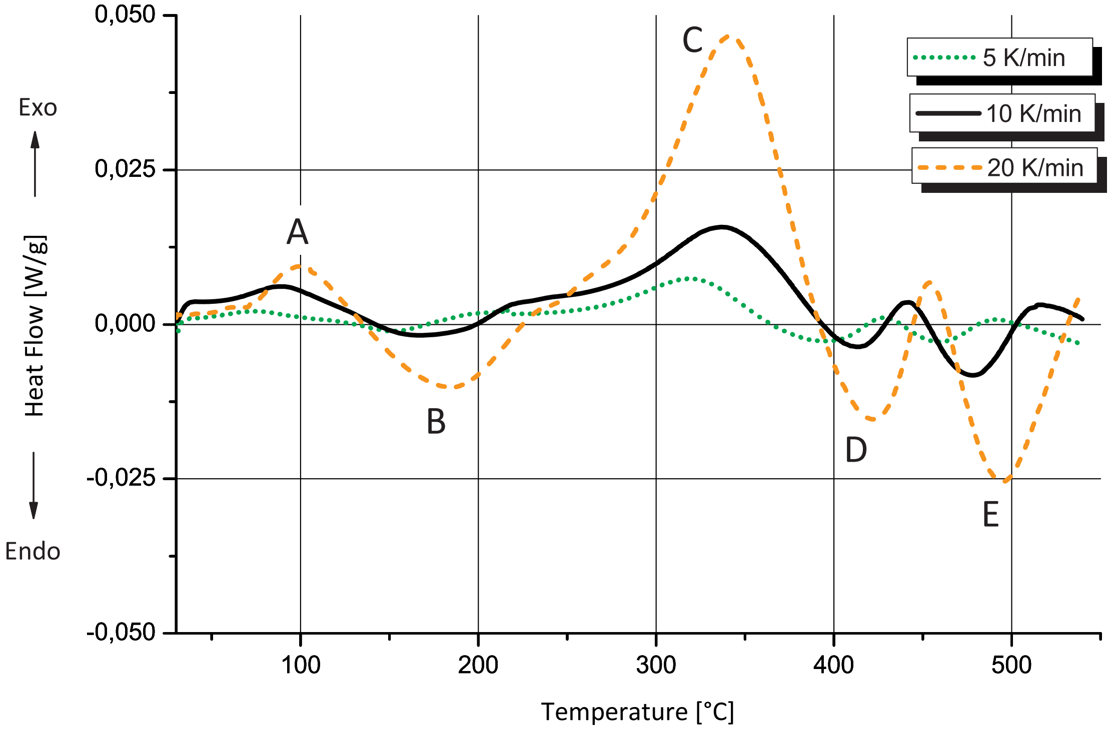

Fig. 5.2.4a: DSC curves of sample 5 at different heating rates

The curves in Fig. 5.2.4b are the 2nd run of DSC and are consistent with each other and accordingly, the comparison of the three DSC curves in Fig. 5.2.4a is possible.

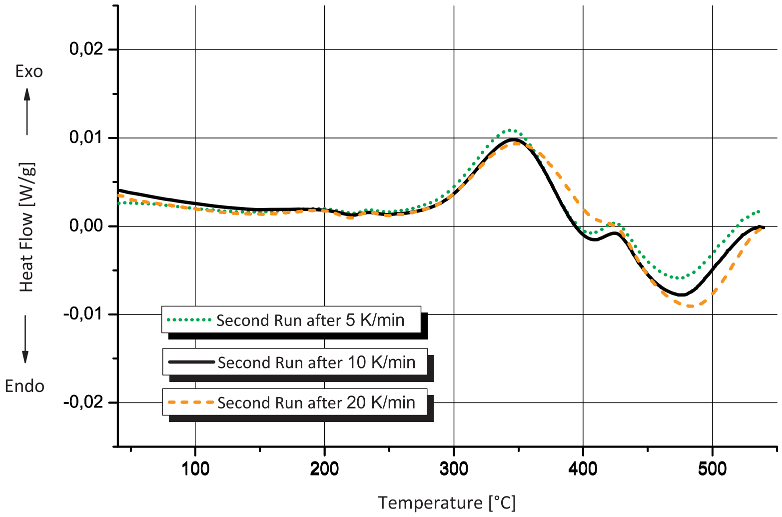

Fig. 5.2.4b: DSC curves of sample 5 after the first run, heating rate 5K/min

The aging behavior of sample 5 is shown in Fig. 5.2.4c. The specimens were room temperature aged for 30min and 2 weeks.

Peak A between 80°C and 100°C appears only for the specimen aged for 30min. Most significant is the difference between the first two endothermic peaks, B1 and B2. For the longer aged specimen, peak B1 appears between 105°C and 120°C, for the 30min aged specimen between 160°C and 180°C. As expected, peak C is more distinctive for the longer room temperature aged specimen. The endothermic peaks D and E appear at almost the same temperature for both specimens.

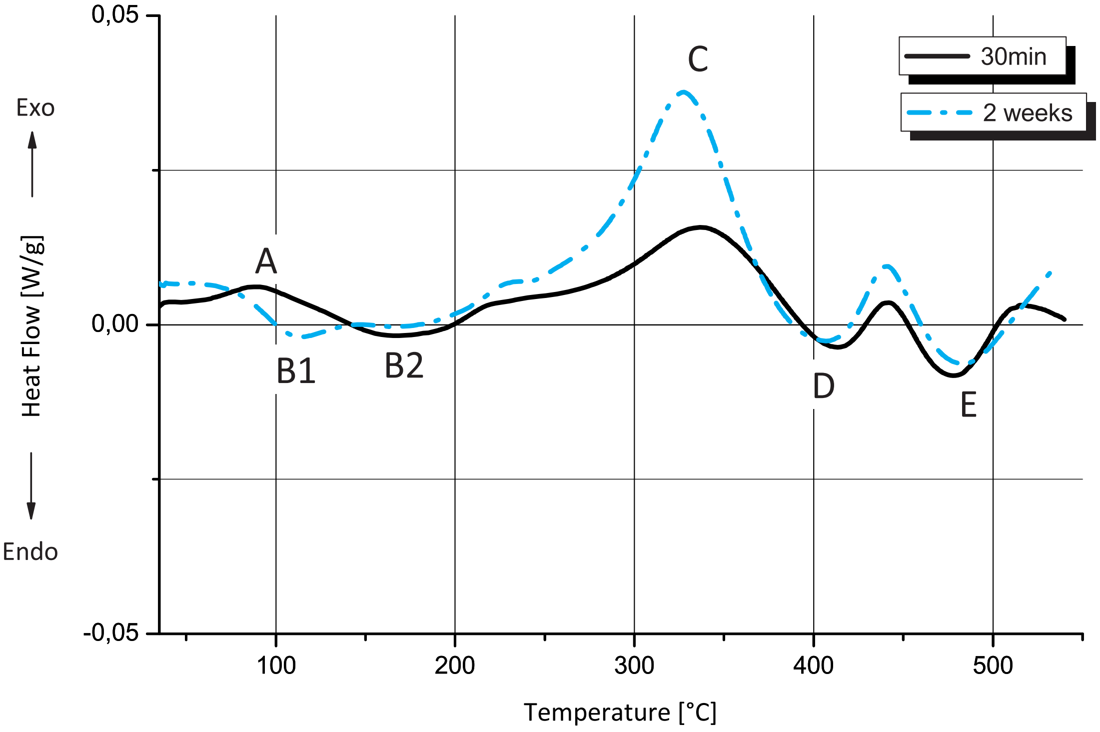

Fig. 5.2.4c: DSC curves of sample 5 at a heating rate of 10K/min after solution heat treatment at 550°C for 25min and aging for different times at room temperature

Fig 5.2.4d shows the DSC curves for the second runs of Fig. 5.2.4c. The curves are consistent with each other. That means the former results, obtained for different aging times, can be compared with each other.

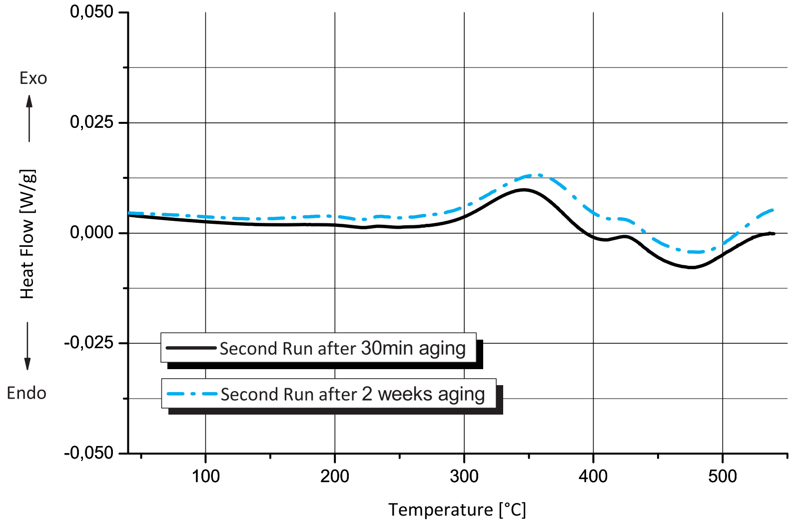

Fig. 5.2.4d: DSC curves of sample 5 after the first run, heating rate 5K/min

5.3 Characteristics of Al-Cu-Mg alloys in the as-cast condition

In Table 5.3, the properties of the manufactured Al-Cu-Mg alloys are summarized to provide an overview.

Table 5.3: Manufacturing characteristics of Al-Cu-Mg alloys

Designation	**Composition [wt%]**	**Used crucible**	**Surrounding area**
Sample 4	Al-4,3Cu-1,49Mg	Graphite	Vacuum
Sample 7	Al-4,3Cu-1,49Mg	Boron nitride	Argon

5.3.1 Al-4,3Cu-1,49Mg manufactured in a graphite crucible under vacuum

During manufacturing of sample 4, a fraction of Mg evaporated due to the vacuum of 6,8x10^{-2} mbar and the temperature of 800°C. Hence, the alloy was only inspected with the scanning electron microscope and the chemical composition was measured with EDX to enable measuring the extent of vaporization, of the 1,49 wt% Mg input.

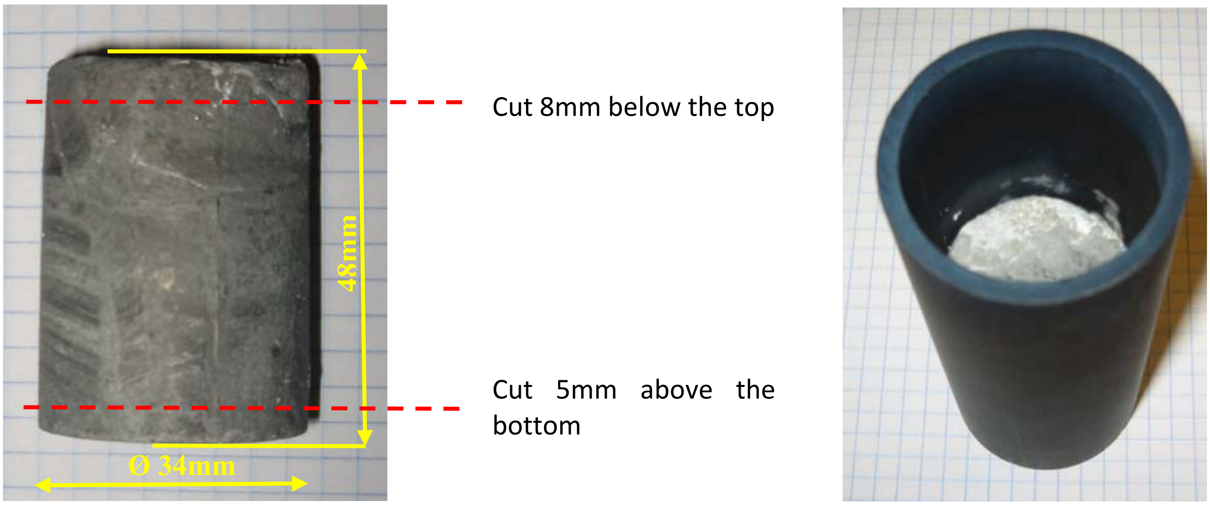

Fig. 5.3.1: Locations for microscopic analysis of sample 4, Al-4.3Cu-1.49Mg and the graphite crucible after the evaporation of a magnesium fraction

On the right, Fig. 5.3.1 shows the blue-discolored graphite crucible through the magnesium vapor.

5.3.1.1 Scanning electron microscope analysis

The ratio of aluminum, copper and magnesium at the bottom and the top of the specimen was determined. Fig. 5.3.1.1 shows the measurement positions.

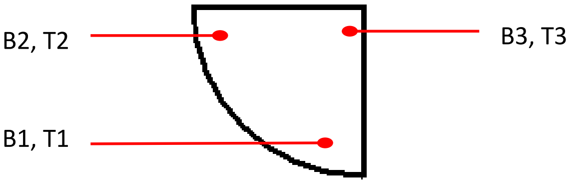

Fig. 5.3.1.1: Location of the measurement positions

The approach was the same, as for sample 2, 3 and 5. First, the average values were calculated and finally the deviation from the reference input was determined in Table 5.3.1.1.

Table 5.3.1.1: Sample 4: Deviation of the alloy´s composition from the reference input of 4,3 wt% Cu and 1,49 wt% Mg

Element	**Average alloy composition in wt% at different positions**		**Overall average alloy composition in wt%**
	Bottom	Top	
Al	93,173	93,457	93,315
Cu	5,754	5,53	5,642
Mg	1,073	1,013	1,043
Element	**Deviation from the reference input of 4,3 wt% Cu and 1,49 wt% Mg in [%]**		
	Bottom	Top	**Overall**
Cu	+33,81	+28,60	+31,21
Mg	-27,99	-32,01	-30,00

At all measurement positions, the content of copper is higher than the reference input of 4,3wt%. In contrast, the magnesium content with -30% is lower which means extensive lose of magnesium. To avoid the evaporation of Mg, sample 7 was manufactured under argon.

5.3.2 Al-4,3Cu-1,49Mg manufactured in a boron nitride crucible under argon

Sample 7 was manufactured under gas atmosphere of argon to avoid the evaporation of Mg. Light microscope and scanning electron microscope analyses were applied. The specimens of sample 7 were taken from the same locations as for sample 4.

5.3.2.1 Light microscope analysis

The specimens were inspected at the positions represented in Fig. 5.3.2.1. Every specimen was scanned in order to find porosities.

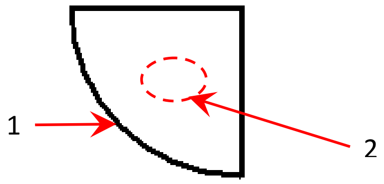

Fig. 5.3.2.1: Location of the view positions at the top and the bottom of sample 7

Results for the “bottom-specimen”:

Fig. 5.3.2.1a and b shows the microstructure at the border and in the middle of the bottom specimen.

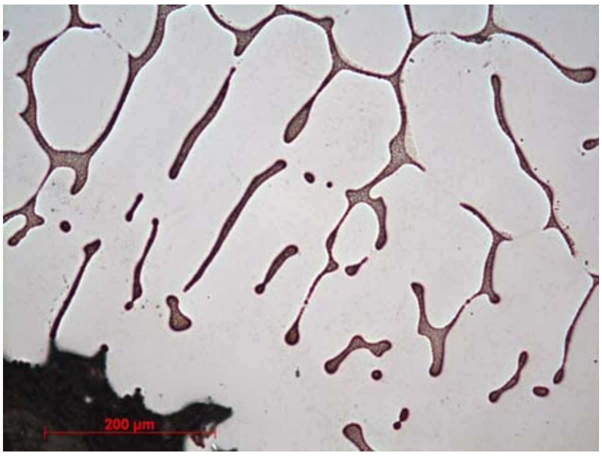

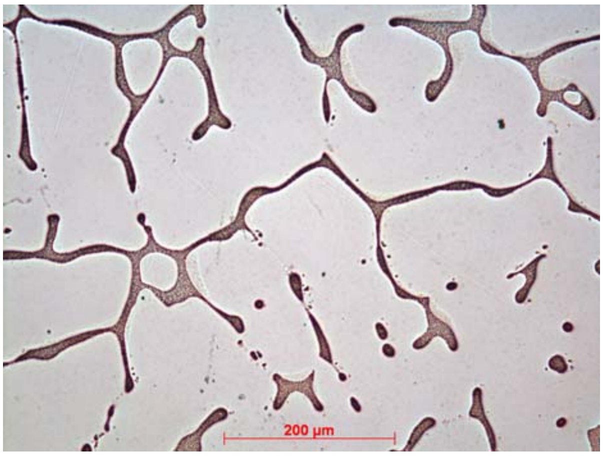

Fig. 5.3.2.1a: Microscopic view at position 1

Fig. 5.3.2.1b: Microscopic view at position 2

Results for the “top-specimen”:

Fig. 5.3.2.1c and d show the microstructure at the border and in the middle of the top specimen.

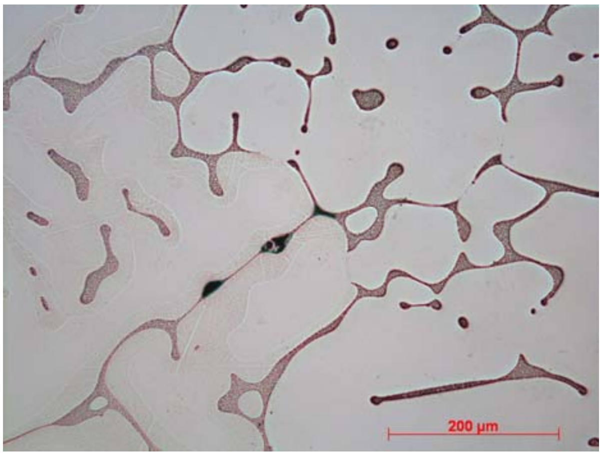

Fig. 5.3.2.1c: Microscopic view at position 1

Fig. 5.3.2.1d: Microscopic view at position 2

Sample 7 shows an equal copper distribution at the top and the bottom. Porosities were found rarely, however they appear as well at the bottom as at the top.

5.3.2.2 Scanning electron microscope analysis

The ratio of aluminum, copper and magnesium at the bottom and the top of the specimens was determined by EDX. All measurements were carried out at a magnification rate of 50x. The measurement procedure is the same as explained before. Summary of the results is given in Table 5.3.2.2.

Table 5.3.2.2: Sample 7: Deviation of the alloy´s composition from the reference input of 4,3 wt% Cu and 1,49 wt% Mg

Element	**Average alloy composition in wt% at different positions**		**Overall average alloy composition in wt%**
	Bottom	Top	
Al	92,553	92,433	92,493
Cu	5,367	5,527	5,447
Mg	2,08	2,04	2,06
Element	**Deviation from the reference input of 4,3 wt% Cu and 1,49 wt% Mg in [%]**		
	Bottom	Top	**Overall**
Cu	+24,81	+28,53	+26,67
Mg	+39,60	+36,91	+38,26

The deviation values for the alloying elements are in an acceptable range. According to the measurement Mg is present with approximately 2wt% in the alloy. This proves that Mg has not evaporated. Measurement uncertainty is present, but the measured values are for every specimen higher than the reference input and do not vary strongly. The EDX analysis is therefore exact enough to prove a homogeneous copper and magnesium distribution in the alloy.

5.4 Characteristics of Al-Cu-Mg alloys after homogenization and extrusion

In this chapter, the characteristics of sample 7 after homogenization and extrusion are represented. Light and scanning electron microscope analysis, hardness measurements and differential scanning calorimetry were applied.

5.4.1 Light microscope analysis

Fig. 5.4.1a and b show the microstructure at the edge and in the middle of the sample with different magnifications.

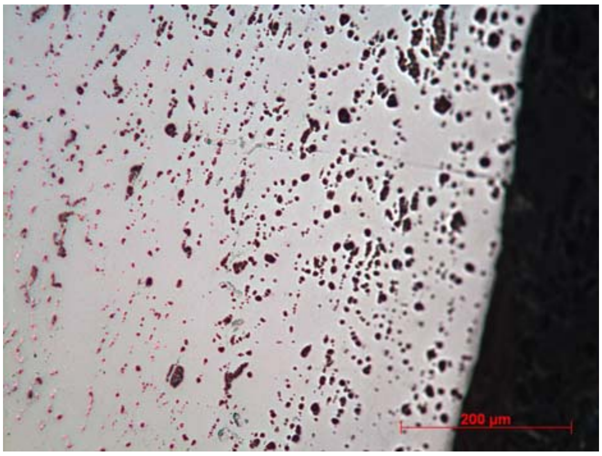

Fig. 5.4.1a: Sample 7 at the edge

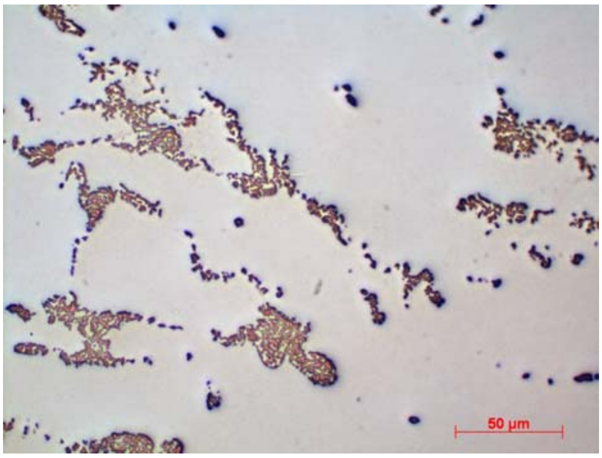

Fig. 5.4.1b: Sample 7 in the middle

Compared with the microstructure in the as-cast condition (see Fig. 5.3.2.1a-d), the intermetallic phases are smaller. During optical microscopy inspection, no porosities were found because they were closed during extrusion. The alloying elements (copper and magnesium) are homogeneously distributed in the aluminum matrix, see the scanning electron microscope analysis in the next chapter.

5.4.2 Scanning electron microscope analysis

Fig. 5.4.2 shows the microstructure at different magnification rates.

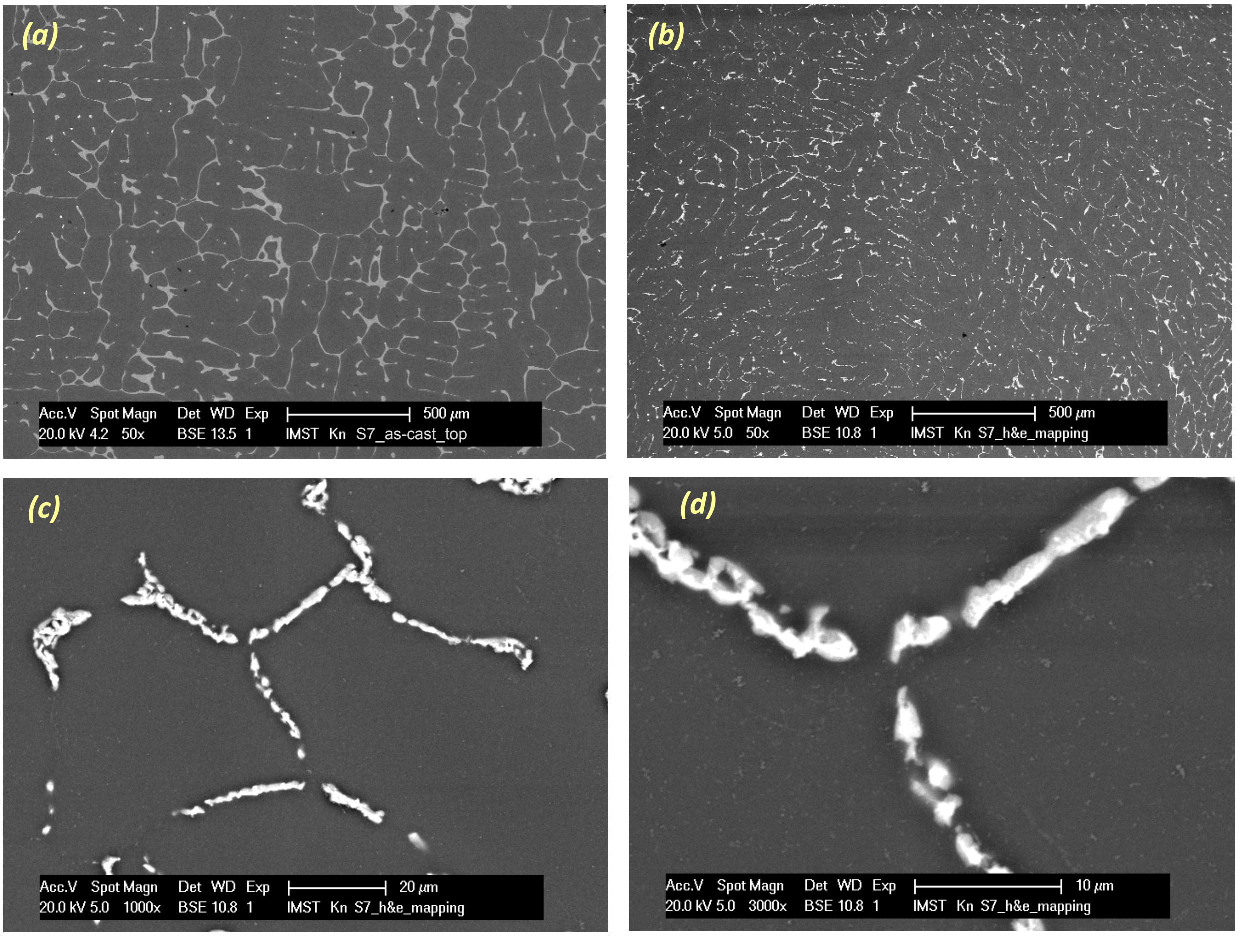

Fig. 5.4.2: Scanning electron microscope view of sample 7 in *(a)* as-cast condition; *(b-d)* after homogenization and extrusion at different magnifications

The results in Table 5.3.2.2 confirm that the alloy´s composition is 94,21Al-4,3Cu-1,49Mg and hence, in this chapter no composition measurements are presented. Distribution of the phases after extrusion is smoother than in the as-cast condition, see difference in Fig. 5.4.2 *(a)* and *(b)*. To demonstrate the Cu and Mg distribution, element-mapping at a magnification of 500x (Fig. 5.4.2a–e) was carried out.

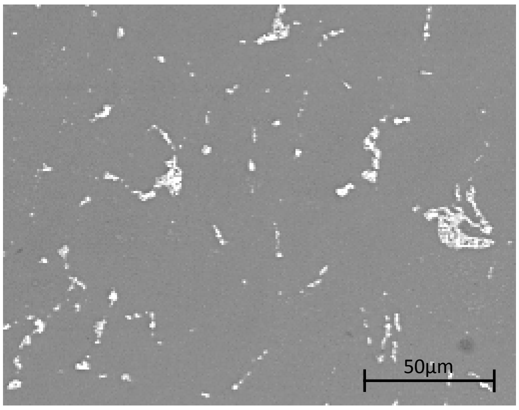

Fig. 5.4.2a: Microscopic structure

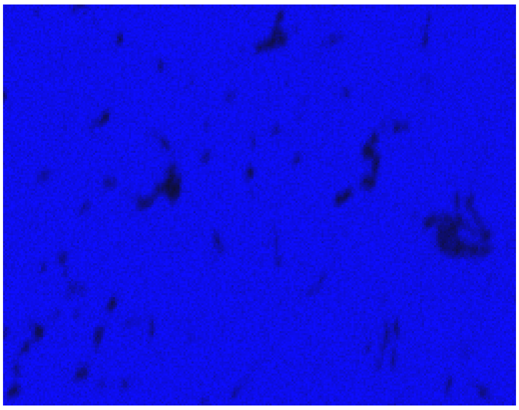

Fig. 5.4.2b: Aluminum matrix

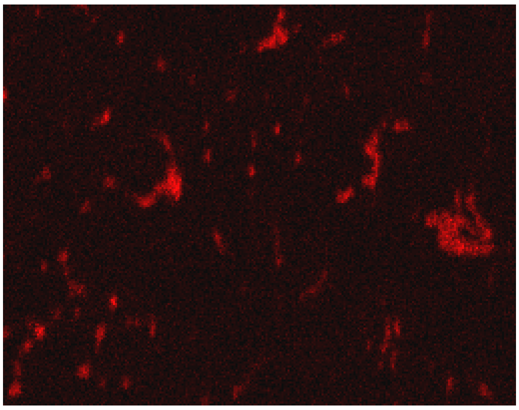

Fig. 5.4.2c: Copper distribution

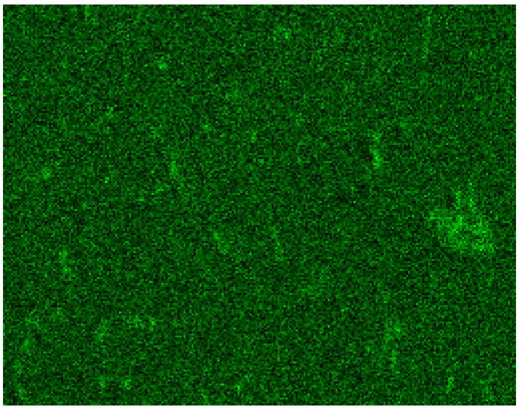

Fig. 5.4.2d: Magnesium distribution

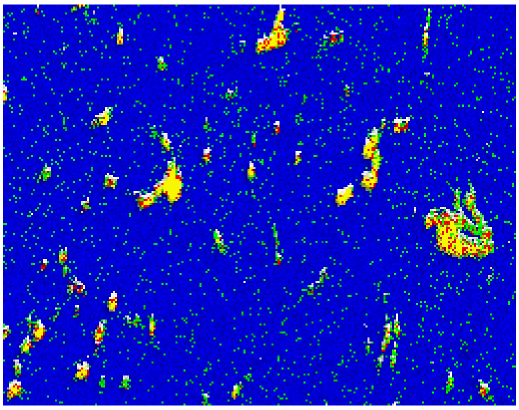

Fig. 5.4.2e: Overlapped: Al, Cu and Mg

The mapping results at a magnification rate of 1000x shows Fig. 5.4.2f–j.

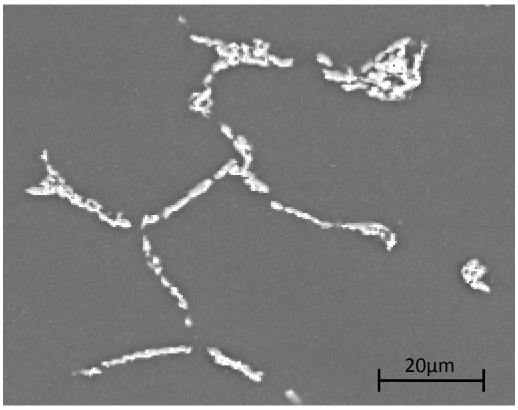

Fig. 5.4.2f: Microscopic structure

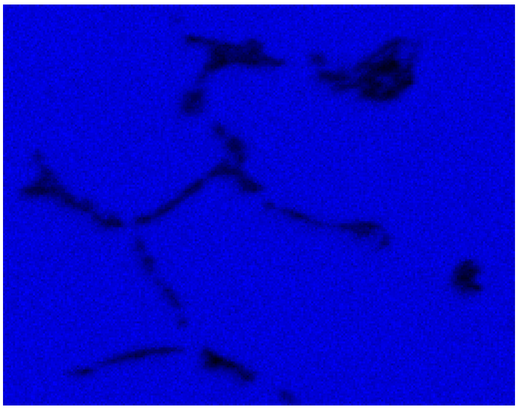

Fig. 5.4.2g: Aluminum matrix

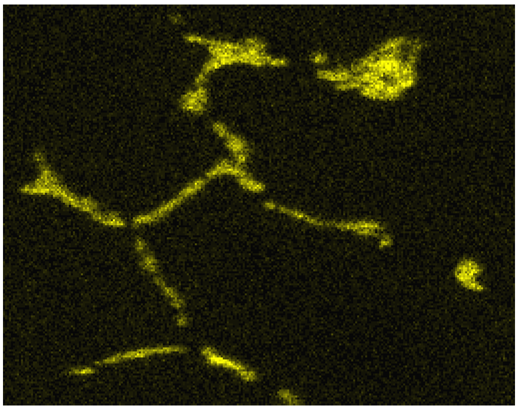

Fig. 5.4.2h: Copper distribution

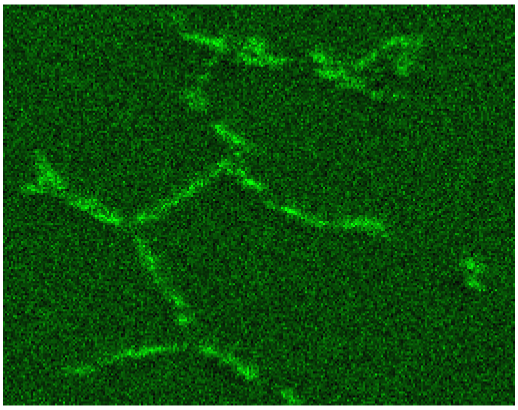

Fig. 5.4.2i: Magnesium distribution

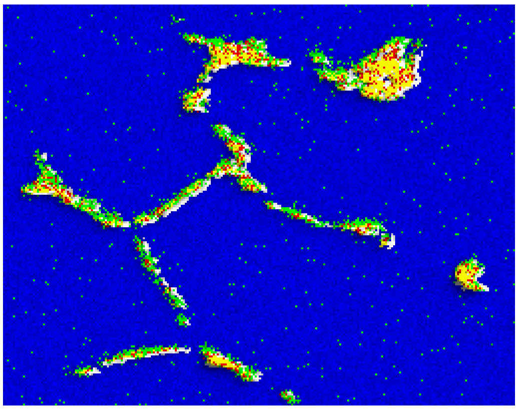

Fig. 5.4.2j: Overlapped: Al, Cu and Mg

5.4.3 Hardness measurement

Sample 7 has been solution heat treated at 495°C for 30min, quenched in water to room temperature and naturally aged. Changing of hardness is illustrated in Fig 5.4.3 and Table 9.1.3.

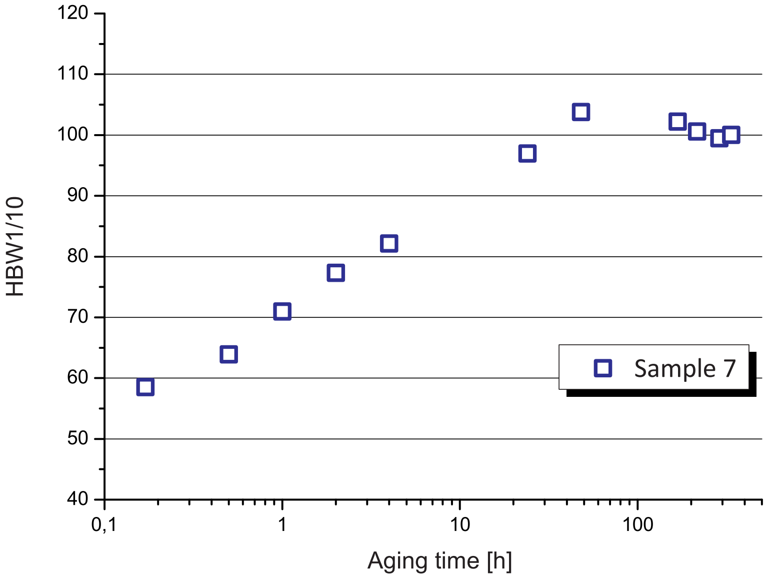

Fig. 5.4.3: Age-hardening curve of sample 7 (Al-4,3Cu-1,49Mg) at room temperature

After 2 days, when the hardness of approximately 104 HBW1/10 is reached, the values start to decrease slowly.

5.4.4 Differential Scanning Calorimetry

Sample 7 was naturally aged for 30min, 2 days and 2 weeks after solution heat treatment and quenching to room temperature. The DSC curves are presented in Fig. 5.4.4a.

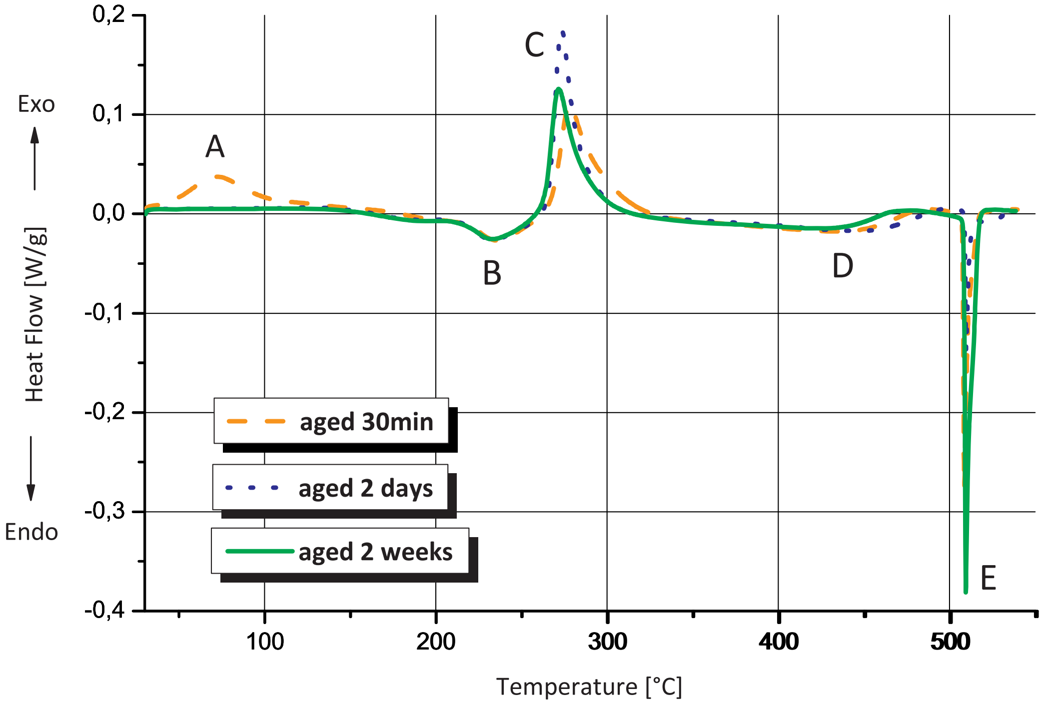

Fig. 5.4.4a: DSC curves of sample 7 at a heating rate of 10K/min. The specimens were solution heat treated at 495°C for 30min, quenched and aged at room temperature for different times before DSC measurement

The observation of the DSC curves shows two exothermic peaks. Peak A between 65°C and 75°C and C between 270°C and 280°C. Furthermore, three endothermic peaks are visible. B between 230°C and 240°C, a broad peak D between 405°C and 455°C and E between 505°C and 515°C.

Fig. 5.4.4b shows the DSC results of the 2^{nd} run.

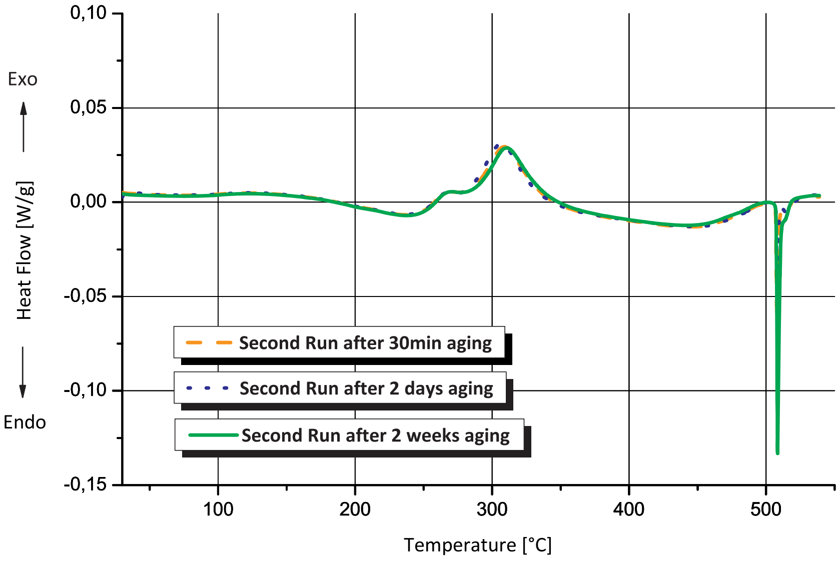

Fig. 5.4.4b: DSC curves of sample 7 after the first run, heating rate 5K/min

5.5 Characteristics of an industrial 2024 aluminum alloy

Light microscope, scanning electron microscope, hardness measurements and differential scanning calorimetry were applied to characterize the alloy. Some properties of the 2024 aluminum alloy, such as it´s composition were known because of former analyses. The results of former spectroscopic analyses are listed in Table 5.5.

Table 5.5: Composition of the industrial 2024 aluminum alloy

Element	Content [wt%]
Cu	4,3
Mg	1,49
Mn	0,71
Fe	0,13
Si	0,07
Cr	<0,01
Ni	<0,01
Zn	0,02
Ti	0,05
Ga	0,01

5.5.1 Light microscope analysis

Fig.5.5.1a and b show the microscopic view at different magnification rates.

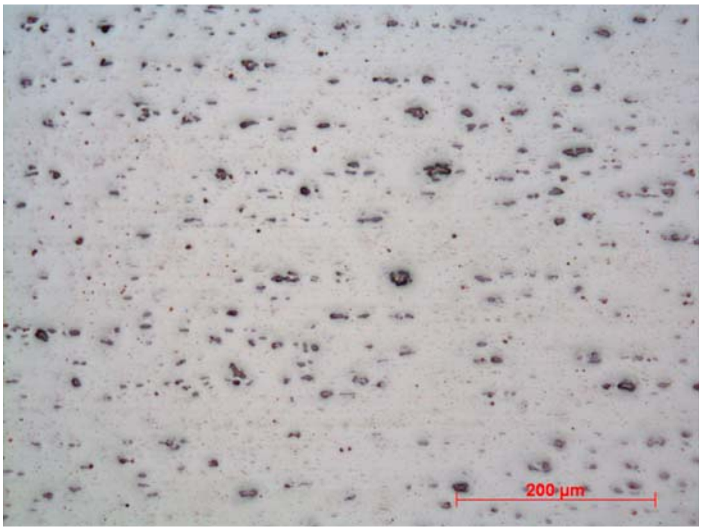

Fig. 5.5.1a Light microscope view of the 2024 aluminum alloy

Due to the aligned structure in Fig. 5.5.1a, the rolling direction of the wrought alloy can be determined.

Rolling direction

→

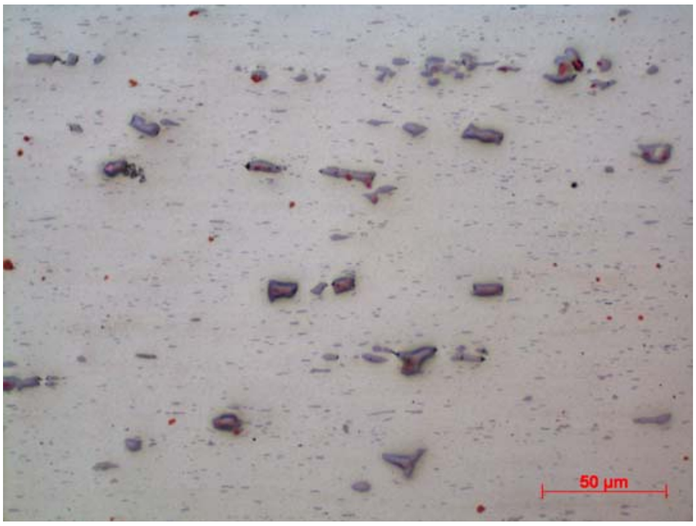

Fig. 5.5.1b Light microscope view of the 2024 aluminum alloy

Fig. 5.5.1b shows the microscopic structure at a higher magnification. A detailed identification of the different alloy components like Cu, Mg, Mn, Fe, Si and intermetallic phases is very difficult. Therefore scanning electron microscope analysis equipped with EDX was applied.

During light microscopic inspection, no porosities were found.

5.5.2 Scanning electron microscope analysis

Element-mapping was carried out for the components Al, Cu, Mg, Mn, Fe and Si at a magnification of 1000x. Fig. 5.5.2a-g shows the results for the specimen. Fig. 5.5.2a is the BSE image of the same position as the mapping images.

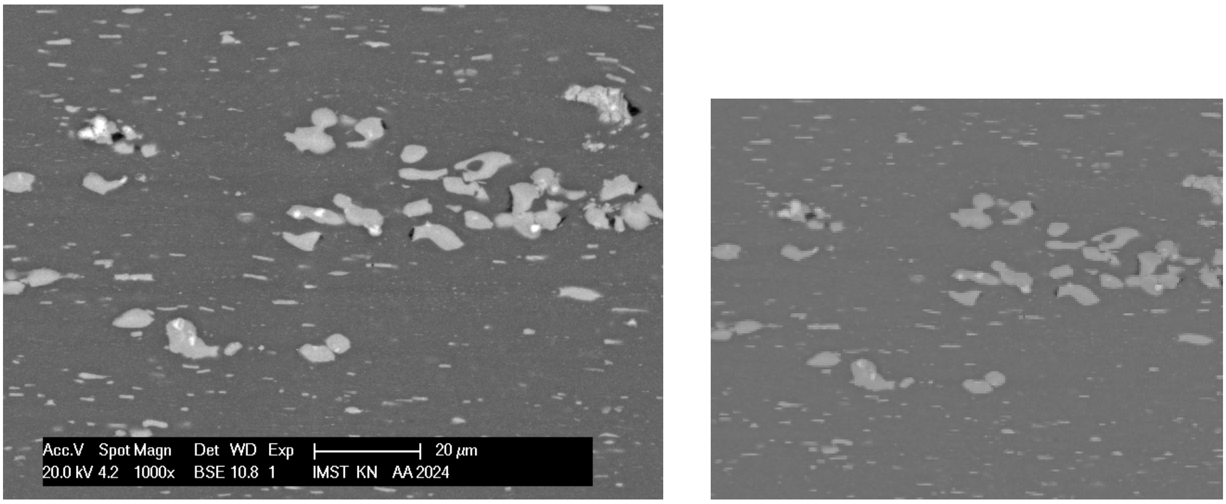

Fig. 5.5.2a: Basic position for mapping of the 2024 alloy in the original condition

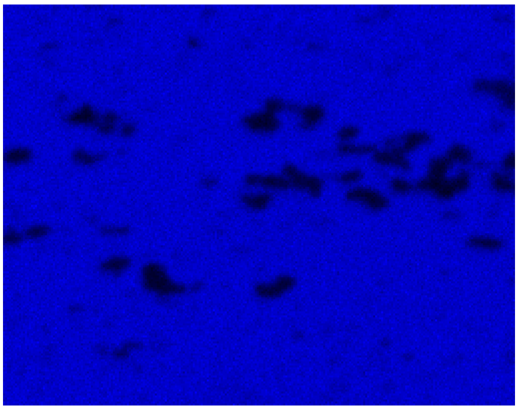

Fig. 5.5.2b: Aluminum matrix of S1

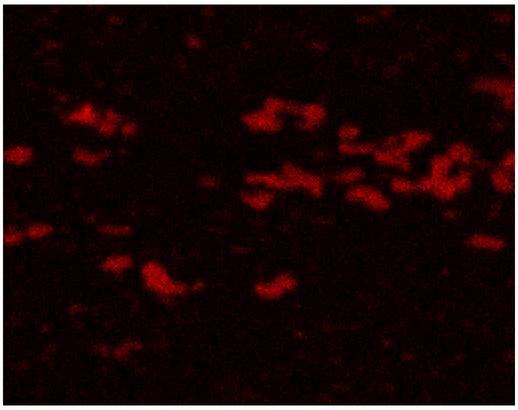

Fig. 5.5.2c: Copper distribution of S1

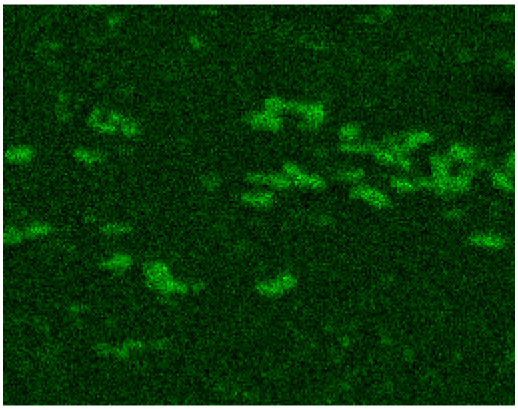

Fig. 5.5.2d: Magnesium distribution of S1

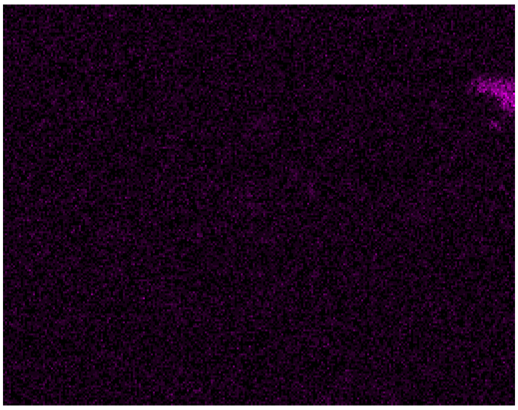

Fig. 5.5.2e: Manganese distribution of S1

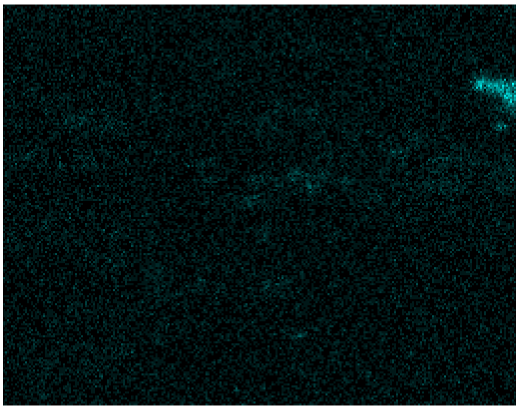

Fig. 5.5.2f: Iron distribution of S1

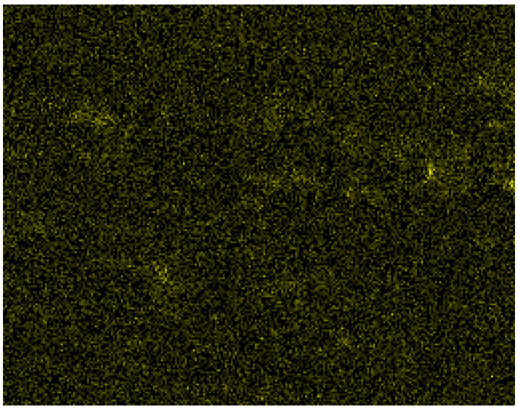

Fig. 5.5.2g: Silicium distribution of S1

The mapping results for the solution heat treated (550°C for 25min) and quenched specimen S2 are shown in Fig. 5.5.2h-n.

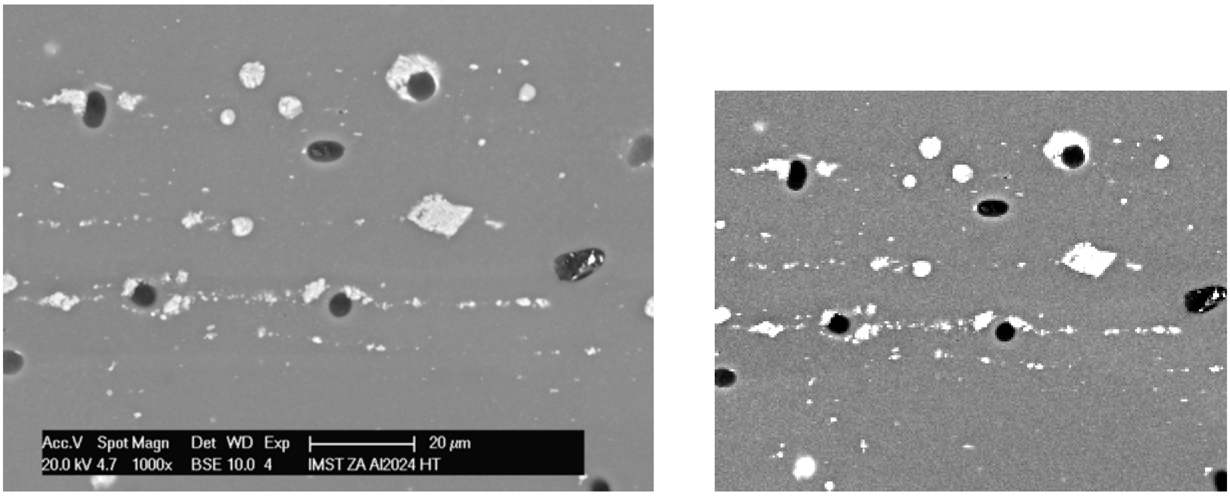

Fig. 5.5.2h: Basic position for mapping of the 2024 alloy after heat treatment

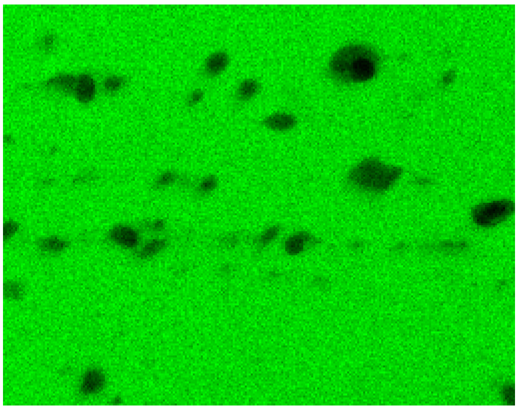

Fig. 5.5.2i: Aluminum matrix of S2

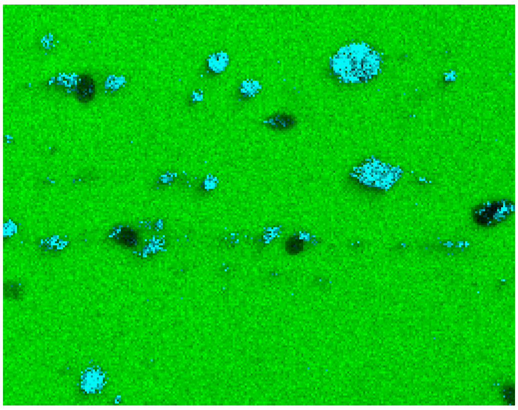

Fig. 5.5.2j: Copper distribution of S2

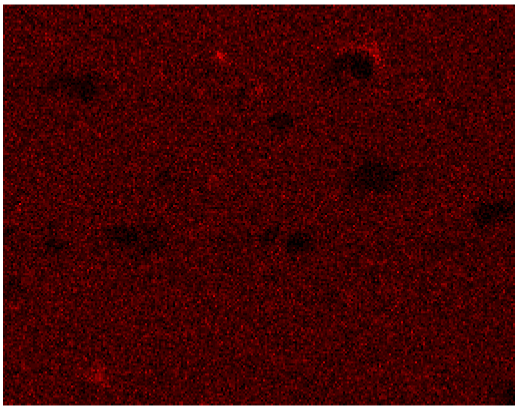

Fig. 5.5.2k: Magnesium distribution of S2

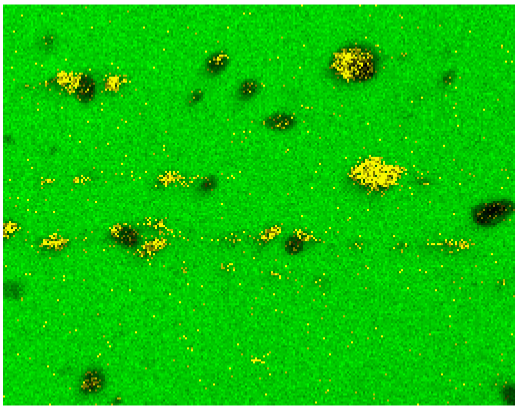

Fig. 5.5.2l: Manganese distribution of S2

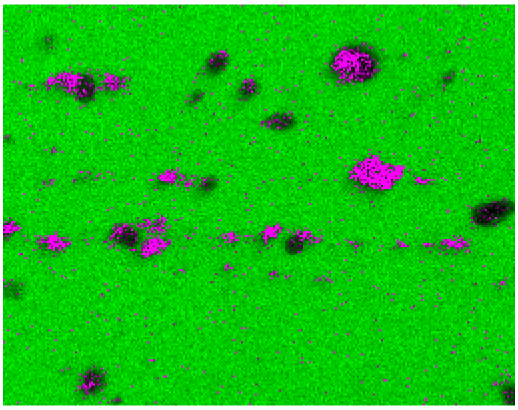

Fig. 5.5.2m: Iron distribution of S2

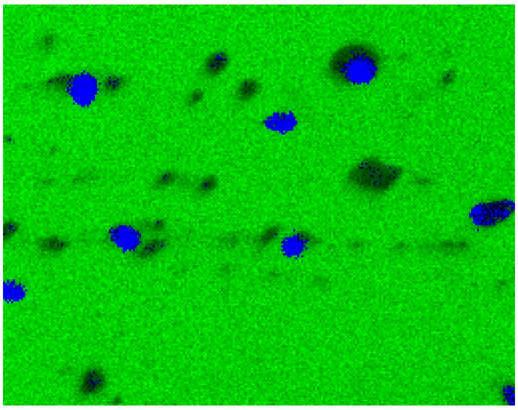

Fig. 5.5.2n: Silicium distribution of S2

5.5.3 Hardness measurement

The first specimen was solution heat treated at 550°C and the second one at 495°C for 25min. Both specimens were subsequently quenched in water to room temperature and they were naturally aged, results see in Fig 5.5.3 and Table 9.1.4a and b.

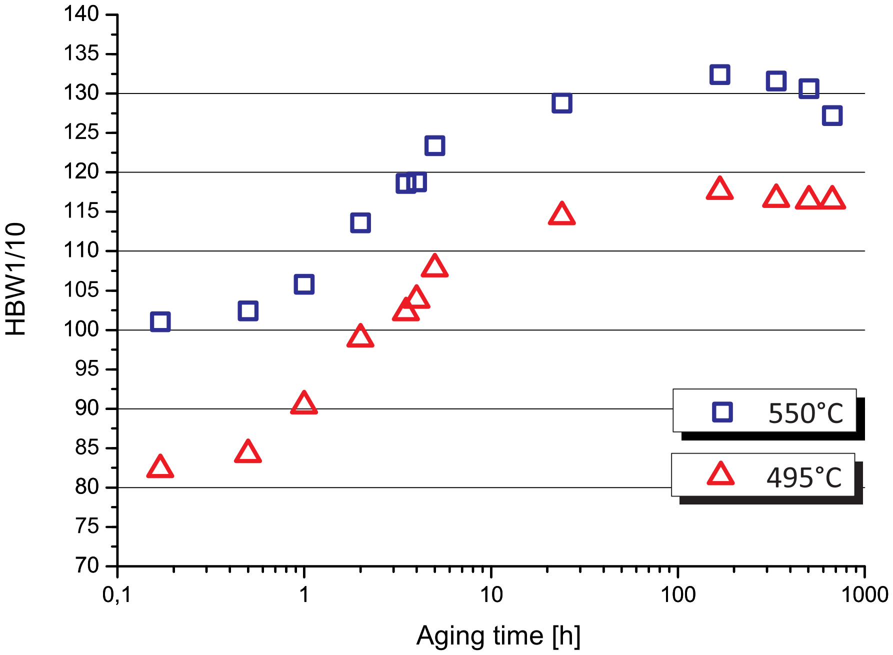

Fig. 5.5.3: Age-hardening curves of the industrial 2024 aluminum alloy at room temperature

After quenching, the hardness curve increases and reaches it´s maximum value between 1 day and 1 week. After 1 week, the precipitation procedure is completed. The specimen which was solution treated at the higher temperature shows higher hardness values. The calculation of measurement inaccuracy is represented in chapter 9.1.4.

5.5.4 Differential Scanning Calorimetry

The specimens were solution heat treated at 550°C for 25min and quenched in water to room temperature. DSC analyses were started 30min after quenching and room temperature aging. The peaks appear most pronounced at a heating rate of 20K/min, but to be consistent with given values of literature, a heating rate of 10K/min was chosen for further DSC tests with this material (see Fig. 5.5.4a).

Two exothermic peaks can be identified in this figure. A between 60°C and 90°C and C between 260°C and 320°C. Furthermore, three endothermic peaks are visible. B between 220°C and 255°C, D between 460°C and 500°C and E between 505°C and 515°C.

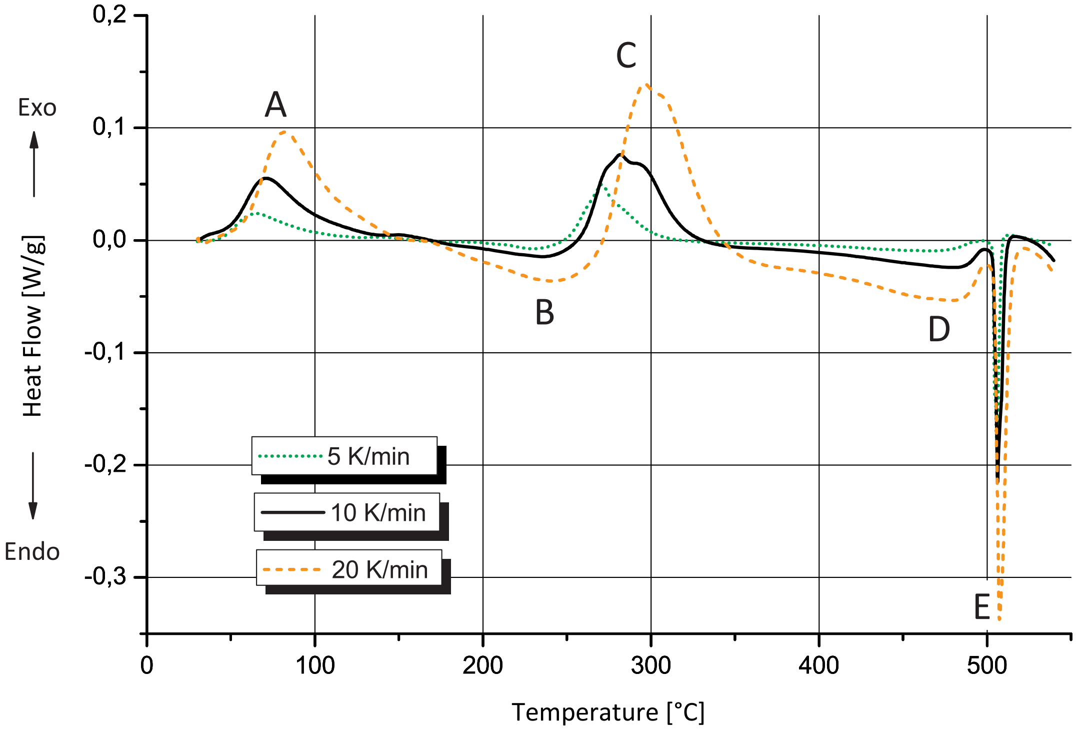

Fig. 5.5.4a: DSC curves of the 2024 aluminum alloy with different heating rates

Fig 5.5.4b shows the heating curves for the second DSC runs. The curves are consistent with each other, that means the former results, shown in Fig. 5.5.4a were correct and comparable to each other.

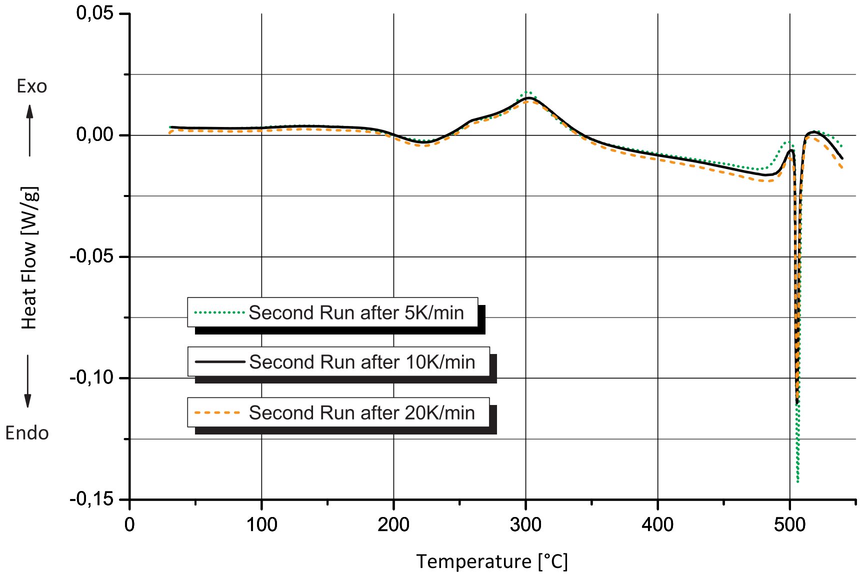

Fig. 5.5.4b: DSC curves of the 2024 aluminum alloy after the first run with a heating rate of 5K/min

A further specimen has been solution heat treated at 495°C for 25min to see the effect of a lower solution treatment temperature on the DSC curve and also to be able to compare with values of literature. DSC analysis was started 30min after quenching and room temperature aging and a heating rate of 10K/min was chosen. The result of the DSC curve is presented with the result obtained in 5.5.4a for the same material but different solution treatment and the same heating rate in Fig. 5.5.4c.

Three exothermic peaks can be identified in this figure. A between 60 and 80°C and C_1&C_2 between 260 and 300°C. Furthermore three endothermic peaks are visible: B between 215 and 245°C, D between 460 and 490°C and E between 505 and 520°C. For the specimen which was solution treated at 550°C , peak C_1 and C_2 tend not completely to overlap as peak A.

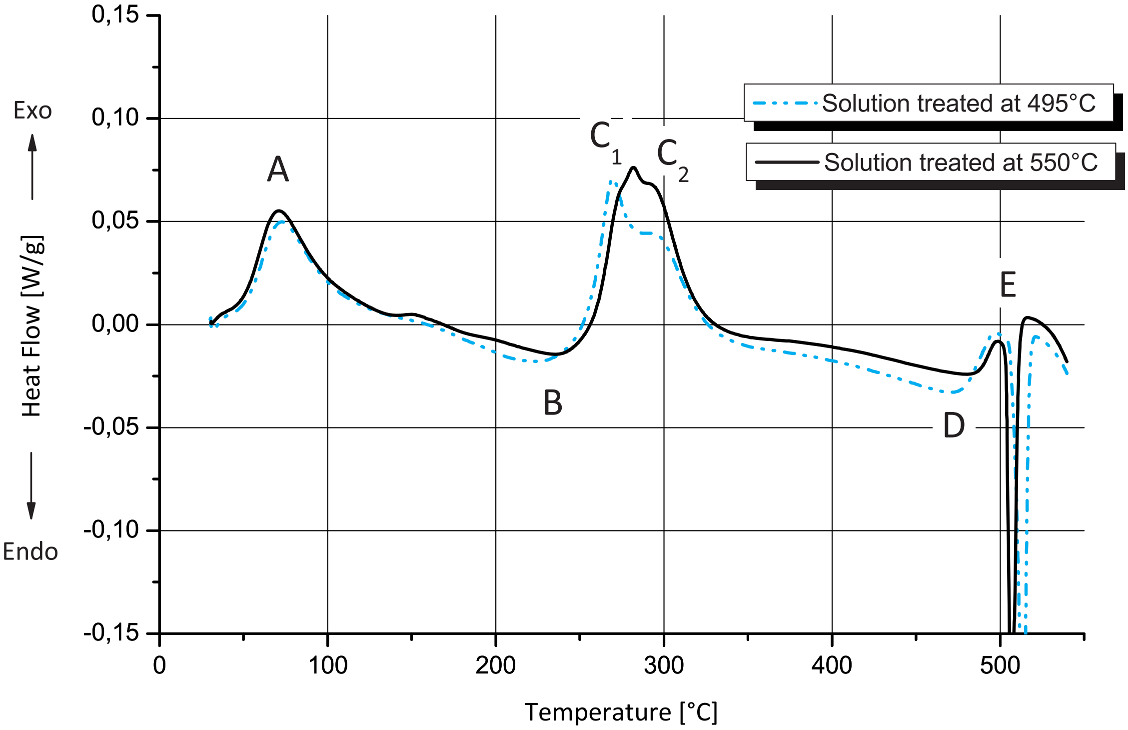

Fig. 5.5.4c: DSC curves of the 2024 aluminum alloy at a heating rate of 10K/min and two different solution heat treating temperatures

Fig 5.5.4d shows the heating curves for the second DSC runs. The curves are consistent with each other, that means the former results obtained for solution heat treating at 495 and 550°C can be compared with each other.

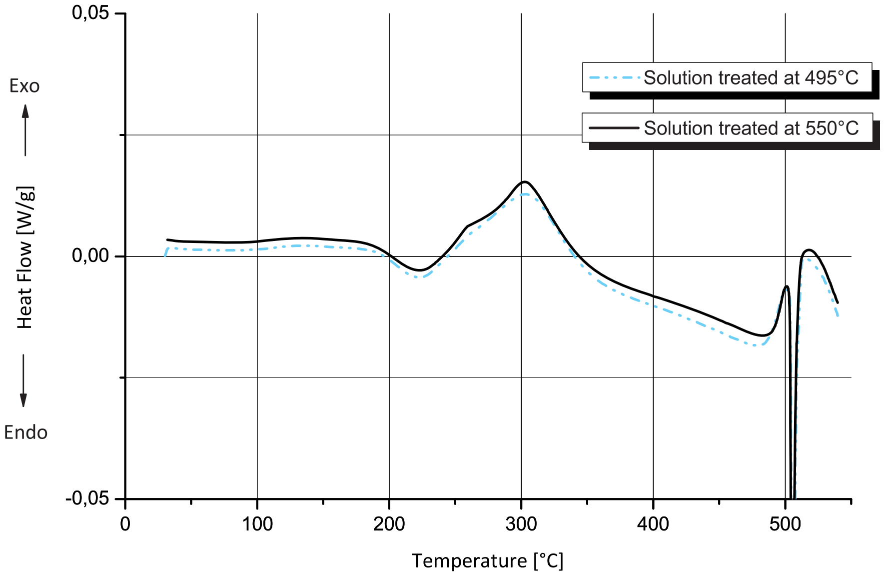

Fig. 5.5.4d: Second run DSC curves of the 2024 aluminum alloy for the two different solution heat treating temperatures, heating rate 5K/min

A specimen was solution heat treated at 550°C for 25min, quenched in water and room temperature aged for 2 weeks. In Fig. 5.5.4e, the results were overlapped with the specimen which has been aged for 30min.

As a result, two exothermic peaks can be identified in this figure. A between 60°C and 80°C and C between 270°C and 295°C. Four endothermic peaks appeared too. B between 215°C and 245°C, D between 460°C and 490°C and E between 505°C and 520°C. Furthermore, between peak A and B an endothermic peak is visible for the specimen aged for 2 weeks.

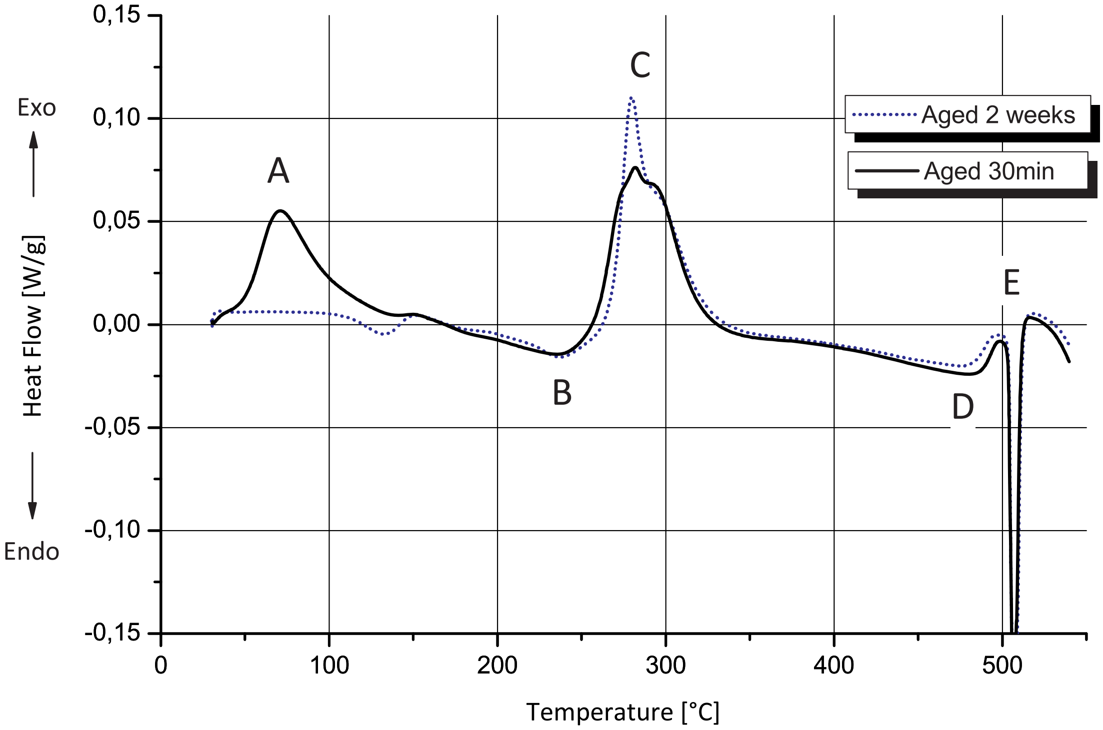

Fig. 5.5.4e: DSC curves of the 2024 aluminum alloy at a heating rate of 10K/min for specimens solution heat treated at 550°C for 25min and aged for different times at room temperature

Fig 5.5.4f shows the heating curves for the second DSC runs. The curves are consistent with each other, that mean the former results obtained for different aging times can be compared.

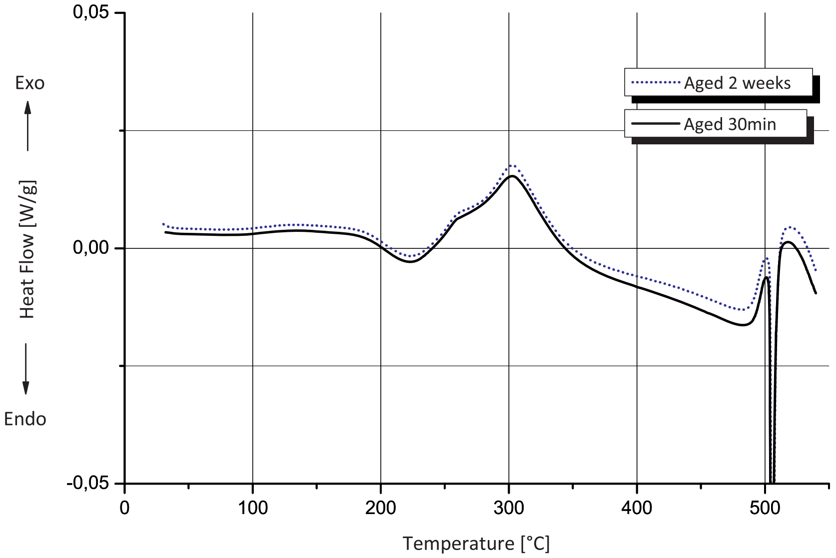

Fig. 5.5.4f: Second run DSC curves of the 2024 aluminum alloy for the specimens with different aging times, heating rate 5K/min

Fig. 5.5.4g shows the DSC curves of the specimens which were solution heat treated at 495°C and 550°C, quenched and aged two weeks at room temperature. As can be observed from the diagram, peak C is higher for the specimen with the higher solution treating temperature.

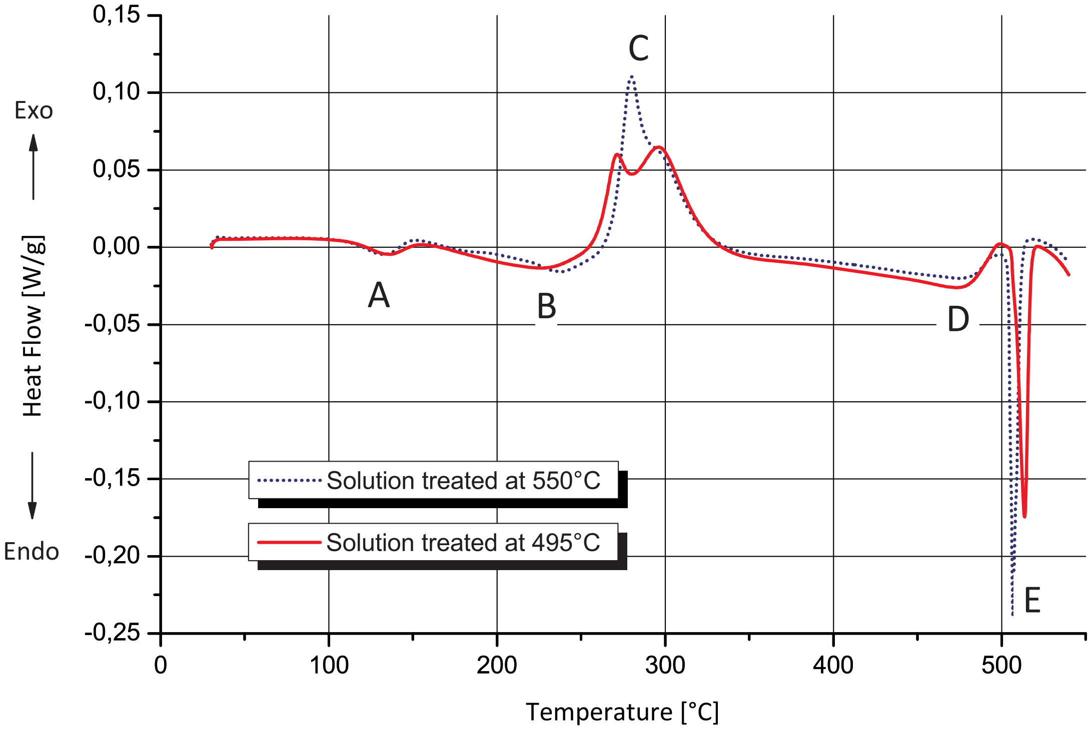

Fig. 5.5.4g: DSC curves of the 2024 aluminum alloy at a heating rate of 10K/min for specimens solution heat treated at 550°C and 495°C for 25min and aged 2 weeks at room temperature

The curves in Fig. 5.5.4h represent the 2nd run of DSC curves and are consistent with each other, accordingly the comparison of the two DSC curves in Fig. 5.5.4g is allowable.

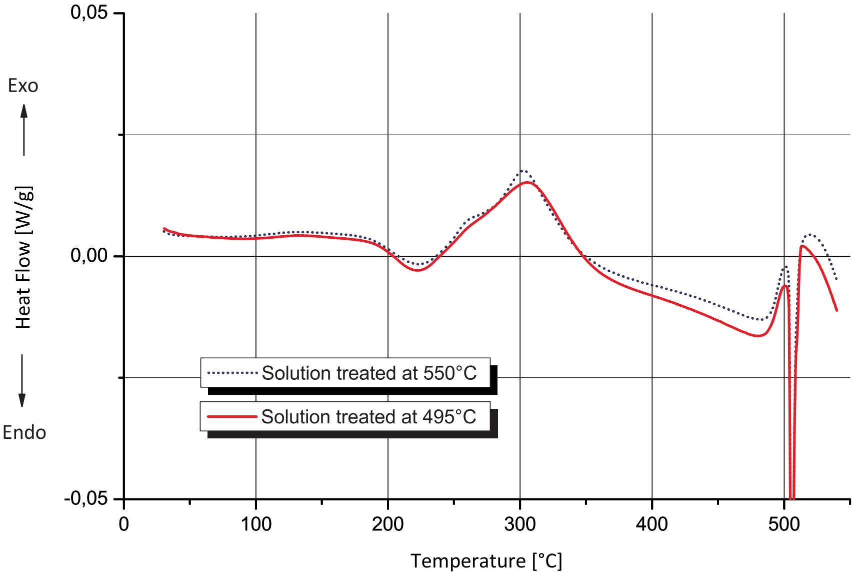

Fig. 5.5.4h: Second run DSC curves of the 2024 aluminum alloy for the two different solution heat treating temperatures, heating rate 5K/min

6 Discussion

In this chapter, the general manufacturing characteristics and the microstructural investigations before and after extrusion of the manufactured Al-Cu and Al-Cu-Mg alloys are discussed. Furthermore, the results of the manufactured Al-Cu-Mg alloy are compared with those of the industrial 2024 aluminum alloy.

6.1 Al-Cu alloys

6.1.1 General manufacturing characteristics

The main objective was to gather and develop the necessary know-how to use correctly the existing facilities to produce different aluminum alloys. A homogeneous microstructure is very important for the manufactured alloys and this task was well fulfilled by the induction furnace. Light and scanning electron microscopy proved that copper is homogeneously distributed in the aluminum matrix. Gravity had no influence on the copper distribution between the top and the bottom of the samples. Taking into account the intermetallic precipitated phases, the manufactured alloys exhibit a homogeneous phase distribution for each approach. Copper dissolution in the aluminum melt proceeded without any difficulty. The distinct advantages of the induction furnace are stirring motions in the melt and this is also confirmed in [17].

The results in Table 5.1.2 show that the temperature at the bottom of the crucible is always higher than at the top. When the thermocouple measured 650°C, aluminum began to melt at the bottom and after reaching 690°C the solid aluminum bars glided into the melt. Aluminum has a melting point of 660,32°C and hence this demonstrates that the induction coil does not heat the graphite crucible more than the material inside.

If a crucible executes a similar effect like a faraday cage, the stirring effect of the induction coil on the melt would be decreased. The used graphite crucible has an electrical resistivity of 34,7 – 6030 µOhm*cm and the boron nitride one of $3{,}16*10^{20}$ – $3{,}16*10^{21}$ µOhm*cm [21]. The difference of approximately 10^{16} µOhm*cm could have influenced the alloy´s microstructure mixing. For the graphite crucible, the stirring effect of the induction coil in the melt was a little lower than in the silicon oxide and boron nitride crucible. This effect was observed only visually.

Light and scanning electron microscopy results (see chapter 5.1.1 – 5.1.5) confirmed that whether a graphite, a silicon oxide or a boron nitride crucible is used, the microstructure stays equal when the furnace atmosphere is the same.

Advantages of the graphite crucible:

- Possibility of temperature measurement with a thermocouple in the bottom of the crucible
- The induction coil can be pilot-controlled (in contrast, the induction coil capacity has to be regulated manually when the boron nitride crucible is used)

Advantages of the boron nitride crucible [21]:

- Higher temperature resistance
- Higher thermal resistivity

6.1.2 Characteristics in the as-cast condition

In the experiment, manufacturing under different surrounding atmospheres had an effect on the number of porosities. This behavior was observed during the microscopic analysis.

During cooling of sample 6, the vacuum was lower as for sample 5. As an effect, this could have had an effect on the number of porosities during solidification.

Feeding the chamber with the inert gas argon provides a protective atmosphere around the melt and therefore no reaction between air and melt occurs. The low pressure on the melt could have influenced the number of porosities during solidification.

6.1.3 Characteristics in the homogenized and extruded condition

The recipient of the used extrusion machine had a defined diameter of 40mm and the sample´s diameter had to be as close to this value as possible because a smaller diameter means, that the sample could be deformed and expanded to the recipient´s diameter during extrusion. The diameter of samples manufactured in the graphite crucible was limited to 34mm. Despite of the smaller diameter, no interfusion between the surface and the core was observed (see Fig. 5.2.2). Sample 6, which was manufactured in the boron nitride crucible, had a diameter of 39mm in the as-cast condition and therefore the deformation degree during extrusion was higher. The extrusion led to closing of the pores (see Fig. 5.2.1a-d), which were observed in the as-cast condition (see Fig. 5.1.4.1a and Fig. 5.1.5.1c-d).

Specimens of sample 5 and 6 were solution heat treated at 550°C for 25min and quenched in water. Hardness measurements proved that a higher deformation degree increases the hardness (results see Fig. 5.2.3).

The precipitation kinetics of sample 5 (Al-4,3Cu) was inspected with hardness measurements and DSC analysis after solution heat treatment at 550°C for 25min and quenching in water. Afterward, the specimens were room temperature aged for different times and compared with the results stated in references [8], [9], [10] and [11].

The DSC curves in Fig. 5.2.4c show two exothermic peaks for the specimen which has been aged for 30 minutes. Peak A appears only for this specimen and can be lead back to the precipitation of quenched clusters [11]. The second exothermic peak C appears for every specimen in Fig. 5.2.4c and is responsible for the hardness. The higher is the peak C the harder is the material. The hardness values in Fig. 5.2.3 verify that the maximum hardness value is reached after 5 weeks. Heat treated Al-Cu alloys reach their maximum hardness after approximately 40 days if artificial aging at 130°C is applied [11]. Increasing the copper content up to the solid solubility increases the hardness [11]. In our experiment only room temperature aging has been applied for the manufactured alloys and according to [11] an estimated time of more than 4 months would be necessary to reach the maximum hardness.

The DSC curves in Fig. 5.2.4c show three endothermic peaks: B1, B2, D and E. Most significant is that the first endothermic peak B shifts to lower temperature for the longer room temperature aged specimens. The dissolution of the GP zones is responsible for peak B1 and B2 and because in the "2-weeks aged specimen" these zones already exist, peak B1 appears at a lower temperature than peak B2 [8, 11]. The remaining peaks D and E, which are due to the dissolution of θ´ and θ phases, appear almost at the same temperature for every specimen.

6.2 Al-Cu-Mg alloys

6.2.1 General manufacturing characteristics

On the contrary to the Al-Cu alloys, vacuum has a distinctive effect on the manufacturing procedure because the boiling point of magnesium in vacuum decreases up to 700°C under a pressure of about 1Pa (= $1x10^{-2}$ mbar) [5, 6]. For this reason there are two possibilities to manufacture an Al-Cu-Mg alloy with low contamination:

- The first one is to limit the vacuum and the temperature.
- Using argon as the surrounding atmosphere is the second possibility. This procedure is more expensive but avoids sublimation of magnesium in vacuum.

In practice, Al-Cu-Mg alloys are manufactured without a controlled atmosphere, see Fig. 3.4a [17].

As it was observed for the manufactured Al-Cu alloys, a homogeneous element distribution was achieved also for Al-Cu-Mg alloys. Melting of aluminum, copper and magnesium with the induction furnace proceeded without any difficulty.

6.2.2 Characteristics in the as-cast condition

As can be observed from Table 5.3.2.2 and Fig. 5.3.2.1a-d, copper and magnesium are homogeneously distributed in the aluminum matrix. The microstructure of the alloy produced with electromagnetic casting in [17] exhibits a similar result as the manufactured alloy (compare Fig. 3.4b with Fig. 5.3.2.1a-d).

Scanning electron microscopy equipped with EDX measurement proved that Mg is present with approximately 2wt%. Considering excess measurement uncertainty errors, the magnesium content of 1,49 wt% in the alloy seems to be reasonable and therefore no Mg sublimation effect is expected. The number of pores was inspected visually with the light and scanning electron microscope. It was significantly lower than in Al-Cu alloys.

6.2.3 Characteristics in the homogenized and extruded condition

Extrusion led to closing of the pores, which were observed in the as-cast condition (see Fig. 5.4.1a-b). Element-mapping analyses (see Fig. 5.4.2a-e) show the distribution of the elements Al, Cu and Mg in images and help to get information about matrix element distribution and to some extend type of intermetallic phases in the matrix. As can be observed from these figures, the “green Mg-cores” occur at the same positions as the copper ones and coincide with intermetallics visible in high magnification SEM backscattered electron images. Considering the chemical composition of the alloy most of these precipitates are stable phase $CuMgAl_2$ (S phase). Parts where no Mg is available but Cu exists in the mapping images most probably are the stable phase $CuAl_2$ (θ phase).

The same can be said for Fig. 5.4.2f-j.

After solution heat treatment and quenching, Al-Cu-Mg alloys reach during aging faster than Al-Cu alloys their maximum hardness values (compare Fig. 5.2.3 with Fig. 5.4.3) [11, 13, 17]. This feature can be lead back to different kinetics of precipitations in these two different alloys. Following observation can be made from Fig. 5.4.3 and Fig. 5.4.4a:

- Peak A in Fig. 5.4.4a is visible due to the formation of Cu-Mg co-clusters (GP zones) and peak B due to the dissolution of GP zones [13].
- DSC and hardness measurements confirmed that the formation of Cu-Mg co-clusters after solution heat treatment and quenching is completed after two days. The same results were observed in [13].
- For different aging times, peak C shows a significant character. This peak is attributed to the formation of S phase ($CuMgAl_2$) precipitates [13, 14] and is responsible for hardness. If the alloy is overaged, peak C may disappear. The highest peak value by room temperature aging will be reached for the specimen that has been aged for two days.
- Peak B, D and E occur almost at the same temperature. The dissolution of S precipitates causes peak D. Further peak E is induced by the partial melting of S+θ eutectics [14].

6.2.4 Comparison of the industrial 2024 alloy and the manufactured Al-Cu-Mg alloy

A distinct difference is the chemical analysis of both materials. Their major alloying elements Cu and Mg are the same but in the industrial aluminum alloy type 2024, there exist some accompanying elements such as Fe, Mn and Si that contribute to precipitation of different intermetallic phases from the melt (Al_2Cu_2Fe, Al_7Cu_2Fe, $Al_{12}Si(FeMn)_3$, $Al_{20}Cu_2(MnFe)_3$ and $Al_{20}Cu_3Mn_3$). Normally these intermetallic phase are stable and do not solve during solid solution treatment. These two materials have not been etched to check for their average grain size. The common expected precipitate phases between these two materials are $CuAl_2$, $CuMgAl_2$ which contribute to the main role of precipitation hardening during aging treatment.

The characteristics of both alloys are summarized in Table 6.2.4.

Table 6.2.4: Composition of the compared alloys; heat treatment before hardness measurements and DSC tests

Alloy	Alloying elements [wt%]	Heat treatment
Sample 7	4,3Cu, 1,49Mg	T4: Solution treated at 495°C for 30min, quenched and aged at room temperature
Industrial 2024	4,3Cu, 1,49Mg, 0,71Mn, 0,13 Fe, 0,07Si, < 0,01 Cr and Ni	T4: Solution treated at 495°C for 25min, quenched and aged at room temperature

A comparison of hardness values obtained after a specific time period of room temperature aging can be seen in Fig. 6.2.4.

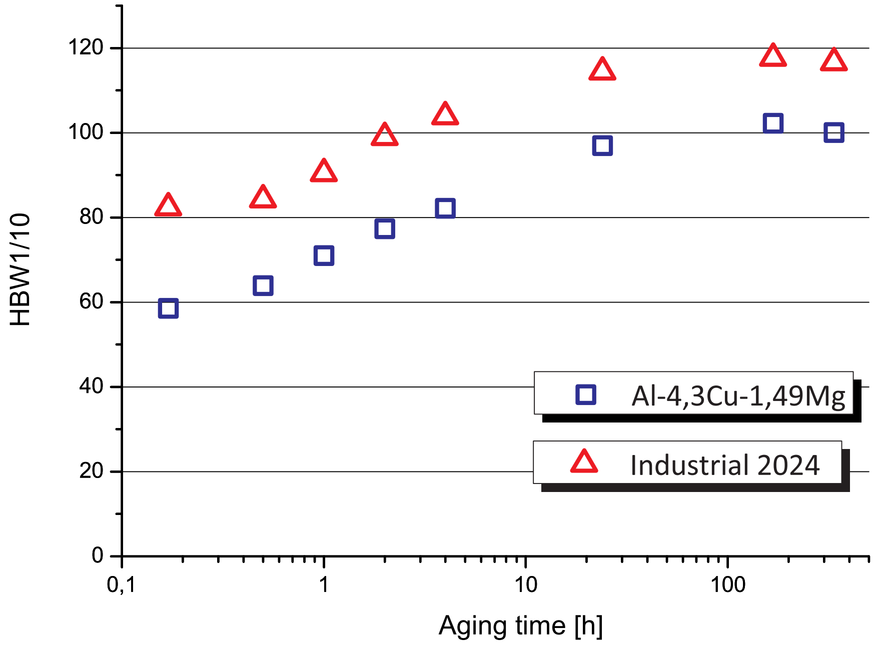

Fig. 6.2.4: Age-hardening curves of the industrial 2024 and the manufactured Al-Cu-Mg alloy at room temperature

As can be observed from Fig. 6.2.4, the industrial alloy exhibits higher hardness values. The industrial alloy was solution treated for 25min and the manufactured one for 30min which should not make a big difference for both. The manufactured alloy exhibits a hardness of about 16% less than the industrial one. The reason of higher hardness of the 2024 alloy can be discussed as follow: Trace elements like manganese and silicon improve the strengthening of aluminum [1].

The production route of both alloys is different. More deformation would be expected to be exposed on the 2024 alloy. Grain size could be different and in addition intermetallic phases which exist in 2024 can be broken during heavy rolling and contribute partially to dispersion hardening of the matrix. Following observations were made from DSC analyses for the industrial alloy:

- Increasing the heating rate leads to more distinct peaks in the DSC curves and shifts the peaks towards higher temperatures (see Fig. 5.5.4a). Furthermore, peak C_1 and C_2 in Fig. 5.5.4c have a tendency to overlap by increasing the heating rate. Both effects have been obtained in [12].

- The DSC curves in Fig. 5.5.4c show a peak A which is visible due to the formation of Cu-Mg co-clusters (GP zones) [14]. For peak A, almost the same heat flow was obtained in DSC experiment as given in [14].

- In the experiment, two specimens were solution heat treated for 25min at different temperatures, the first one at 550°C and the second one at 495°C. In Fig. 5.5.4c, peak A and B (which is due to the dissolution of the GP zones [14]) are almost equal for each solution heat treatment temperature.

- The most significant difference shows peak C_1 and C_2 in Fig. 5.5.4c. These are attributed to the formation of S phase ($CuMgAl_2$) precipitates. The lower solution heat treatment temperature of 495°C leads to a higher difference between the peaks. In [14] C_I and C_{II} were investigated and as a result two precipitate types of S were defined, type I and type II. The formation of type II phase precipitates is strongly dependent on solution treatment and cold work and has a random interface with the matrix [14]. In solution treated, quenched and cold worked samples, an extensive formation of type I occurs, whilst the formation of type II is suppressed [14].

- Peak D, which is the result of the dissolution of the S precipitates [14], and E, which is the result of the partial melting of S+θ eutectics [14], show no significant difference between the two different solution treatment temperatures.

Observing the comparison of hardness curves (Fig. 5.5.3) and DSC curves (Fig. 5.5.4e), the precipitation sequence is completed after one week. Peak A in Fig. 5.5.4e disappears for the longer aged specimen because the formation of Cu-Mg co-clusters is completed after 1 week [13].

The specimen which was heat treated at 495°C exhibits a lower hardness than the specimen which was heat treated at 550°C, see Fig. 5.5.3. A higher number of metastable phases and an increase of S-phase decomposition might lead to the difference in hardness [10]. Peak C in Fig. 5.5.4g is lower for the 495°C – specimen which denotes a lower hardness. The same results were obtained in [13]. The observation that the 495°C – specimen has two C – peaks and the 550°C – specimen only one, can be lead back to solving more precipitate phases during higher temperature solution heat treatment [10].

7 Summary and conclusions

Manufacturing of Al-Cu and Al-Cu-Mg alloys could be completed with satisfying results because the stirring motions of the induction furnace lead to a homogeneous alloy. Scanning electron microscope analysis at the top and the bottom of the ingots proved that gravity has no influence on the copper and magnesium distribution in the aluminum matrix.

When vacuum was used as the surrounding atmosphere for the melt, the manufactured alloy exhibited different hardness values maybe due to different cooling rate. The highest hardness values were not obtained for the sample, which was cooled under the highest vacuum. The effect of gas would be to increase the heat transfer from the crucible to the environment. This cooling effect can directly affect the hardness of an as-cast material.

In the experiment, three different crucibles were used for the manufacturing procedure. The graphite one allows a temperature measurement with a thermocouple in the bottom of the crucible and therefore the induction coil can be pilot-controlled. The silicon oxide and the boron nitride crucible have a lower thermal conductivity and hence the power input of the induction coil has to be regulated manually. Besides, the boron nitride crucible has a smooth surface and a higher temperature resistance. Every crucible can be used for the manufacturing procedure because despite the lower electrical resistivity of the graphite crucible, every manufactured alloy exhibits a homogeneous microstructure. Furthermore, the manual regulation of the induction coil is possible because of the presence of an inspection glass. In addition, the temperature of the melt could be measured through the inspection glass with an adjusted temperature measurement range spectrometer.

The manufactured samples were homogenized and extruded afterwards. Light and scanning electron microscope analyses of the microstructure in the as-cast and extruded condition provided different results. The extrusion led to a closure of porosities and the interdendritic spaces. DSC analyses and hardness measurements proved that the precipitation sequence of Al-Cu alloys is not as fast as the one of Al-Cu-Mg alloys. The different binding energy between atoms and different precipitation kinetics of precipitation phases are responsible for this difference. A higher deformation degree during extrusion leads to smaller grains and increases the hardness. Comparisons of DSC and hardness results match very well with experimental results given in literature.

When the industrial 2024 aluminum alloy is solution heat treated at 550°C instead of 495°C, the hardness increases with approximately 15 HBW1/10. Higher solution heat treatment temperature means that more precipitate phases can go into solution and potentially higher precipitation hardening. As a disadvantage, a higher heat treating temperature can decrease the fracture toughness.

The main objective of the experiments was to gather and develop the necessary know-how to use correctly the existing furnace facilities to produce different aluminum alloys. The comparison of the manufactured Al-Cu-Mg alloy with the industrial 2024 aluminum alloy shows a satisfactory result. This work should give sufficient fundamentals to produce new alloys with the induction furnace and in addition some general information about heat treatment and material characterization of the Al-Cu-Mg system.

8 References

[1] Imran Nasim Khan; PhD Thesis 2007; University of Southampton Research Repository ePrints Soton (2007)

[2] Dietrich G. Atlenpohl; Aluminum: Technology, applications, and environment (1998)

[3] H.W.L. Philipps, M.A., F.R.I.C., F.Inst.P, F.I.M; Annotated equilibrium diagrams of some aluminium alloy systems; Institute of metals monograph and report series No. 25

[4] http://de.wikipedia.org/wiki/

[5] Inoue Makoto, En´yama Takafumi, Iwai Masao; Vacuum Sublimation Refining of Magnesium; Research Reports of Toyama National College of Technology

[6] Schiele&Schön; Giesserei Lexikon 18. Auflage (2000); p. 210-211

[7] Friedrich Ostermann; Anwendungstechnologie Aluminium 1998, p.71/72

[8]; A Hayoune, D. Hamana; Journal of Alloys and Compounds 474 (2009) 118–123

[9] S.P. Ringer and K. Hono; Materials characterization 44:101–131 (2000)

[10] Hermann Schumann and Heinrich Oettel; Wiley-VCH Verlag; Metallografie 14. Auflage (2005); p. 844-864

[11] S.K. Son, M. Takeda, M. Mitome, Y. Bando, T. Endo; Materials Letters 59 (2005) 629– 632)

[12] A. Gaber, A. Mossad Ali; Journal of Alloys and Compounds 432 (2007) 149–155 (2006)

[13] J. Starink, N. Gao, J.L. Yan; Materials Science and Engineering A 387–389 (2004) 222–226

[14] S.C. Wang, M.J. Starink; Acta Materialia 55 (2007) 933–941

[15] http://www.finishing.com/269/68.shtml

[16] W.Y. Kim, C.G. Kang, B.M. Kim; Materials Science and Engineering A 447 (2007) 1–10

[17] SUG WON KIM and HAI HAO; Microstructure and Fatigue Characteristics of Direct Chill Cast and Electromagnetic Cast 2024 Al Alloy Ingots; Korea Sanhak Foundation (2002)

[18] Prof. Hans Peter Degischer; Light Metals lecture

[19] Y. Totik, M. Gavgali; Materials Characterization 49 (2003) 261– 268

[20] Anne Lise Dons; Journal of Light Metals 1 (2001) 133-149

[21] GRANTA material ingelligence; CES Edupack and CES Selector 2009 (Materials Software; Materials Data and Materials Database); Level 3

9 Appendix

9.1 Hardness measurement

9.1.1 Results of the Al-4,3Cu alloys in the as-cast condition

Table 9.1.1: Hardness values of sample 3, 5 and 6

	Sample 3	Sample 5	Sample 6
HBW 2,5/15,625	44,6	40,6	43,5
	46,3	44,5	43,6
	44,5	42,5	45,4
	47,2	38,9	44,9
	45,2	43,1	47,4
	43,3	39,8	47,4
	43,9	41,8	46,1
	43,0	43,1	47,4
HBW 2,5/15,625 Average	44,75	41,79	45,71

9.1.2 Results of the Al-4,3Cu alloys after homogenization and extrusion

Table 9.1.2a: Hardness values of sample 5

Time after quenching	10min	30min	1h	2h	4h	1 day	1 week	2 weeks	3 weeks	4 weeks	5 weeks
HBW 1/10	53,4	55,3	59,9	60,9	64,2	65,5	65,1	68,0	66,6	64,2	69,2
	53,6	55,9	59,9	62,8	64,4	65,8	66,2	68,8	64,0	67,0	68,0
	52,9	56,6	58,9	60,9	63,3	62,8	65,1	66,2	64,9	65,9	68,3
	53,4	56,2	58,1	61,8	62,8	64,1	65,8	67,1	64,8	66,8	69,7
	52,4	55,3	58,9	62,3	63,3	63,2	66,9	67,0	65,2	66,1	69,9
HBW 1/10 Average	53,14	55,86	59,14	61,74	63,6	64,28	65,82	67,42	65,1	66,0	69,02

Table 9.1.2b: Hardness values of sample 6

Time after quenching	10min	30min	1h	2h	4h	1 day	1 week	2 weeks	3 weeks	4 weeks	5 weeks
HBW 1/10	58,3	58,4	60,1	60,7	63,3	65,5	72,2	70,3	71,9	70,6	73,8
	57,9	57,0	59,5	61,2	63,7	65,5	70,9	73,8	70,3	71,3	76,8
	57,8	59,0	59,3	60,9	64,8	65,5	69,1	69,8	70,1	69,9	77,1
	56,2	57,5	60,5	61,2	65,5	67,2	69,8	73,5	68,8	72,4	73,5
	56,9	58,1	59,1	60,5	65,3	66,4	71,0	72,0	68,8	71,0	73,5
HBW 1/10 Average	57,42	58	59,7	60,9	64,52	66,02	70,6	71,88	69,98	71,04	74,94

9.1.3 Results of the Al-4,3Cu-1,49Mg alloy after homogenization and extrusion

Table 9.1.3: Hardness values of sample 7, solution heat treated at 495°C for 30min

Time after quenching	10min	30min	1h	2h	4h	1 day	2 days	1 week	9 days	12 days	2 weeks
HBW 1/10	57,9	63,1	69,3	78,6	81,3	97,3	104	102	100	101	99,8
	58,5	63,4	70,9	76,0	83,9	96,5	103	103	101	98,6	101
	58,7	62,8	71,4	77,1	79,9	97,3	105	102	102	100	99,8
	59,1	65,1	72,2	76,9	83,6	96,9	104	102	99,0	99,0	99,8
	58,4	65,1	71,1	78,0	82,0	96,9	103	102	101	98,8	99,8
HBW 1/10 Average	58,52	63,9	70,98	77,32	82,14	96,98	103,8	102,2	100,6	99,48	100,04

9.1.4 Results for the industrial 2024 aluminum alloy

Table 9.1.4a: Hardness values of the 2024 aluminum alloy, solution heat treated at 550°C for 25min

Time after quenching	10min	30min	1h	2h	3h 30min	4h	5h	1 day	1 week	2 weeks	3 weeks	4 weeks
HBW 1/10	102	101	107	113	117	118	124	129	132	132	130	126
	99,4	103	106	113	118	120	124	128	133	132	132	127
	99,8	100	105	114	118	121	123	130	131	132	131	127
	101	104	106	113	119	118	124	128	134	130	131	128
	103	104	105	115	121	117	122	129	132	132	129	128
HBW 1/10 Average	101,04	102,4	105,8	113,6	118,6	118,8	123,4	128,8	132,4	131,6	130,6	127,2

Method for the calculation of measurement inaccuracy

Standard deviation according the 1σ limiting deviation

$$u_E := \frac{0.02 \cdot 246.8}{2.8} \qquad u_E = 1.763 \qquad \text{Table 2 according to the standard}$$

Standard uncertainty of the hardness of the CRM (Insecurity which is connected with the metrological overall function of the durometer and the plate for comparing hardness)

$$u_{CRM} := \frac{2.2}{2} \qquad u_{CRM} = 1.1$$

Standard uncertainty of the durometer during measurement on the CRM

$$H_1 = \frac{\sum_{i=1}^{n} H_{1i}}{n} \qquad H_1 := \frac{246 + 245 + 246 + 246 + 246}{5} \qquad H_1 = 245.8$$

$$H_2 = \frac{\sum_{i=1}^{n} H_{2i}}{n} \qquad H_2 := \frac{245 + 246 + 247 + 246 + 247}{5} \qquad H_2 = 246.2$$

$$s_{H1} = \sqrt{\frac{1}{(n-1)} \cdot \sum_{i=1}^{n} \left(H_i - H_1\right)^2} \qquad s_{H1} := 0.45$$

$$s_{H2} = \sqrt{\frac{1}{(n-1)} \cdot \sum_{i=1}^{n} \left(H_i - H_2\right)^2} \qquad s_{H2} := 0.84$$

$s_{H1} > s_{H2}$ => for s_H the higher value is used $\qquad s_H := 0.84$

Standard uncertainty of the durometer during the measurement on the CRM

$t := 1.14$ for $n := 5$

$$u_H := \frac{t \cdot s_H}{\sqrt{n}} \qquad u_H = 0.428$$

Average&standard deviation during the measurement with the specimen

$$x = \sum_{i=1}^{n} x_i$$

$x_1 := 101.04 \quad x_4 := 113.6 \quad x_7 := 123.4 \quad x_{10} := 131.6$

$x_2 := 102.4 \quad x_5 := 118.6 \quad x_8 := 128.8 \quad x_{11} := 130.6$

$x_3 := 105.8 \quad x_6 := 118.8 \quad x_9 := 132.4 \quad x_{12} := 127.2$

$$s_x = \sqrt{\frac{1}{(n-1)} \cdot \sum_{i=1}^{n} \left(x_i - x\right)^2}$$

$$s_{x1} := \sqrt{\frac{1}{n-1} \cdot \left[\left(102 - x_1\right)^2 \cdot \left[\left(99.4 - x_1\right)4\right]^2 \cdot \left(99.8 - x_1\right)^2 \cdot \left(101 - x_1\right)^2 \cdot \left(103 - x_1\right)^2\right]} \qquad s_{x1} = 0.306$$

$$u_{x1} := t \cdot \frac{s_{x1}}{\sqrt{n}} \qquad u_{x1} = 0.156$$

$$s_{x2} := \sqrt{\frac{1}{n-1} \cdot \left[\left(101 - x_2\right)^2 \cdot \left(103 - x_2\right)^2 \cdot \left(100 - x_2\right)^2 \cdot \left(104 - x_2\right)^2 \cdot \left(104 - x_2\right)^2\right]} \qquad s_{x2} = 2.58$$

$$u_{x2} := t \cdot \frac{s_{x2}}{\sqrt{n}} \qquad u_{x2} = 1.316$$

$$s_{x3} := \sqrt{\frac{1}{n-1} \cdot \left[\left(107 - x_3\right)^2 \cdot \left(106 - x_3\right)^2 \cdot \left(105 - x_3\right)^2 \cdot \left(106 - x_3\right)^2 \cdot \left(105 - x_3\right)^2\right]} \qquad s_{x3} = 0.015$$

$$u_{x3} := t \cdot \frac{s_{x3}}{\sqrt{n}} \qquad u_{x3} = 7.831 \times 10^{-3}$$

$$s_{x4} := \sqrt{\frac{1}{n-1} \cdot \left[\left(113 - x_4\right)^2 \cdot \left(113 - x_4\right)^2 \cdot \left(114 - x_4\right)^2 \cdot \left(113 - x_4\right)^2 \cdot \left(115 - x_4\right)^2\right]} \qquad s_{x4} = 0.06$$

$u_{x4} := t\cdot\frac{s_{x4}}{\sqrt{n}}$ $\qquad u_{x4} = 0.031$

$s_{x5} := \sqrt{\frac{1}{n-1}\cdot\left[(117 - x_5)^2\cdot(118 - x_5)^2\cdot(118 - x_5)^2\cdot(119 - x_5)^2\cdot(121 - x_5)^2\right]}$ $\qquad s_{x5} = 0.276$

$u_{x5} := t\cdot\frac{s_{x4}}{\sqrt{n}}$ $\qquad u_{x5} = 0.031$

$s_{x6} := \sqrt{\frac{1}{n-1}\cdot\left[(118 - x_6)^2\cdot(120 - x_6)^2\cdot(121 - x_6)^2\cdot(118 - x_6)^2\cdot(117 - x_6)^2\right]}$ $\qquad s_{x6} = 1.521$

$u_{x6} := t\cdot\frac{s_{x6}}{\sqrt{n}}$ $\qquad u_{x6} = 0.775$

$s_{x7} := \sqrt{\frac{1}{n-1}\cdot\left[(124 - x_7)^2\cdot(124 - x_7)^2\cdot(123 - x_7)^2\cdot(124 - x_7)^2\cdot(122 - x_7)^2\right]}$ $\qquad s_{x7} = 0.06$

$u_{x7} := t\cdot\frac{s_{x7}}{\sqrt{n}}$ $\qquad u_{x7} = 0.031$

$s_{x8} := \sqrt{\frac{1}{n-1}\cdot\left[(129 - x_8)^2\cdot(128 - x_8)^2\cdot(130 - x_8)^2\cdot(128 - x_8)^2\cdot(129 - x_8)^2\right]}$ $\qquad s_{x8} = 0.015$

$u_{x8} := t\cdot\frac{s_{x8}}{\sqrt{n}}$ $\qquad u_{x8} = 7.831 \times 10^{-3}$

$s_{x9} := \sqrt{\frac{1}{n-1}\cdot\left[(132 - x_9)^2\cdot(133 - x_9)^2\cdot(131 - x_9)^2\cdot(134 - x_9)^2\cdot(132 - x_9)^2\right]}$ $\qquad s_{x9} = 0.108$

$u_{x9} := t\cdot\frac{s_{x9}}{\sqrt{n}}$ $\qquad u_{x9} = 0.055$

$s_{x10} := \sqrt{\frac{1}{n-1}\cdot\left[(132 - x_{10})^2\cdot(132 - x_{10})^2\cdot(132 - x_{10})^2\cdot(130 - x_{10})^2\cdot(132 - x_{10})^2\right]}$ $\qquad s_{x10} = 0.02$

$u_{x10} := t\cdot\frac{s_{x10}}{\sqrt{n}}$ $\qquad u_{x10} = 0.01$

$s_{x11} := \sqrt{\frac{1}{n-1}\cdot\left[(130 - x_{11})^2\cdot(132 - x_{11})^2\cdot(131 - x_{11})^2\cdot(131 - x_{11})^2\cdot(129 - x_{11})^2\right]}$ $\qquad s_{x11} = 0.108$

$u_{x11} := t\cdot\frac{s_{x11}}{\sqrt{n}}$ $\qquad u_{x11} = 0.055$

$$s_{x12} := \sqrt{\frac{1}{n-1}\cdot\left[\left(126-x_{12}\right)^2\cdot\left(127-x_{12}\right)^2\cdot\left(127-x_{12}\right)^2\cdot\left(128-x_{12}\right)^2\cdot\left(128-x_{12}\right)^2\right]} \qquad s_{x12} = 0.015$$

$$u_{x12} := t\cdot\frac{s_{x12}}{\sqrt{n}} \qquad u_{x12} = 7.831\times10^{-3}$$

Standard uncertainty due to the resolution of the length measuring system

$$u_{ms} = \frac{\delta_{ms}}{2\cdot\sqrt{3}} = \frac{1\text{HBW}}{2\cdot\sqrt{3}} \qquad u_{ms} := \frac{1}{2\cdot\sqrt{3}} \qquad u_{ms} = 0.289$$

Uncertainty of the measurement

$$U = \sqrt{u_E^{\,2} + u_{CRM}^{\,2} + u_H^{\,2} + u_x^{\,2} + u_{ms}^{\,2}} \qquad X = x + -U$$

$$U_1 := \sqrt{u_E^{\,2} + u_{CRM}^{\,2} + u_H^{\,2} + u_{x1}^{\,2} + u_{ms}^{\,2}} \qquad U_1 = 2.147$$

After 10min: (101,04 + - 2,1) HBW

$$U_2 := \sqrt{u_E^{\,2} + u_{CRM}^{\,2} + u_H^{\,2} + u_{x2}^{\,2} + u_{ms}^{\,2}} \qquad U_2 = 2.513$$

After 30min: (102,4 + - 2,5) HBW

$$U_3 := \sqrt{u_E^{\,2} + u_{CRM}^{\,2} + u_H^{\,2} + u_{x3}^{\,2} + u_{ms}^{\,2}} \qquad U_3 = 2.141$$

After 1h: (105,8 + - 2,1) HBW

$$U_4 := \sqrt{u_E^{\,2} + u_{CRM}^{\,2} + u_H^{\,2} + u_{x4}^{\,2} + u_{ms}^{\,2}} \qquad U_4 = 2.141$$

After 2h: (113,6 + - 2,1) HBW

$$U_5 := \sqrt{u_E^{\,2} + u_{CRM}^{\,2} + u_H^{\,2} + u_{x5}^{\,2} + u_{ms}^{\,2}} \qquad U_5 = 2.141$$

After 3h 30min: (118,6 + - 2,1) HBW

$$U_6 := \sqrt{u_E^{\,2} + u_{CRM}^{\,2} + u_H^{\,2} + u_{x6}^{\,2} + u_{ms}^{\,2}} \qquad U_6 = 2.277$$

After 4h: (118,8 + - 2,3) HBW

$$U_7 := \sqrt{u_E^{\,2} + u_{CRM}^{\,2} + u_H^{\,2} + u_{x7}^{\,2} + u_{ms}^{\,2}} \qquad U_7 = 2.141$$

After 5h: (123,4 + - 2,1) HBW

$$U_8 := \sqrt{u_E^{\,2} + u_{CRM}^{\,2} + u_H^{\,2} + u_{x8}^{\,2} + u_{ms}^{\,2}} \qquad U_8 = 2.141$$

After 1 day: (128,8 + - 2,1) HBW

$$U_9 := \sqrt{u_E^2 + u_{CRM}^2 + u_H^2 + u_{x9}^2 + u_{ms}^2} \qquad U_9 = 2.142$$

After 1 week: (132,4 + - 2,1) HBW

$$U_{10} := \sqrt{u_E^2 + u_{CRM}^2 + u_H^2 + u_{x10}^2 + u_{ms}^2} \qquad U_{10} = 2.141$$

After 2 weeks: (131,6 + - 2,1) HBW

$$U_{11} := \sqrt{u_E^2 + u_{CRM}^2 + u_H^2 + u_{x11}^2 + u_{ms}^2} \qquad U_{11} = 2.142$$

After 3 weeks: (130,6 + - 2,1) HBW

$$U_{12} := \sqrt{u_E^2 + u_{CRM}^2 + u_H^2 + u_{x12}^2 + u_{ms}^2} \qquad U_{12} = 2.141$$

After 4 weeks: (127,2 + - 2,1) HBW

The deviation of maximum 2,5 HBW1/10 and minimum 2,1 HBW1/10 won´t change much further measurements and hence the measurement inaccuracy was only calculated for this specimen.

Table 9.1.4b: Hardness values of the 2024 aluminum alloy, solution heat treated at 495°C for 25min

Time after quenching	10min	30min	1h	2h	3h 30min	4h	5h	1 day	1 week	2 weeks	3 weeks	4 weeks
HBW 1/10	82,3	83,6	89,0	100	102	103	107	114	118	116	117	116
	82	84,2	89,7	98,2	103	104	109	114	117	117	115	117
	82,3	84,2	91,9	99,4	103	105	107	115	119	116	116	117
	82,6	83,9	91,5	98,2	102	104	108	116	117	117	117	116
	82,3	84,9	90,1	98,6	101	103	109	113	117	117	117	116
HBW 1/10 Average	82,3	84,2	90,4	98,88	102,2	103,8	107,8	114,4	117,6	116,6	116,4	116,4